



UNIVERSITY
OF MANITOBA

**Active Magnetic Compensation Prototype for a
Neutron Electric Dipole Moment Experiment**

by

Shomi Ahmed

A thesis submitted to
The Faculty of Graduate Studies of
The University of Manitoba
in partial fulfillment of the requirements
of the degree of

Master of Science

Department of Physics & Astronomy
The University of Manitoba
Winnipeg, Manitoba, Canada
April 2019

© Copyright 2019 by Shomi Ahmed

Thesis Advisor and Co-advisor

Author

Dr. Jeff Martin and Dr. Chris Bidinosti

Shomi Ahmed

Abstract

The existence of a non-zero neutron electric dipole moment (nEDM) would violate parity and time-reversal symmetry. Extensions to the Standard Model predict the nEDM to be $10^{-26} - 10^{-28}$ e·cm. The current best upper limit is 3.0×10^{-26} e·cm. The nEDM experiment at TRIUMF is aiming to improve the precision of the measurement to the 10^{-27} e·cm level. The experiment requires a very stable ($< \text{pT}$) and homogeneous ($< \text{nT/m}$) magnetic field (B_0) within the measurement cell.

This thesis concerns the development of active magnetic shielding to stabilize the external magnetic field by compensation coils using a prototype active magnetic shield at The University of Winnipeg. Experimental results are compared with simulations of the behaviour of the active magnetic compensation system. The quasi-static magnetic behavior of the system, including the effect of the passive magnetic shields, is included in this simulation using finite element analysis (FEA). These results are then used to create a full time-dependent simulation of the multi-dimensional feedback system response. A major challenge faced in the development of the system was a slow current response, even though the magnetic response was rapid. This is now understood to be due to having too much freedom in assigning the currents in the system. Reducing the degrees of freedom in the coil system, as an alternate strategy to Tikhonov regularization, solved this problem in a way that hasn't been previously discussed in the literature. Several recommendations are made to improve the performance in future realizations of the system at TRIUMF.

Acknowledgments

Being an engineering student, I found the alleyways were topsy-turvy during the tenure of my Masters journey. I stepped in with a high hope, stumbled sometimes in the middle but always found the right guidance and motivation for pursuing my objective.

Firstly, I must recognize the contribution of my supervisor Dr. Jeff Martin for taking the risk, keeping faith on my ability. More so, Dr. Martin has given me unparalleled freedom to feel a foreign land as my second home despite located 12000 km away from my motherland. He has always guided me whenever I stuck up in my research. He has given me the opportunity to attend several conferences all over Canada beyond the imagination of a Masters student. His contributions are phenomenal for my research and thesis writing. His mentoring and passion for exploring the mysteries of this project motivated me in every step. He has been the most influential resource professional while I mature from a simple student to a better researcher of my ability.

Next important person who deserves special mention is David Ostapchuk. He has helped me graciously to settle in, write codes as well as build apparatus for my research project. In addition to my supervisor, whenever I faced problems, I knew that I could always rely on Dave for solution.

I would like to thank my co-supervisor Dr. Chris Bidinosti for his generous help and support during my Masters journey as well as while writing this thesis. I would also like to thank Dr. Peter Blunden and Dr. Cyrus Shafai for serving to my committee. In addition to my supervisor, co-supervisor, and committee members, I want to thank

Dr. Takashi Higuchi for reviewing my thesis. I am grateful to Dr. Russell Mammei for his contribution in OPERA simulation. I am also grateful to Dr. Beatrice Franke and Dr. Blair Jamieson for their valuable suggestions during my research work.

The graduate students particularly Dr. Taraneh Andalib, Sakib Rahman, Michael Lang, Moushumi Das, Ray Dwaipayana, Sean Hansen-Romu and Wolfgang Klassen were especially cooperative to me. I am thankful to each of them.

Last but not the least, I want to thank my family specially my mother and also my friends who have supported me always. Above all, I am grateful to the almighty Allah for His endless mercy.

It has been an honor to be part of this wonderful project and be around some extraordinary scholars.

Thank you all.

Shomi

Dedicated to -

My father whom I lost during my Masters journey.

May Allah rest his soul and place him in heaven.

Contents

Abstract	ii
Acknowledgments	iii
Dedication	v
Table of Contents	viii
List of Tables	ix
List of Figures	x
1 Motivation for a New Precise Measurement of the nEDM	1
1.1 Baryon Asymmetry and the nEDM	2
1.2 Ultracold Neutrons	4
1.3 Measurement Principle of nEDM	5
1.4 Experimental Efforts	6
1.5 TUCAN nEDM Experiment	10
2 Overview of Magnetic Field Systems	12
2.1 Magnetic Field Requirements for TUCAN nEDM Experiment	12
2.1.1 Active Magnetic Shield	14
2.1.2 Passive Magnetic Shield	16
2.1.3 Internal Coil System	16
2.1.4 Internal Magnetometry	17
2.2 Review of the Active Magnetic Compensation Systems Developed for Other nEDM Experiments	18
2.3 Overview of the AMC prototype development	21
3 Active Magnetic Compensation Prototype	22
3.1 Overview of AMC Prototype	23
3.2 Mu-Metal Shields	24
3.3 Coil Cube	26
3.4 Fluxgate Sensors	28
3.5 Data Acquisition (DAQ) Module	29
3.6 DAC and the Current Sink	33

3.7	Filtering	36
3.8	Field Fluctuations Surrounding the Prototype	39
4	AMC Prototype Feedback and Control Algorithm	42
4.1	Principle of Operation	43
4.2	Matrix of Proportionality Factors	43
4.3	Implementation of PI Control Algorithm	46
4.4	Inversion of Matrix	49
4.4.1	Regularization by Random Fluctuation	53
4.5	Tuning of PI Parameters	57
4.6	Quantitative Measures of Magnetic Compensation Performance	59
4.6.1	Condition Number	60
4.6.2	Reduction of Magnetic Field Fluctuation and PI Behavior upon Stimulus	60
4.6.3	Allan Deviations and Shielding Factors	63
5	Quantification of Active Magnetic Compensation Prototype	66
5.1	Sampling Frequency and Filtering	67
5.2	PI Tuning General Behavior	73
5.2.1	Effect of changing P term	74
5.2.2	Effect of the I term	76
5.2.3	Effect of adjusting both P and I	78
5.2.4	The “Current Drifting Problem”	80
5.3	Fluxgate Placements and Impact of Passive Shield	81
5.3.1	Fluxgate Placements	82
5.3.2	Impact of Passive Shield	86
5.4	Simulation of Multidimensional Feedback System	88
5.4.1	Simulation in OPERA to Generate Field Maps in Coil Cube	89
	Geometry Definition in OPERA	89
	Simulation Applying Current in Compensation Coils	91
	The Effect of Earth’s Field and of the Perturbation Coil	93
5.4.2	Field Map Processing in Python	94
5.4.3	PI Simulation in Python	97
5.5	Studies on the Regularization Parameter r	98
5.5.1	Effect of r on PI Tuning	99
5.5.2	Regularization by Matrix Condition Number Method	104
5.6	“New” feedback algorithm vs. standard PI control	106
5.7	Coil Configuration	110
5.8	Other metrics of feedback system performance	129
5.8.1	Internal Sensor Perturbations	129
5.8.2	Allan Deviation Results	132

6	Conclusion	141
6.1	Key Findings	141
6.2	Recommendations on the Active Magnetic Compensation System Design Process for TUCAN	144
6.2.1	Test designs based on known perturbations	144
6.2.2	To regularize or not to regularize	145
6.2.3	Condition number is not everything	146
6.2.4	What to do instead of regularizing	146
	Coils that generate spherical harmonics	147
	Eliminating the zero-field mode	147
6.2.5	Develop a full FEA plus feedback system simulation	148
6.3	Implementation in the TUCAN nEDM Experiment	148
A	Analytic solutions to a spherical mu-metal shell in multi-pole field	153
A.1	General solution for an applied zonal field	154
A.1.1	Using Equivalent Bound Surface Currents	155
A.1.2	Using Scalar Potential	158
A.1.3	Comparison of two methods	163
A.2	Magnetic field with uniform background ($l=1$)	164
A.2.1	Comparison with simulation	165
	Bibliography	168

List of Tables

3.1	Dimensions of prototype passive shielding layers	25
3.2	Coil dimensions and electrical properties.	27
3.3	Properties of the fluxgate sensors used for the prototype.	28
3.4	T7 Pro manufacturer's sample frequency for different resolution index	31
3.5	T7 Pro measured loop frequency for different resolution index	32
3.6	4 th -order Low-Pass Butterworth Filter Specification	36
4.1	Definition of different indices used to indicate sensor, coil and iterations	44
4.2	Typical magnetic fields surrounding the prototype	47
4.3	Ziegler-Nichols tuning method for P and PI controllers.	58
5.1	Matrix properties for different numbers of fluxgate sensors at different positions.	84
5.2	Properties for different coil configurations	119
A.1	Properties of the spherical mu-metal shield in OPERA.	166
A.2	Comparison of simulated \mathbf{B} field with analytical one	167

List of Figures

1.1	Standard model of elementary particles.	2
1.2	Ramsey’s method of separated oscillatory fields.	5
1.3	Experimental nEDM upper limit over the years	7
1.4	Conceptual design of the proposed TUCAN source and nEDM Experiment.	10
2.1	Schematic diagram for the TUCAN nEDM magnetic field systems	14
3.1	Active Magnetic Field Compensation (AMC) Prototype at the University of Winnipeg	23
3.2	Prototype passive shielding at the University of Winnipeg	25
3.3	Schematic diagram indicating the coil configuration and the position of the fluxgate sensors.	27
3.4	Average Spectral Density for Mag690.	29
3.5	Effective resolution for different resolution index for gain 1 and $\pm 10 V$ range.	30
3.6	Current Sink Device	34
3.7	Resolution of LJTick-DACs	35
3.8	4 th -order low-pass Butterworth filter	37
3.9	Frequency response of a 4 th -order low-pass Butterworth filter.	38
3.10	Fluctuations of the magnetic field at UofW	40
3.11	Histogram of the difference in the magnetic field.	41
4.1	Color map of \mathbf{M}	46
4.2	The compensation effect on single sensor due to single coil.	49
4.3	Color map of Σ	51
4.4	The effect of r on the coil currents.	54
4.5	The effect of r on remaining fluctuations.	56
4.6	The effect of r on normalized current and remaining fluctuations.	57
4.7	Zoomed current behaviour in coil C_x^+	59
4.8	Magnetic field reduction at some of the sensor positions.	61

4.9	The effect of r for experimental setup.	62
4.10	The Allan deviation.	64
5.1	Filtering effect on the magnetic field signals.	69
5.2	Active magnetic field compensation at sensor position 1y.	70
5.3	Compensation behaviour for various resolution indices.	71
5.4	Compensation behaviour for various resolution indices with different software averages.	73
5.5	Coil currents with field change ΔB for different values of k_c^p	75
5.6	The effect of k_c^p on fluctuations.	76
5.7	Coil currents with field change ΔB for k_c^i	77
5.8	Coil currents with drift ΔB for different values of k_c^p only.	79
5.9	Comparison of magnetic compensation results with and without the magnetic shield present.	87
5.10	Prototype geometry in OPERA simulation	90
5.11	Settings to generate surface mesh in OPERA.	91
5.12	Field map of the cube for C_y^- coil energized.	92
5.13	Comparison of experimental and simulated \mathbf{M}	95
5.14	Comparison of experimental and simulated magnetic compensation results.	98
5.15	Single magnetic field compensation results for fixed k_c^p and r and different values of k_c^i	100
5.16	Single magnetic field compensation results for fixed k_c^p and k_c^i and different values of r	101
5.17	Coil currents with field change ΔB for $k_c^p = 0.60$, $k_c^i = 0.37$ and $r = 2.4$	102
5.18	Coil currents with field change ΔB for $k_c^p = 0.0$, $k_c^i = 1.0$ and $r = 2.4$	103
5.19	Comparing r from two different methods.	104
5.20	Comparison of old and new feedback algorithms.	108
5.21	Matrix for 6 coils.	111
5.22	Diagonal Matrix for 6 coils.	112
5.23	Orthogonal matrix \mathbf{V}^T for 6 coils.	112
5.24	Singular currents corresponding to the singular value $\Sigma_{66} = 0$	114
5.25	Matrix for 5 coils.	117
5.26	Diagonal Matrix for 5 coils.	117
5.27	Orthogonal matrix \mathbf{V}^T for 5 coils.	118
5.28	Coil currents with field change ΔB for different coil configurations in regularized \mathbf{M}^{-1}	121
5.29	Coil currents with field change ΔB for different coil configurations with non-regularized \mathbf{M}^{-1}	123
5.30	Experimental results for the Σ matrix.	124
5.31	Experimentally measured right singular vectors.	125
5.32	Five-coil feedback results for common C_z^\pm configuration.	126

5.33	Experimental results for the Σ matrix with the magnetic shield in place.	127
5.34	Five-coil feedback results with the magnetic shield inside the coil cube.	128
5.35	Central magnetic field in the z and x directions, 6-coil feedback algorithm.	130
5.36	The 5-coil feedback algorithm	131
5.37	Field change ΔB for 24 hrs with feedback algorithm switched off.	133
5.38	5-coil feedback algorithm with zoomed coil currents	134
5.39	5-coil feedback algorithm for “natural” fluctuations	136
5.40	Coil currents for the run shown in Fig. 5.39.	136
5.41	Second example run of 5-coil feedback algorithm for “natural” fluctuations	137
5.42	Coil currents for the run shown in Fig. 5.41.	137
5.43	Correcting a slowly ramped current in the perturbation coil.	139
5.44	Coil currents for the run shown in Fig. 5.43.	139
5.45	Second example run correcting a slowly ramped current in the perturbation coil.	140
5.46	Coil currents for the run shown in Fig. 5.45.	140
6.1	Schematic diagram of TUCAN nEDM magnetic field subsystems.	150
A.1	Spherical shell in a uniform magnetic field	155
A.2	Shielding effect of spherical shell in a uniform magnetic field.	164
A.3	Color map of the spherical mu-metal shield in OPERA.	166

Chapter 1

Motivation for a New Precise Measurement of the nEDM

The existence of a non-zero neutron electric dipole moment (nEDM) would violate parity and time-reversal symmetry. As a result, experiments that seek to measure the nEDM, or indeed the permanent electric dipole moment of any particle, have been of great interest for many decades [1]. This thesis focuses on the need for magnetic field stability in such experiments and describes the development of an active magnetic compensation system for such purpose. To begin, this chapter first highlights the scientific interest in a new precise measurement of the nEDM. The measurement principle of the nEDM experiment is discussed with the importance of the magnetic environment for the successfulness of the experiment. Finally, this chapter ends with describing the TRIUMF Ultra Cold Advanced Neutron (TUCAN) EDM experiment.

1.1 Baryon Asymmetry and the $nEDM$

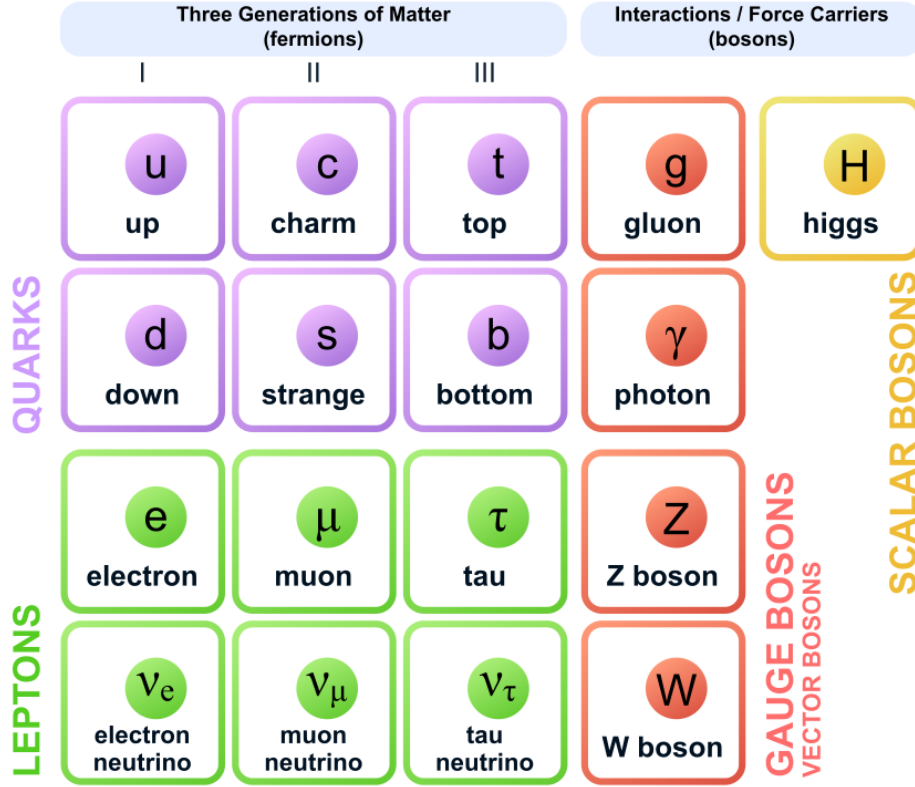


Figure 1.1: Standard model of elementary particles [2]. Three generations of matter aligned column-wise and classified into two groups : quarks and leptons.

The universe is composed of particles which are governed by the four fundamental forces (electromagnetic, weak interaction, strong interaction and gravitational force). The Standard Model (SM) is a theory to describe particle interactions excluding gravity. Quarks, leptons, gauge bosons, and the higgs bosons are the fundamental particles. They are shown in Fig. 1.1.

Baryons such as the neutron are formed from three quarks. In the early universe, there were equal particle numbers of matter and antimatter. But the universe to-

day contains mostly baryonic matter. By experimental observations of the cosmic microwave background radiation (CMBR) the baryon asymmetry can be deduced to be [3]

$$\eta = \frac{n_b - \bar{n}_b}{n_\gamma} \simeq 6.0 \times 10^{-10}, \quad (1.1)$$

where n_b , \bar{n}_b and n_γ are the number of baryons, anti-baryons and photons respectively.

Baryogenesis is the process of creation of a baryon asymmetry from an initially symmetric state. In 1967, A.D. Sakharov described following three conditions on particle theories aiming to explain baryogenesis [4]:

1. **Baryon number (B) violation.** Any theory which creates net baryon number obviously requires B-violating processes.
2. **Charge (C) and Charge-Parity (CP) symmetry violation.** Particle and antiparticle reaction rates must also be different otherwise net baryon creation would be balanced by net anti-baryon creation, hence CP violation is required.
3. **Departure from thermal equilibrium.** In thermal equilibrium, forward reaction rates would balance reverse rates and no net baryon number could be produced, hence a departure from thermal equilibrium is required.

The Big Bang, and subsequent cooling of the universe, offers a way to provide the departure from thermal equilibrium in many models of baryogenesis [5]. Electroweak baryogenesis is a scenario which uses SM processes, the electroweak phase transition, and the expansion and cooling of the universe to explain baryogenesis. One drawback of the electroweak baryogenesis is that there is not enough CP violation in the SM. This motivates searches for new sources of CP violation near the weak scale.

A fundamental symmetry of quantum field theories is CPT symmetry, which implies that time-reversal (T) violation is equivalent to CP violation. An electric dipole moment (EDM) is a measure of separation of oppositely charged particles within a system. To have a nonzero EDM, the system should violate both parity (P) and time-reversal (T) symmetry [6]. Because of the CPT theorem, a non-zero EDM represents a search for new physics that violates CP symmetry. The neutron may have an EDM with its magnitude depending on the nature and origin of T violation [7]. A precise measurement of the nEDM is a very important measurement which could help solving the baryon asymmetry problem by a discovery of new physics.

1.2 Ultracold Neutrons

Ultracold neutrons (UCN) will be used at TRIUMF to measure the nEDM. They have small kinetic energies (< 300 neV). They can be confined in a material bottle because they are reflected at any angle of incidence off suitable material walls [8]. Their interaction with the neutron optical potential of the walls through the strong force enables them to trap. This provides a long time frame (the mean lifetime of neutron is $\tau_n = 881.5$ s [9]) for observation making them ideal for the nEDM experiment. The first UCN were produced in 2017 at TRIUMF using superfluid-helium at 0.9 K as the UCN production medium [10–12].

1.3 Measurement Principle of nEDM

To initiate the measurement process, UCN are first polarized by passage through a strong magnetic field and then guided to the nEDM cell. For the extraction of the nEDM, a form of Ramsey's method of separated oscillatory fields [13] is used. The

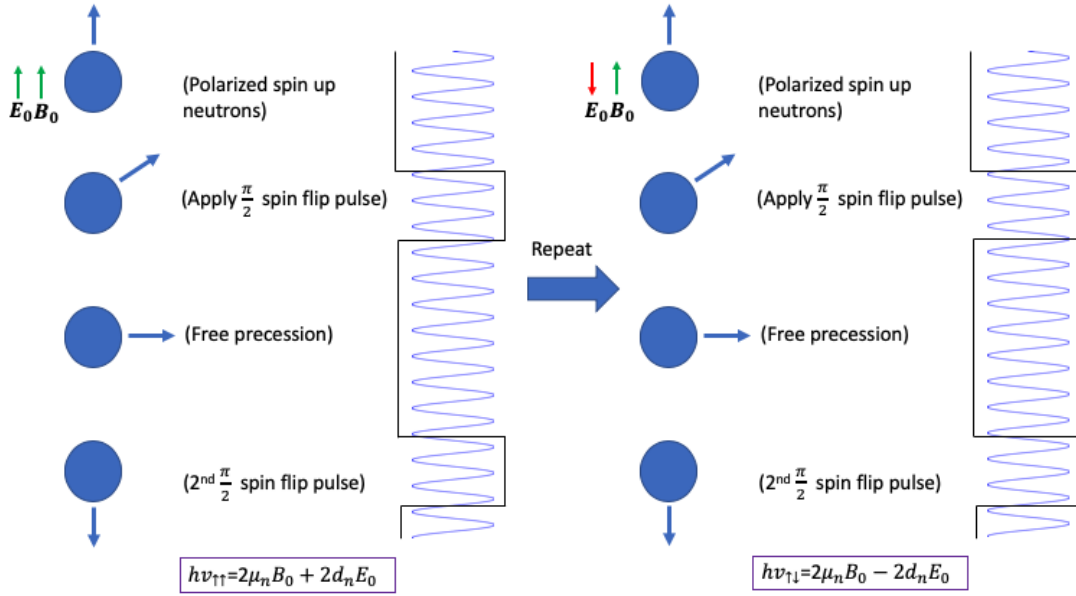


Figure 1.2: Ramsey's method of separated oscillatory fields, as applied to the measurement of the nEDM. The \mathbf{E}_0 field is parallel to \mathbf{B}_0 field on the left, whereas in the right they are antiparallel.

method of the nEDM measurement is shown in Fig. 1.2. At the beginning and end of free precession, short $\pi/2$ pulses are applied. Polarized neutron detection after the pulse sequence is used to measure the free spin precession frequency ν (the Larmor frequency). In the first instance (left one in Fig. 1.2), an electric field (\mathbf{E}_0) parallel to the magnetic field (\mathbf{B}_0) will be applied giving a spin-precession frequency as

$$h\nu_{\uparrow\uparrow} = 2\mu_n B_0 + 2d_n E_0, \quad (1.2)$$

where μ_n and d_n are the magnetic and electric dipole moments respectively, h is Planck's constant and arrows indicate parallel orientation of \mathbf{E}_0 and \mathbf{B}_0 . Now the same experiment is repeated with anti-parallel \mathbf{E}_0 (right one in Fig. 1.2) which gives the spin-precession frequency

$$hv_{\uparrow\downarrow} = 2\mu_n B_0 - 2d_n E_0, \quad (1.3)$$

where the arrows indicate anti-parallel orientation of \mathbf{E}_0 and \mathbf{B}_0 . The measured change in the precession frequency (using Eq. (1.2) and Eq. (1.3)) can be used to deduce the nEDM via

$$d_n = \frac{h(v_{\uparrow\uparrow} - v_{\uparrow\downarrow})}{4E_0}. \quad (1.4)$$

Since the nuclear magnetic resonant (NMR) frequency is proportional to the magnetic field in the nEDM cell, the requirement is to have a very stable and homogeneous \mathbf{B}_0 field within the cell.

1.4 Experimental Efforts

Additional sources of CP violation beyond the standard model predict the nEDM to be in the range of $10^{-26} - 10^{-28}$ e·cm as compared to $10^{-31} - 10^{-33}$ e·cm predicted by the standard model [14–16]. There are several experiments aiming at improving the uncertainty on the nEDM. So far a non-zero nEDM has not been found.

Figure 1.3 summarizes the previous experimental results. Since the first data published in 1957 [17], the upper limit set on the nEDM has been reduced by eight orders of magnitude over the last six decades. In 1980, ultracold neutron (UCN) experiments overtook neutron beam experiments in precision. The current best upper limit set by

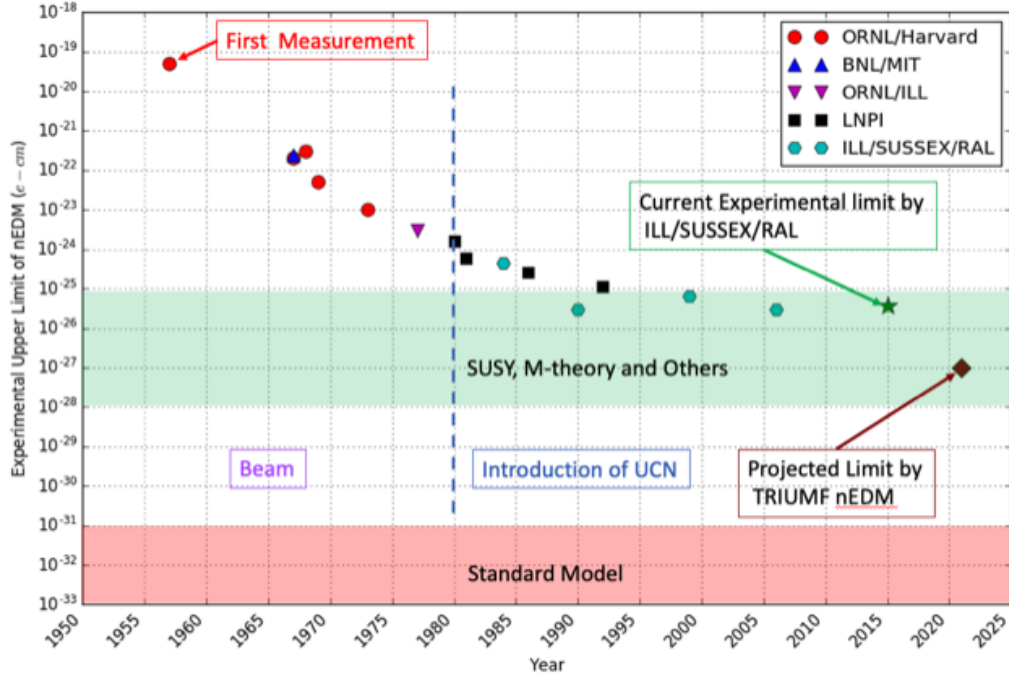


Figure 1.3: Experimental $nEDM$ upper limit over the years [17–33] along with theoretical predictions [14–16]. The vertical dashed line indicates the introduction of UCN. The light green region indicates the $nEDM$ limit in SUSY, M-theory and others while the light red region indicates for SM.

the Sussex-RAL-ILL $nEDM$ experiment is 3.0×10^{-26} e-cm (90 % C.L) [34, 35]. The experiment was performed at Institut Laue-Langevin (ILL, Grenoble, France). A new ^{199}Hg EDM measurement constrains the $nEDM$ better than direct $nEDM$ measurements, giving $d_n < 1.6 \times 10^{-26}$ e-cm [36], although subject to uncertainty from Schiff screening. The TUCAN $nEDM$ experiment is aiming to measure the $nEDM$ with an overall uncertainty at the 10^{-27} e-cm level.

The Paul Scherrer Institut (PSI, Villigen, Switzerland) $nEDM$ experiment used an improved version of the former Sussex-RAL-ILL apparatus. Several innovations were

made at PSI, including a new solid deuterium (SD_2) spallation-driven UCN source. The experiment employed several Cs magnetometers outside the EDM cell, and a ^{199}Hg comagnetometer. Active magnetic shielding and other environmental controls were improved. A new detector that can simultaneously count both spin states of UCN was also implemented. The final sensitivity expected is 10^{-26} e·cm [37] and the final data are being analyzed.

Some of the chief improvements made at PSI have been in the area of nearby alkali atom (Cs) magnetometry, Hg comagnetometry, and neutron magnetometry. An achievement at PSI is the understanding of the Cs magnetometer signals in terms of magnetic field gradients internal to the magnetic shielding. This has led to a detailed understanding of the false EDM of the Hg comagnetometer [38]. Another recent achievement is in using the neutrons themselves to measure gradients [39]. PSI also aims to improve their magnetometry with ^3He magnetometers inside the electrodes of the double EDM measurement cells for their future n2EDM effort. They are developing Cs magnetometers to sense the free-induction decay signal from ^3He , which resulted in a new high-precision magnetometer possessing excellent long-term stability [40]. The precision goal for n2EDM is 5×10^{-28} e·cm [41, 42].

The nEDM collaboration at the Spallation Neutron Source (SNS, Oak Ridge, TN, USA) plans to measure $\delta d_n < 3 \times 10^{-28}$ e·cm [43], which is a two-order magnitude improvement [44]. They plan to use a unique experimental technique. A cold neutron (CN) beam from the SNS will impinge upon a volume of superfluid ^4He creating UCN. The nEDM measurement will also be conducted in the superfluid. A small amount of polarized ^3He introduced into the superfluid ^4He will act as both a comag-

netometer and spin analyzer for the UCN. The ^3He neutron capture rate is strongly spin dependent, and will beat at the difference of the Larmor precession frequencies of the neutrons and ^3He . A non-zero EDM would change the beat frequency with E -reversal. Scintillation light produced in the superfluid will be used to detect the capture products. The false EDM of the ^3He comagnetometer may be reduced by collisions in the surrounding ^4He [45]. The group aims to commission the experiment at SNS by 2022 [43].

At the Los Alamos National Laboratory (LANL, Los Alamos, NM, USA), an upgraded UCN source will be used to conduct a new room-temperature nEDM experiment [46]. An upgrade of the source, and an experiment storing UCN in an nEDM-like bottle has been completed recently [47, 48]. The upgrade enables an nEDM experiment with a statistical sensitivity of 2×10^{-27} e·cm. A test nEDM apparatus, similar in scope to our prototype nEDM apparatus used at RCNP Osaka is assembled by the LANL collaboration to conduct experiments.

AT ILL, groups from Russia [49] and Munich [50] are pursuing two other room temperature nEDM experiments. In the future, the Russian experiment will be moved to the Petersburg Nuclear Physics Institute (PNPI) in Gatchina where their own UCN source is being developed. Internal to the innermost magnetic shield of both experiments are double measurement cells and Cs magnetometers. The Munich experiment's ^{199}Hg comagnetometer and their active and passive magnetic shielding system [51–53] are quite impressive. The groups are at the stage of constructing major equipment and upgrades.

1.5 TUCAN $nEDM$ Experiment

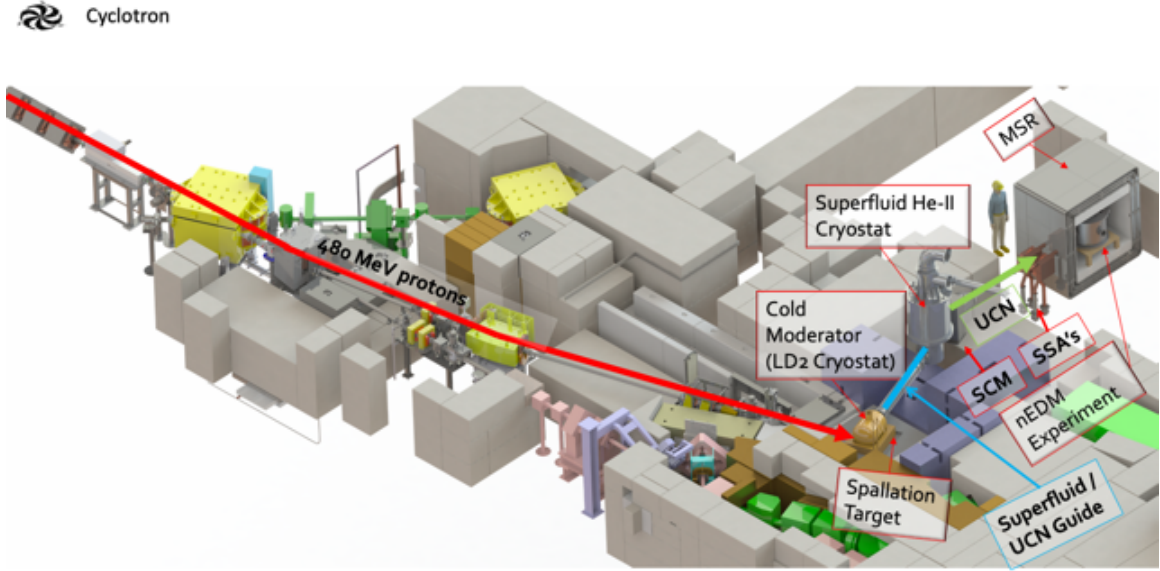


Figure 1.4: Conceptual design of the proposed TUCAN source and $nEDM$ Experiment. The major portion of the biological shielding is not shown. Protons strike a tungsten spallation target. Neutrons are moderated in the LD₂ cryostat and become UCN in a super fluid ⁴He bottle within, which is cooled by the superfluid ⁴He cryostat. UCN pass through guides and the superconducting magnet (SCM) to reach the $nEDM$ experiment located within a magnetically shielded room (MSR). Simultaneous spin analyzers (SSA's) detect the UCN at the end of each $nEDM$ experimental cycle.

The proposed TUCAN facility and $nEDM$ experiment is shown in Fig. 1.4. A proton beam at 480 MeV and 40 μA from the cyclotron impinges upon the tungsten spallation target liberating fast neutrons. Above the target is a neutron moderator

system containing liquid deuterium (LD_2) which creates a large flux of cold neutrons (CN). The CN enter a bottle surrounded by the LD_2 which contains superfluid ^4He below 1 K. In the superfluid, the CN excite phonon and roton transitions, losing virtually all their kinetic energy to become ultracold.

Once a sufficient density of UCN has built up, a UCN valve opens. The UCN are transported out of the source by reflection on the surfaces of UCN guides. A superconducting magnet (SCM) transmits one neutron spin orientation in the magnetic field, giving near-unity UCN polarization and facilitating transmission through a vacuum-isolation foil at room temperature. The UCN are then transported to the nEDM experiment by additional guides. At the end of each nEDM experiment cycle, simultaneous spin analyzers (SSA's) detect the UCN.

As mentioned above, a major challenge for all nEDM experiments is the generation of a sufficiently homogeneous and stable magnetic field in which to perform the Ramsey measurement. The particular magnetic field requirements for the TUCAN nEDM experiment are presented in Chapter 2, along with a description of the principles of active magnetic field compensation (AMC), which is the subject of this work. Chapters 3 and 4 describe the AMC prototype and control methods developed in the thesis, while Chapter 5 provides a detailed quantification of the systems performance. In Chapter 6, I summarize the four key findings of the thesis and provide a number of recommendations for a final AMC system suitable for the TUCAN nEDM experiment.

Chapter 2

Overview of Magnetic Field Systems

This chapter describes the magnetic field requirements for the TUCAN nEDM experiment. The magnetic subsystems which are required to achieve the magnetic field requirement are introduced. I have also briefly reviewed the current status worldwide of the use of active magnetic shielding for nEDM measurements.

2.1 Magnetic Field Requirements for TUCAN nEDM

Experiment

The magnetic field requirements to achieve 10^{-27} e-cm sensitivity level for TUCAN nEDM experiment are the following:

- The experimental magnetic field $B_0 \sim 1 \mu\text{T}$.

- The drift in B_0 should be less than ~ 1 pT over one nEDM measurement cycle.
- The inhomogeneity in B_0 should be less than ~ 1 nT/m over the fiducial volume of the nEDM experiment.

A particularly challenging aspect is that the TUCAN nEDM experiment will be located in the fringe field of TRIUMF cyclotron. At the location of the experiment, the fringe could be as large as 7 – 8 times the magnetic field of the Earth ($\sim 376 \mu\text{T}$) with $\sim 100 \mu\text{T}/\text{m}$ gradients [54]. Furthermore, large changes due to external magnetic sources are possible. These sources include nearby beam line magnets or the movement of large magnetic objects such as the 50-ton crane in Meson Hall. In general, the cyclotron field is very stable. During quiet times ~ 100 nT fluctuations are observed which are consistent in scale with typical drifts in Earth’s magnetic field and typical laboratory environments. But the fluctuations during the day could be as large as $\sim 16 \mu\text{T}$ due to movement of the 50-ton crane based on measurements done in 2012. The magnetic field information will be quantified in near future with new fluxgates which are being set up in the Meson Hall [55].

We need several approaches combining active and passive magnetic shielding in order to insulate the experimental volume from the extraneous magnetic fields. The general approach is shown in Fig. 2.1. The nEDM experiment will be placed inside a magnetically shielded room (MSR). Surrounding the MSR will be a suitably designed array of electromagnetic coils that will provide active shielding, or compensation, of the cyclotron and other background fields. Collectively the active compensation system and MSR will nullify external fields in the region of the experiment. The internal coil system will generate the magnetic fields for the Ramsey cycle. The

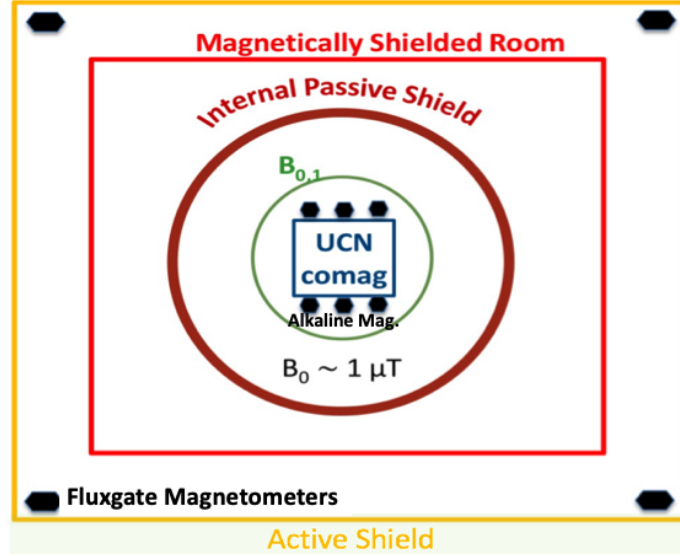


Figure 2.1: Schematic diagram for the TUCAN nEDM magnetic field systems. From outside in: The active compensation system external to the magnetically shielded room (MSR). Internal to the innermost of the four passive shielding layers of MSR, there is internal coil system (B_0 and B_1 coils) followed by the alkaline magnetometers, UCN, and the comagnetometers.

alkaline magnetometers will measure the presence of vertical magnetic field gradient. For compensating B_0 field fluctuations, ^{199}Hg co-magnetometer will be used.

2.1.1 Active Magnetic Shield

The active magnetic field compensation (AMC) system will control the magnetic field immediately outside the outermost passive shielding layer. The AMC consists of a system of fluxgate magnetometers and coils to characterize and control the environment around the magnetic shields in a feedback loop.

The coils will reduce $\sim 16 \mu\text{T}$ fluctuations (for example from crane movement) to

$\sim 1 \mu\text{T}$ – 100 nT in the 10 Hz to DC frequency range in all three directions by active feedback from the array of fluxgate sensors. The fluxgate sensors will be placed near the compensation coils and the passive shields. The feedback loop goal correction rate is maximally 6 Hz. The goal correction rate is set by the following considerations:

- The upper limit should be $< 8 \text{ Hz}$ to reduce potential of inducing spin flips or shifts on precession frequency where the precession frequencies are $\sim 8 \text{ Hz}$ for ^{199}Hg co-magnetometer and $\sim 30 \text{ Hz}$ for neutrons in the nEDM experiment in a $1 \mu\text{T}$ field [56].
- The lower limit should be $\gtrsim 1 \text{ Hz}$ considering changes due to the sources in Meson Hall of TRIUMF for example how fast a crane moves, how fast other large resistive magnets might be ramped as well as change of Earth’s field with time.

In the $\sim 400 \mu\text{T}$ fringe field of the cyclotron, saturation of the passive magnetic shielding system can be a concern, which would seriously impact its effectiveness. The AMC could be used to reduce this field if necessary. However, its dynamic range would need to be increased substantially, possibly necessitating two independent magnetic control systems. Furthermore, when accessing the experiment, the door to the MSR must be opened. If exposed to a large external field, the inner layers of the passive shielding system could themselves become magnetized, necessitating degaussing and additional experimental down time. This could be another reason to reduce the external field below $\sim 400 \mu\text{T}$.

The point of the above discussion is that the requirements are not fully specified at this time but these are some ideas of what the requirements might be. Section 6.3

discusses in more detail some ideas about the implementation at TRIUMF.

2.1.2 Passive Magnetic Shield

The task of the passive magnetic shielding system is to provide a magnetically stable environment to perform the precision low-field NMR spectroscopy on the neutrons. Generally, the passive magnetic shielding system is composed of a thin multi-layer shields with materials having high magnetic permeability such as mu-metal. The outer layers are usually cylindrical [57, 58] but they can also take the same forms as the MSR [51, 53]. The innermost layer can be designed to include its response to the B_0 coil to achieve required homogeneity of the experimental field [59, 60]. The TUCAN nEDM experiment will employ a MSR consisting of four nested mu-metal enclosures as its passive shielding, conceptually similar to Ref. [51].

The MSR will have a quasi-static shielding factor of $\sim 10^5$ to reduce ~ 100 nT fluctuations to $< \text{pT}$. The MSR for TUCAN nEDM experiment will have an inner cubic space of side-length 1.8 m and outer side-length 2.8 m, with mu-metal wall thicknesses 2 mm, 6 mm, 4 mm, 4 mm (inner to outer), equally spaced to produce this shielding factor.

2.1.3 Internal Coil System

The internal coil system must generate a highly uniform field of order $1 \mu\text{T}$ with gradients less than $\sim 1 \text{ nT/m}$ and a drift of less than $\sim 1 \text{ pT}$ over the free precession time of the UCN. This system includes a static B_0 coil, static correction coils, and an oscillating B_1 -coil.

B_0 -coil which produces the $1 \mu\text{T}$ magnetic field provides the quantization axis for Larmor precession. Correction coils which carry a relatively small current are required to null remnant transverse fields and gradients (typically 300 pT/m) over the nEDM measurement cell. High-precision current supplies ($\sim 1 \text{ ppm}$) will be used to drive these DC internal coils.

A B_1 -coil operating at $\sim 30 \text{ Hz}$ is used in the Ramsey resonance method for $\pi/2$ spin re-orientation. AC coils will apply the $\pi/2$ pulses for the UCN and comagnetometer species, to initiate free spin precession. The UCN need a second $\pi/2$ pulse to complete the Ramsey sequence. They are then drained and their spins measured along the quantization axis.

2.1.4 Internal Magnetometry

A comagnetometer is used to measure and correct for B_0 field drifts. In the comagnetometer, optical pumping is used to polarize a vapor of ^{199}Hg atoms which are then introduced into the nEDM cell at the same time as the neutrons, and the spin-precession frequencies of both species are measured simultaneously. It is called a comagnetometer because both species occupy the same volume at the same time. A continuous measurement of the precession frequency of the comagnetometer can be used to normalize the magnetic field drifts. Normally, drifts of $1 - 10 \text{ pT}$ in B_0 field may be corrected to the $\sim 10 \text{ fT}$ level using the comagnetometer technique in a typical nEDM experiment.

The motion of the comagnetometer atoms and neutrons within the EDM cell in the presence of a magnetic gradient causes frequency shifts that reverse sign with \mathbf{E}

reversal [45, 61, 62]. Both the comagnetometer and UCN are affected, but comagnetometer effects tend to dominate due to the higher (thermal) velocity of the atoms.

A number of alkaline magnetometers are placed just outside the nEDM measurement cell. They are used to characterize magnetic homogeneity and stability. The chief purpose is to characterize gradients, in order to characterize the leading contributions to false EDMs arising from Hg and UCN motion in the EDM cell.

2.2 Review of the Active Magnetic Compensation Systems Developed for Other nEDM Experiments

Several active shields have been built since the 1980s for applications like ion beams, bio-magnetism [63–68], all the way to the nEDM experiments [69, 70]. The first active magnetic field compensation system used in an nEDM experiment was at PSI in 2013 [69]. The main application was to stabilize and reduce the effect of the neighbouring superconducting test facilities, SULTAN and EDIPO, which are roughly 30 m away and can produce $\sim 50 \mu\text{T}$ fluctuations at the experimental site. Such external perturbations can influence the magnitude of B_0 field as well as change the magnetization of the mu-metal shielding producing remanent magnetic fields. Due to this more time is spent on degaussing after such events which reduces the nEDM measurement time significantly. Moreover, SULTAN and EDIPO can also reverse the direction of the magnetic field in the horizontal plane at the experimental site.

For active magnetic compensation at PSI, six rectangular coils ($6 \text{ m} \times 8 \text{ m}$) were

used to create three orthogonal sets of Helmholtz-like coils. The currents in these coils were controlled dynamically via a proportional-integral feedback loop. The algorithm was a starting point for my work and is described in Chapter 4. Reference [69] has pointed out the ill-conditioned problem of the matrix in the feedback algorithm and solved the problem by using matrix regularization.

In 2016, Ref. [70] also discussed a large-scale active shield that was designed, built, and characterized to compensate and cancel external magnetic fields in real-time for the Munich nEDM experiment. The design was mainly based on simulations and optimization processes and the active shield was composed of 24 compensation coils and 180 field probes. The feedback algorithm was similar to that in Ref. [69]. In addition to matrix regularization [69] for noise reduction, Ref. [70] also implemented signal correlations which only affected the proportional (P) term of the feedback control algorithm. Signal correlations prevented the active compensation system from adding unnecessary noise to a stable field. The position of the 3-axis sensors and their quantity were optimized by a Monte Carlo method making use of the field maps of all 24 coils and the combined ambient field. This active magnetic compensation system reduces the static field surrounding the passive shields by roughly 10 times, while the dynamic mode improves the stability by more than one order of magnitude.

In 2018, Ref. [71] presented the concept of active magnetic field compensation system for the n2EDM upgrade at PSI. Reference [71] discussed a new method of grid-based magnetic field coil design where the predefined grid may be shared between multiple coils and demonstrated by a small-scale active magnetic shield. Reference [71] suggested that the n2EDM shield will perform better by tailoring it for

the particular magnetic environment and by providing coils for high-order variations. A mobile tower with magnetic sensors was built to map the magnetic environment at the n2EDM experimental site. The position and orientation of the magnetic sensors attached to the the mobile tower were continuously measured with string potentiometers while mapping. Reference [71] pointed out the importance of the condition number and empathized building a well-conditioned system rather than regularizing an ill-conditioned system.

In 2013, Ref. [9] introduced a prototype active magnetic compensation system. The system was constructed and tested at the University of Winnipeg for the development of active magnetic compensation for the TUCAN nEDM experiment. The system was based on the measurement of magnetic fields from a 3-axis fluxgate sensor, centered in a 3-axis Helmholtz-like coil set in absence of the passive magnetic shielding. A proportional-integral-derivative (PID) feedback algorithm was used to drive the field to zero. A Helmholtz-configuration perturbation coil was built to test the active shielding ability of the feedback system. The system was capable of reducing reducing tens of μT magnetic field variations to the level of tens of nT. The RMS shielding factors were found to be > 1000 for magnetic field perturbation frequencies ≤ 20 mHz, and > 100 for frequencies ≤ 0.5 Hz. Ref. [9] found that the shielding factors were proportional to the sampling frequency, inversely proportional to the perturbation frequency, and limited by the broadband noise of the background.

2.3 Overview of the AMC prototype development

The overall objective of this thesis was the development of a prototype AMC system for the TUCAN nEDM experiment that offers feedback control of multiple compensation coils based on an array of fluxgate sensors. As mentioned already, an earlier prototype had been assembled at the University of Winnipeg and successfully tested in a basic mode of operation [72]. I successfully implemented, commissioned, and characterized the multi-dimensional control system for the prototype based on the works of Refs. [69, 70], as described in Chapters 3, 4, and 5. To meet the design goal of 6 Hz and reduce high frequency noise, I built 4th-order low-pass Butterworth filters. To understand the prototype performance and solve various problems I encountered, I completed a quasi-static magnetic simulation of the system, and made a time-dependent simulation of the PI feedback and control algorithm. The prototype now operates successfully with multi-dimensional control. My key contributions, along with recommendations for a future AMC system, are summarized further in Chapter 6.

Chapter 3

Active Magnetic Compensation

Prototype

A prototype active magnetic compensation system was built and tested at the University of Winnipeg. This chapter describes the components of the prototype and their performance. The multi-dimensional feedback algorithm which corrects fluctuations is discussed in the next chapter. The system was designed to compensate fluctuations on the scale of those of the background field in the laboratory. Customization of a future AMC system for the scale and magnetic environment of the TUCAN nEDM experiment can be done based on the experience gained with the prototype.

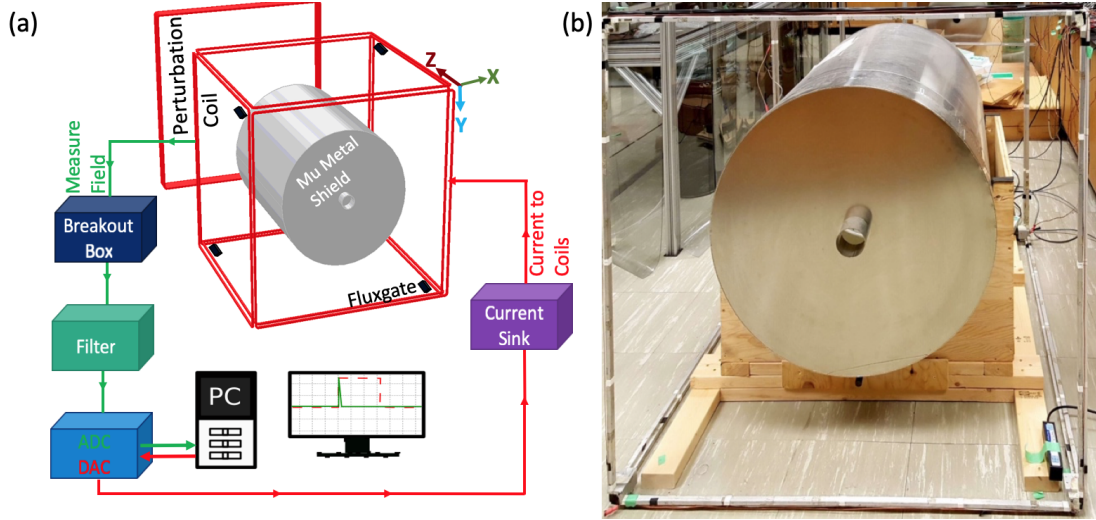


Figure 3.1: AMC Prototype at the University of Winnipeg. The schematic diagram is shown in (a) and a photograph in (b). Surrounding the outermost mu-metal passive shielding layer are six coils on six faces of a cubic Al frame. A seventh coil provides additional perturbations to the field. The magnetic environment is sensed by the 3-axis fluxgates. The filters remove high-frequency noise. Fluxgate signals are recorded by an ADC and a computer uses a multi-dimensional feedback algorithm to control the currents in the coils via DACs and current sinks.

3.1 Overview of AMC Prototype

A schematic diagram of the prototype is displayed in Fig. 3.1(a). A picture of the coils and magnetic shield is shown in Fig. 3.1(b). The magnetic background fluctuation was known to be ~ 100 nT (see Section 3.8) over the course of a day. The prototype has been designed to compensate that through the six current-carrying single-loop coils on the six faces of a cubic frame. A cylindrical multi-layer, mu-metal shield sits at the centre of the coils. This combined system represents a roughly one-third scale model

of the eventual TUCAN nEDM experiment. An additional coil, located $\sim 1 - 2$ m away from the prototype, serves to generate known magnetic field perturbations for quantitative characterization. The properties of the mu-metal shields are discussed further in Section 3.2 and the coil cube in Section 3.3.

Four 3-axis fluxgate sensors were placed at positions near the shield and coil system to measure the field for compensation. Another 3-axis fluxgate sensor was placed at the center of the passive shield for quantification of the prototype. Details of the fluxgate sensor system are discussed in Section 3.4.

It was found that the fluxgate signals were dominated by 60-Hz electrical noise from the background. A further concern is that if the AMC system itself generates substantial feedback at ~ 8 Hz in a $1 \mu\text{T}$ field, it could induce changes in the ^{199}Hg free precession. As a result, a number of 4th-order low-pass Butterworth filters with corner frequency 10 Hz were built to reduce the noise. The filter details are prescribed in Section 3.7. After filtering, the signals are transmitted to the computer via the analog to digital converter (ADC) of a LabJack T7 Pro [73]. The required currents are calculated in a computer (PC) using a proportional-integral (PI) control algorithm. The computer uses digital to analog converters (DACs) to control six voltage controlled current sinks. The current sinks drive the six compensation coils.

More details of each component are discussed in the following sections.

3.2 Mu-Metal Shields

The passive magnetic shielding is composed of thin multi-layer shields with materials having high magnetic permeability (mu-metal). In the prototype at UW, there are

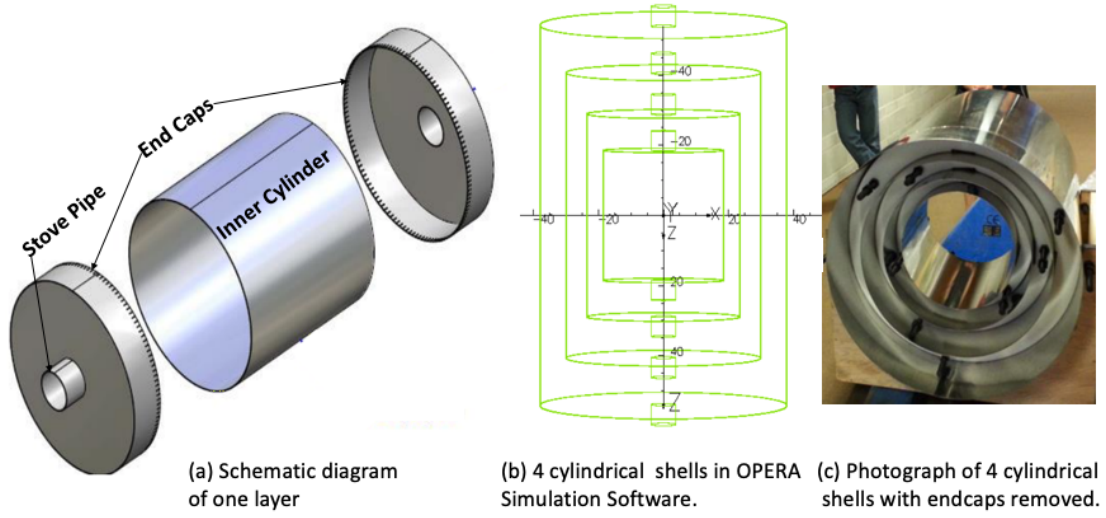


Figure 3.2: Prototype passive shielding at the University of Winnipeg (UW) [74].

four layers of cylindrical shields enclosing a volume of interest as shown in Fig. 3.2. Each shell is enclosed with end caps as shown in Fig. 3.2(a). Amumetal (Magnifer 7904) of thickness 0.0625 inch has been used for the layers, which is an 80% Nickel-Iron alloy. The shields were fabricated and annealed by Amuneal Manufacturing Corp. [75]. There are two end-caps on each cylinder with a hole of 7.5 cm diameter at the center. To minimize the leakage of the external fields into the progressively shielded inner volumes, a stove-pipe of length 5.5 cm is placed on each hole (see Fig. 3.2(a)).

Parameters	Innermost Layer	2 nd Layer	3 rd Layer	Outermost Layer	Stove Pipe
Radius (cm)	18.5	23.5	30	38	3.7
Length (cm)	37	55	71	90	5.5

Table 3.1: Dimensions of prototype passive shielding layers including stove pipes radius and length.

The radii and lengths of the four layers including the stove pipes are shown in Table 3.1. A combined DC shielding factor $\sim 10^6$ is expected. A discussion about another prototype of similar design but smaller in size can be found in Ref. [76], where a shielding factor of $\sim 10^7$ was measured using a very sensitive magnetometer.

3.3 Coil Cube

As discussed in Section 3.1, the prototype has been designed to compensate ~ 100 nT magnetic background fluctuations by introducing six current carrying closed loop coils on six faces of a cube surrounding the outermost mu-metal shield. To achieve this a single turn coil was wound on each of the six sides ($1.5 \text{ m} \times 1.5 \text{ m}$) of an aluminium frame. The coils, which can be powered independently, are designated as C_x^\pm , C_y^\pm and C_z^\pm (Fig. 3.3) and are sometimes referred to as compensation coils because they are responsible for compensating magnetic fluctuations. In addition, there is a perturbation coil namely P_z^+ , which is used to apply additional field for testing purposes. Figure 3.3 also displays the numbers 1-8 indicating possible positions of the fluxgate sensors, which will be discussed in the next section.

The compensation coils have been chosen to be single turn to have small resistance ($\sim 0.15 \Omega$) and small inductive reactance. The perturbation electro-magnet coil has the same dimensions but 77 turns. The perturbation coil was typically placed parallel to the same face of the C_z^+ coil, separated by 1.06 m. Coil properties are summarized in Table 3.2.

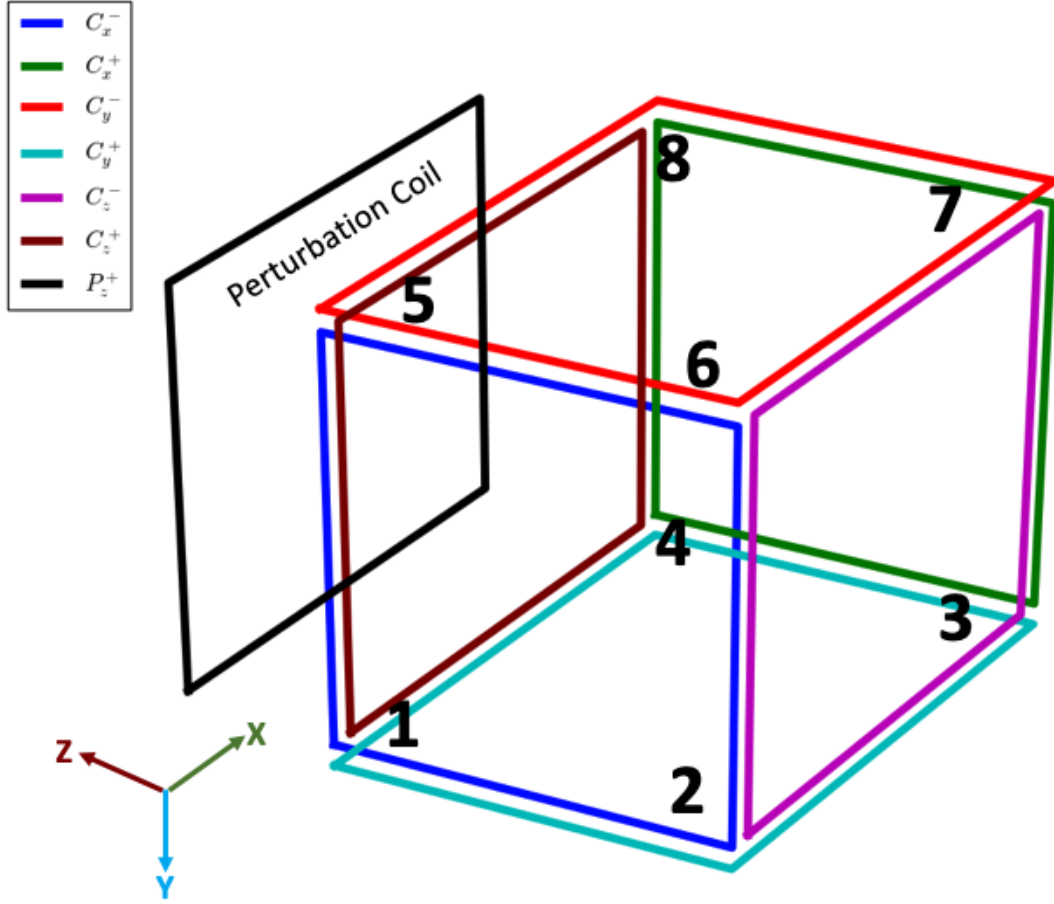


Figure 3.3: Schematic diagram indicating the coil configuration and naming scheme, as well as the numbered locations of the fluxgate sensors.

Parameters	Compensation Coils (C_x^\pm , C_y^\pm and C_z^\pm)	Perturbation Coil (P_z^+)
Dimension (m \times m)	1.15 \times 1.15	1.15 \times 1.15
No. of Turns	1	77
Resistance (Ω)	0.15	11.55
Inductance (mH)	0.32	24.62

Table 3.2: Coil dimensions and electrical properties.

3.4 Fluxgate Sensors

The fluxgate is a well-known magnetic sensor [77, 78]. For the AMC prototype, four 3-axis fluxgate sensors (2 Bartington Mag-03 and 2 Bartington Mag690) were placed at different positions within the compensation coils to measure field for compensation. Beside those, one 3-axis fluxgate sensor (Bartington Mag690) was placed at the center of the prototype for quantification of its performance. The numbering 1-8 in Fig. 3.3 indicates possible positions of the fluxgates. In addition to those, more positions were also used which would be discussed in Chapter 5. A breakout box was built to provide power to each of the four fluxgate units and to separate each of x -, y - and z -axis readouts, resulting in 12 analog outputs. Figure 3.3 also defines the direction x , y and z for the fluxgates. The properties of the fluxgate sensors that are used for the prototype are shown in Table 3.3 and collected from the manufacturer [79].

Parameters	Mag-03	Mag690
Measure Range (μT)	± 70	± 100
Noise Level ($\text{pT}_{\text{rms}} / \sqrt{\text{Hz}}$ at 1 Hz)	< 6	≥ 10 to < 20
Bandwidth (kHz)	3	1

Table 3.3: Properties of the fluxgate sensors used for the prototype.

According to the manufacturer, the typical noise levels are from $< 6 \text{ pT}_{\text{rms}} / \sqrt{\text{Hz}}$ and ≥ 10 to $< 20 \text{ pT}_{\text{rms}} / \sqrt{\text{Hz}}$ at 1 Hz for Mag-03 and Mag690 respectively. The noise level of the fluxgates were measured to be found that they matched the manufacturer’s specification. For the test, data was taken by placing each fluxgate inside the shield

and field data recorded. The data was processed in Mathematica [80] to estimate the power spectral density using a discrete Fourier transform (DFT) [81]. Figure 3.4 shows that the noise level is $\sim 16 \text{ pT}_{\text{rms}} / \sqrt{\text{Hz}}$ at 1 Hz for the Mag690. This also confirms that the ADC (Section 3.5) does not present any substantial noise beyond the fundamental noise of the fluxgate.

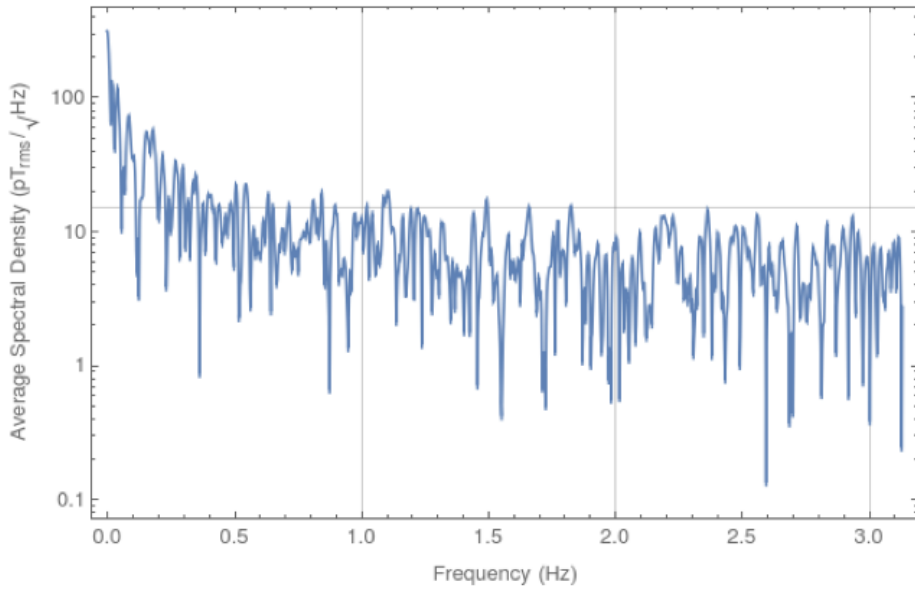


Figure 3.4: Average Spectral Density for Mag690.

3.5 Data Acquisition (DAQ) Module

A LabJack T7 Pro Data Acquisition (DAQ) module [73] was used for analog to digital conversion of the fluxgate signals. The performance and characterization of the LabJack’s analog to digital converter (ADC) is presented here. The same unit, with an additional expansion module, was used a digital to analog converter (DAC) to control coil currents, as discussed in the next section.

In addition to the standard 16-bit ADC with range ± 10 V, the LabJack T7-Pro is equipped with a 24-bit sigma-delta ADC. The effective resolution can be varied from 16 to 19.1 bits when analog conversion occurs on the 16-bit ADC, and from 19.6 to 21.8 bits on the 24-bit ADC with gain 1 [73]. For testing, a short jumper was used to connect a test channel with ground and 512 successive readings, and the mean of those readings were stored. The root mean square (RMS) calibrated voltage differences from the mean was calculated as ΔV_{RMS} . This was converted to bits using

$$\text{Effective Resolution} = \log_2 \left(\frac{\Delta V_{\text{FSR}}}{\Delta V_{\text{RMS}}} \right), \quad (3.1)$$

where $\Delta V_{\text{FSR}} = 20$ V is the ADC full-scale range for gain = 1 used for this study.

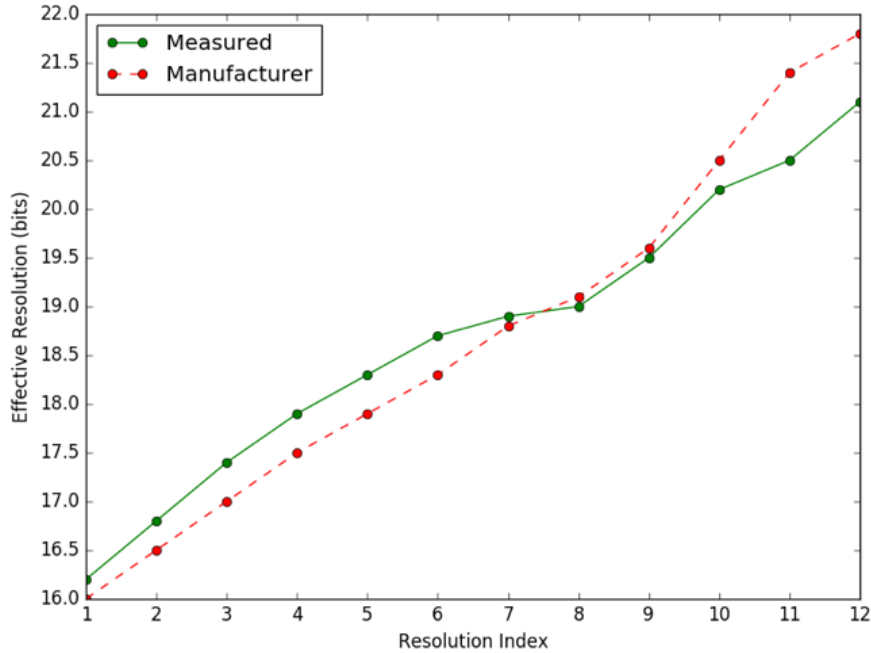


Figure 3.5: Effective resolution for different resolution index for gain 1 and ± 10 V range. A higher resolution index will result in lower noise and higher effective resolution but increases sample times.

Figure 3.5 compares the manufacturer [73] result (dashed red) with measured result (solid green) for different resolution indices. Higher resolution index means lower noise, but it also results in increased averaging times and decreased bandwidth as shown in Table 3.4. Normally, a gain of 1 was used.

Res. Index	Bandwidth (Hz) (Gain/Range: 1/± 10V)	Bandwidth (Hz) (Gain/Range: 10/± 1V)	Bandwidth (Hz) (Gain/Range: 100/± 0.1V)	Bandwidth (Hz) (Gain/Range: 1000/± 0.01V)
1	25000.0	4347.8	970.9	198.8
2	25000.0	4347.8	492.6	100.0
3	16666.7	1818.2	198.0	99.0
4	11111.1	1724.1	196.9	99.0
5	6250.0	869.6	194.2	98.0
6	3448.3	438.6	97.3	97.1
7	1785.7	392.2	94.8	94.3
8	917.4	324.7	90.3	90.1
9	285.7	285.7	285.7	285.7
10	74.6	74.6	74.6	74.6
11	15.1	15.1	15.1	15.1
12	6.3	6.3	6.3	6.3

Table 3.4: T7 Pro sample frequency for different resolution index, gain and voltage range [73].

Table 3.4 also reports sampling rates for each analog input. If more than one input

Res. Index	Loop bandwidth (Hz) for 1 channel (Gain/Range: $1/\pm 10V$)	Loop bandwidth (Hz) for 14 channels (Gain/Range: $1/\pm 10V$)	Possible Averages for 14 channels to meet design goal
1	3846.2	344.7	50
2	3846.2	328.0	48
3	3448.3	303.2	45
4	2777.8	263.8	39
5	2272.7	209.4	31
6	1694.9	149.4	23
7	1204.8	95.3	15
8	694.4	55.4	9
9	237.5	19.5	3
10	71.6	5.3	-
11	15.0	1.1	-
12	6.3	0.4	-

Table 3.5: T7 Pro loop frequency for different resolution index with gain 1 achieved in the setup at UW. Possible loop bandwidth for 14 channels and software averaging to meet design goal is also shown.

is used, the overall sample rate suffers accordingly since the same ADC is used. In addition, there are delays due to computation time, which results in an overall slower response which we call the loop sampling frequency (Table 3.5). For resolution index 1, it is found to be 3846.2 Hz, which is smaller than the effective sampling frequency

25000 Hz reported in Table 3.4 because of polling time which is typically 1 ms per channel read [73]. The polling time includes LJM library overhead, Linux overhead, USB communication time, and device processing time. Table 3.5 also shows the possible loop bandwidth for 14 fluxgate axes that have been used for active magnetic compensation. Possible software averaging is also shown in Table 3.5 to meet the 6 Hz system design goal. Resolution index 1 – 9 are acceptable to meet the design goal. Software averaging should give roughly the same noise performance which is discussed later (Chapter 5).

3.6 DAC and the Current Sink

Once the fluxgate signals have been processed in the PI control algorithm within the computer, currents must be sent to the compensation coils. DACs were used to provide analog output voltage signals. An 8-channel current sink device was built to convert those voltage signals into currents for the coils. Both the DAC and the current sink device will be discussed in this section.

An expansion module from LabJack called the LJTick-DAC provides two 14-bit analog outputs per module with a range of ± 10 V. The LJTick-DAC plugs into any digital I/O block of T7 Pro. To control the seven coils (including the perturbation coil), 4 LJTick-DACs were connected to LabJack T7 Pro via the CB15 terminal.

It was found that the field generated by one of the coils at the center of the cube was ~ 200 nT, when there was ~ 200 mA current flowing through the coil. Since the environmental magnetic fluctuations are ~ 100 nT, a 200 mA current sink was considered sufficient. The required gain of the current sink is then such that

200 mA current shall be generated over a 10 V range. In the current sink design (Fig. 3.6), it means that the sense resistor must be $R_{\text{sense}} = \frac{10 \text{ V}}{0.2 \text{ A}} = 50 \Omega$. Of the eight available channels, six were connected to the six compensation coils and our first prototype current sink was connected to the perturbation coil. The other two remaining channels were not used here. The 8-channel device is powered by 24 V at a limit of $\sim 1.3 \text{ A}$ current.

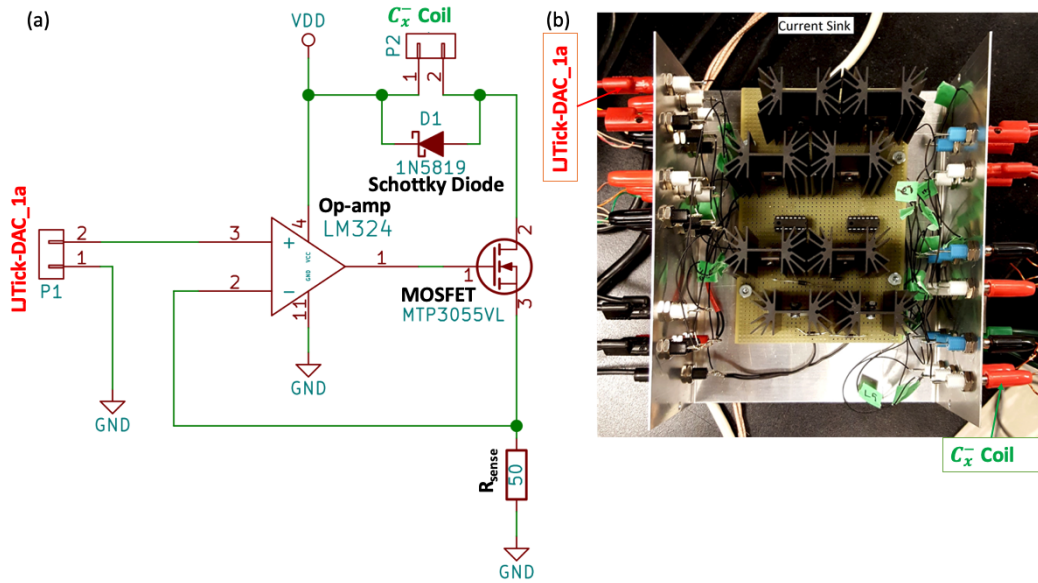


Figure 3.6: Current Sink Device. Circuit diagram of one of the voltage controlled current sink device shows in (a) and the pictorial topview of all the assembled current sink circuits shows in (b). The description is given in the text.

In the circuit diagram (Fig. 3.6(a)), the output voltage from LJTick-DAC_1a (channel a of first LJTick-DAC) is connected to the input of the current sink. The output of the op-amp is connected to pin 1 (the gate) of a power metal-oxide-semiconductor field-effect transistor (MOSFET) designed for low voltage, high speed switching applications. A Schottky diode is connected in parallel with the output

where the coil C_x^- is connected for reverse current protection. All the current sink circuits are assembled in a box and a picture is shown in Fig. 3.6(b). The current sinks were calibrated and agreement was formed with the gain of 50Ω set by R_{sense} .

Although the LJTick-DAC supports -10 to 10 V range, the current sink device uses the 0 to 10 V range for convenience, at the cost of losing one bit in resolution. If it is required to utilize the full resolution of the DACs, it's probably easier to just modify the LJTick-DACs -10 to 10 V range to a smaller unipolar range which exists on the chip just prior to the generation of the bipolar. We successfully modified one LJTick-DAC in this way, and modified R_{sense} accordingly in its current sink.

The current resolution was tested using an Agilent 34970A data acquisition device with an ammeter module in it. Results are shown in Fig. 3.7 and are in agreement with expectation.

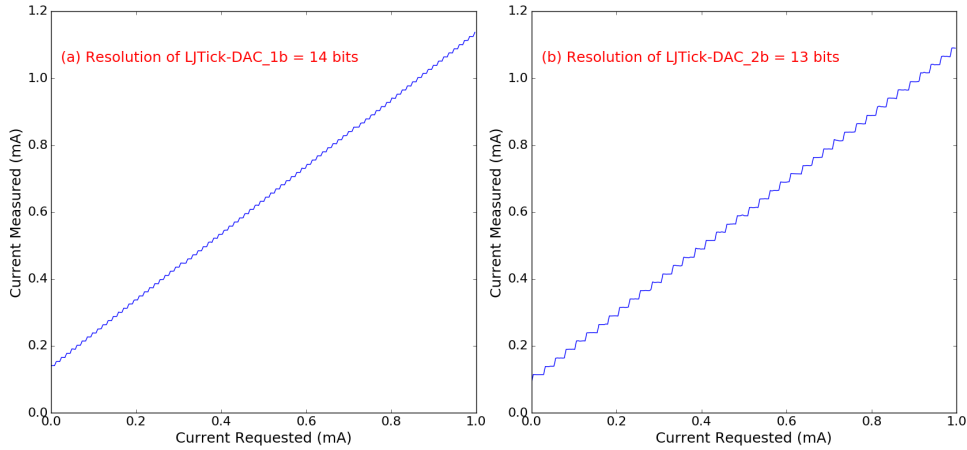


Figure 3.7: Resolution of LJTick-DACs. Currents measured (vertical-axis) with 0.001 mA increment each time for requested current (horizontal axis) from 0 to 1 mA to find the resolution of the DACs. Resolution of channel b of modified LJTick-DAC is shown in (a), and resolution of channel b of unmodified LJTick-DAC in (b).

3.7 Filtering

The raw fluxgate signals have a large amount of 60 Hz noise. In principle, the ADC can handle this by increasing the amount of averaging. This is done by increasing the resolution index (Table 3.5) but at the cost of a slower effective sampling rate (bandwidth). The noise was large enough that resolution index 12 needed to be used which was unacceptably slow, and insufficient to meet the 6 Hz design goal for the long correction rate.

To make the ADC response time faster, twelve 4th-order low-pass Butterworth filters were designed and built. The specifications of the filter are shown in Table 3.6. The voltage range had chosen to be ± 12 V same as the fluxgate sensors. So, the same power supply can be used for both the filter and the fluxgates. The cutoff frequency of the filter was selected to be 10 Hz. This is sufficient to reduce 60 Hz noise to an acceptable level while still enabling the 6 Hz goal correction rate. In addition to these filters, 3 low-pass filters are available from a Bartington signal conditioning unit (SCU1) with variable gain and bandwidth.

Voltage Range (V)	± 12
Gain (V/V)	1
Passband	-3 dB at 10 Hz
Stopband	-60 dB at 100 Hz

Table 3.6: 4th-order Low-Pass Butterworth Filter Specification

The circuit diagram of a 4th-order low-pass Butterworth filter is shown in Fig. 3.8(a). The filter was designed online via Analog Filter Wizard tool [82] to our specifications.

Two 2nd-order low-pass filters have been cascaded in series to form a 4th-order low-pass filter. The 2nd-order low-pass filters use Sallen-Key architecture which allows better passband gain without the use of the inductors. We also made a board to accommodate 3 filters (one for each axis of a fluxgate). Photographs of the implementation are shown in Fig. 3.8(b). The front side (left in Fig. 3.8(b)) contains 3 input and output terminals.

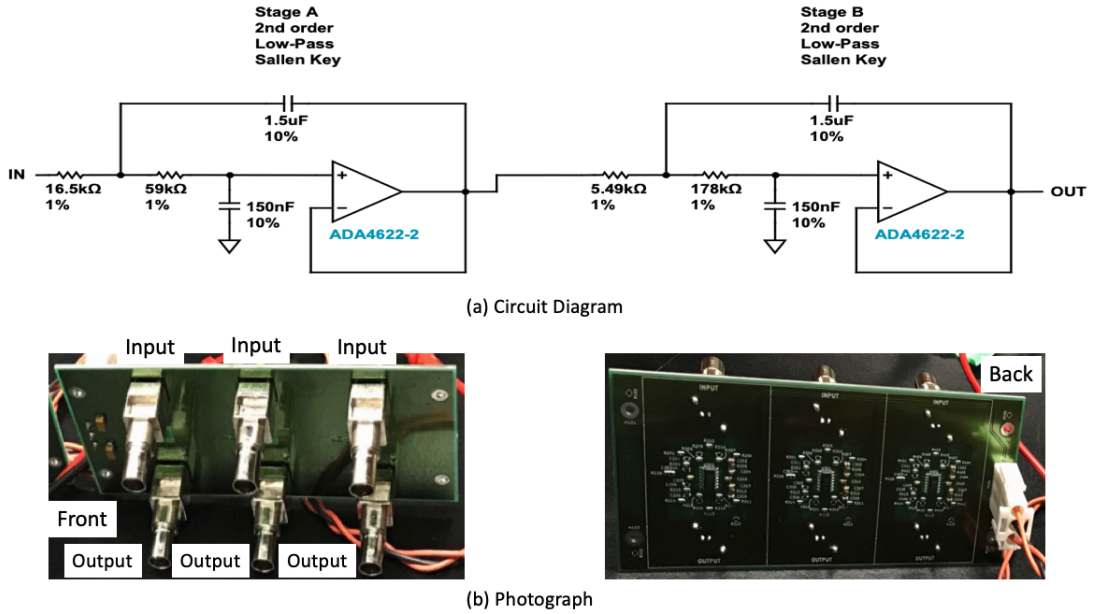


Figure 3.8: 4th-order low-pass Butterworth filter (a) circuit diagram of one filter, (b) photographs of three filter board.

To characterize the filters above, one was connected to a lock-in amplifier and the frequency varied from 1 Hz – 15 kHz with constant amplitude inputted to the filter. The output of the filter was connected to the lock-in amplifier for demodulation. The gain was then determined as

$$\text{Gain} = |V_{\text{out}}/V_{\text{in}}|, \text{ and} \quad (3.2)$$

in decibel (dB) as

$$\text{Gain (dB)} = 20 \log_{10}|V_{\text{out}}/V_{\text{in}}|, \quad (3.3)$$

where V_{in} is the signal amplitude inputted to the filter, and V_{out} is the output amplitude.

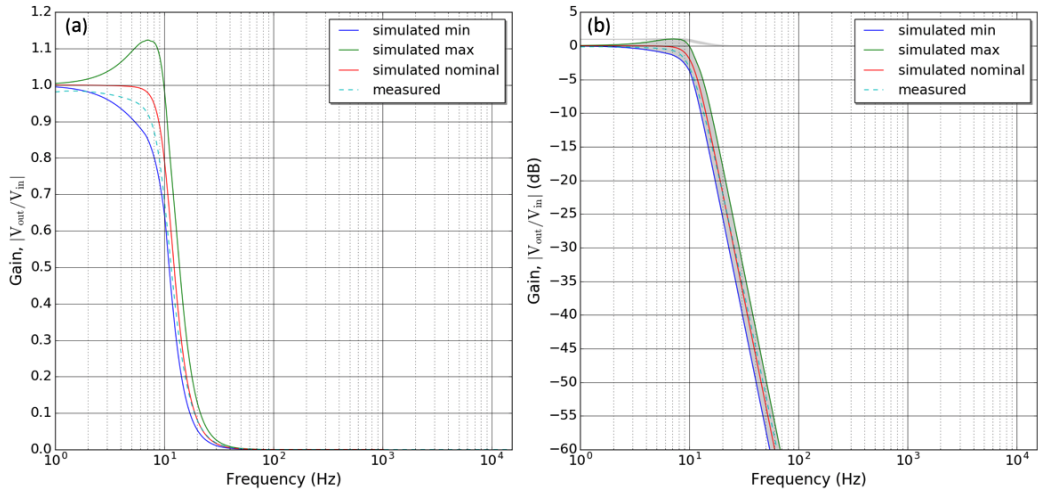


Figure 3.9: Comparison of frequency response of a 4th-order low-pass Butterworth with simulation. Vertical axis in both represents the gain. The difference between (a) and (b) is that the gain is converted to dB in (b). The curve with different colors represent different results as shown by the legends and their description is given in the text.

The frequency response for gain is shown in Fig. 3.9(a) and is compared with the simulated design values. The simulation provides an expected nominal, minimum, and maximum values based on component tolerances. It is seen that the measured value falls within the region of simulated minimum and maximum and nearly to the nominal. The same comparison is shown in dB in Fig. 3.9(b). The gain has been attenuated by ~ 3 dB at 10 Hz as expected. In Section 5.1, the results with and

without the filters will be shown.

3.8 Field Fluctuations Surrounding the Prototype

To characterize the magnetic field fluctuations, the field was measured as a function of time using one fluxgate of the apparatus. For this measurement, the passive magnetic shields were removed from the coil cube so that they would not distort the result.

The field fluctuation measurement is shown in Fig. 3.10 for one 24-hour period. The data are compared with data from the nearest space weather station (Brandon, MB, CA) [83] which is ~ 215 km away. The direction of x , y and z axis used in Fig. 3.10 are defined by the space weather station as follows: $+x =$ north, $+y =$ east, and $+z =$ vertically down. In order to compare field fluctuations more efficiently, an offset, defined by the first data points in the time series, was subtracted from all other data. The offsets were 10139 nT, 3048 nT, and 40358 nT for our case and 15108 nT, 1341 nT, and 54712 nT for the Brandon space weather station in x , y and z axis respectively.

Figure 3.10 shows that the field fluctuations level are $\sim 50 - 100$ nT for all axes in both the measurement taken at UofW and that in Brandon. In general, the two measurements track one another. The UofW data, taken in a busy building in the middle of a city, obviously suffers additional human-induced magnetic noise. Overall, the fluctuations of the magnetic field in the lab at UofW are typically ± 100 nT, as was known prior to this measurement.

Magnetic noise at 1 Hz was characterized by making a histogram of differences in

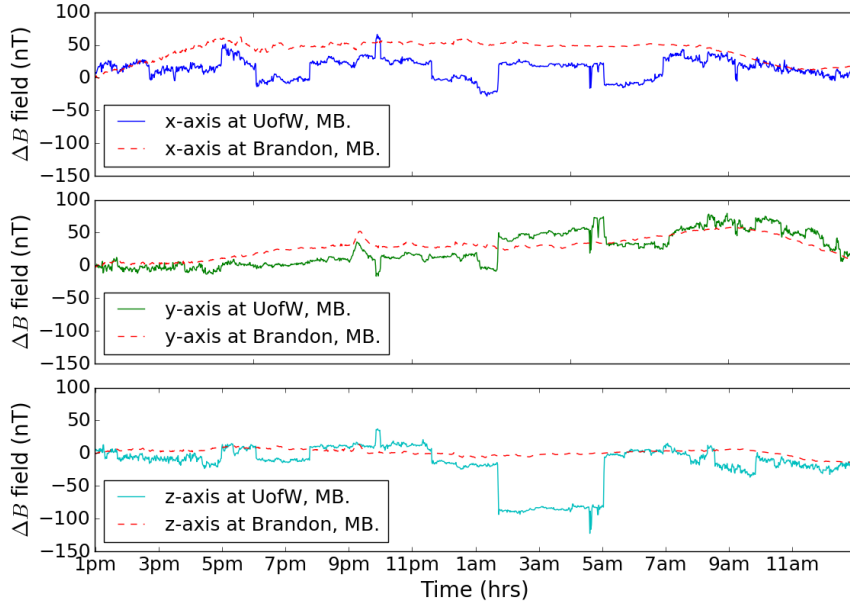


Figure 3.10: Comparison of fluctuations of the magnetic field measured at the University of Winnipeg (UofW) for 24 hours with that from the Brandon, MB space weather station. The data was taken from 1pm CST on August 29, 2018 to 1pm CST on August 30, 2018.

subsequent magnetic field measurements separated by 1 second as

$$\Delta B(1s) = B(t + 1s) - B(t). \quad (3.4)$$

The result is shown in Fig. 3.11. It is seen that the noise width at 1 Hz is ~ 1.5 nT for most sensors. This property will be used in Section 4.4.1 for generating random magnetic fields. The fluxgate sensors used are shown in the legends of the figure for x , y and z magnetic field direction. For fluxgate sensor positions see Fig. 3.3.

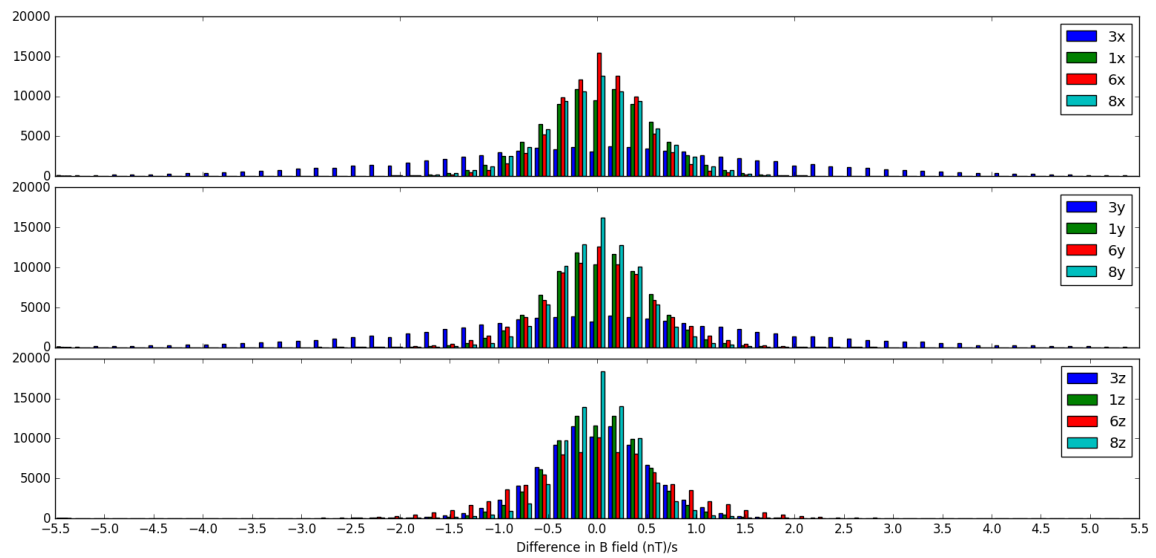


Figure 3.11: Histogram of the difference in the magnetic field for different sensor positions and axes over 24 hours starting at 1 pm CST on 29 August, 2018 in the laboratory at the University of Winnipeg.

Chapter 4

AMC Prototype Feedback and Control Algorithm

This chapter describes how the system works as a unit to provide magnetic field control. The description includes the algorithm which generates the feedback and control mechanism and some typical results from operation. It also includes the methods used in operating the system, such as tuning methods used in the control algorithm. Finally, metrics are defined that will be used to further quantify the system performance. These will be applied in Chapter 5 where more results and solutions to problem encountered in the operation of the system will be presented. Much of the work presented in Chapter 4 follows the work of others, especially Refs. [69–71]. New work that builds on these results is presented in Chapter 5.

4.1 Principle of Operation

The goal of this Section is to introduce the general idea of how the feedback system works, and to introduce the principles of operation. It also introduces a few of the key issues faced when operating the system.

Fluxgates measure the magnetic field. Each fluxgate axis has a setpoint. When the fluxgate signal drifts from the setpoint, the error grows. The fluxgates respond to changes in the coil currents in a linear fashion and can therefore be described by a matrix. The inverse matrix describes how to correct the currents based on the errors from the consecutive fluxgate signals. A Proportional Integral (PI) control algorithm is used in conjunction with the matrix inverse to correct currents based on the error signals. The matrix is not square and its inverse has to be defined. A problem arises that the matrix can be ill-conditioned, and this problem must be dealt with.

In the upcoming Sections, the mathematical definitions required to explain system operation will be discussed. Issues encountered in ill-conditioning and the mathematical principles of non-square matrix inversion will be covered and some basic results of the measurements after tuning the PI parameters will be shown. Metrics of the system performance are also discussed. Chapter 5 relates to use of these tools to characterize system performance, focusing on the novel aspects of any work.

4.2 Matrix of Proportionality Factors

As previously discussed in Sections 3.3 and 3.4, there are total 14 sensor axes and 7 coils for the prototype. Among them, 12 sensors and 6 coils are used for compensation

and others are used for quantification. The magnetic field readings change linearly with current, represented by a constant matrix \mathbf{M} . The matrix is a constant if we ignore hysteresis. This is generally a good approximation because the magnetic permeability of the nearby magnetic shields is very large.

Index	Range	Labels	Definition
c	1-6	C_x^\pm, C_y^\pm and C_z^\pm	Define specific coil
S	1-14	$1x, 1y, 1z$ or $3x, 3y, 3z$ or center- x ... center- z etc. (see Fig. 3.3)	Define the x, y and z of a specific position (Numbering based on positions). Control sensors used on the center of the prototype
s	1-12	Same as labels of S	Subset of S excluding the 2 control sensors
n	$0 < N < \infty$	1,2,3,..., N	Define no. of PI loop iterations

Table 4.1: Definition of different indices used to indicate sensor, coil and iterations in the feedback loop. Each sensor and coil also has a label which identifies it physically.

The relationship between the relative sensor readings and the coil currents is

$$B_s^n(\text{coils}) = \sum_{c=1}^6 M_{sc} I_c^n, \quad (4.1)$$

where M_{sc} are the elements of the matrix \mathbf{M} and I_c^n is the current set on the coils for a particular measurements where n runs from 0 to N for N being total number of measurements. The sum is over coils c and the sensor index s runs from 1 to 12. They are defined in Table 4.1. The field $B_s^n(\text{coils})$ refers only to the relative field, in the sense that it is the field generated at sensor s by the coil set. There could be other fields from the environment, which are the fields we seek ultimately to correct as will be discussed in the following Section 4.3.

The matrix defined in this way is easy to measure using the system. Each coil c is set to a unit current, with all other currents set to zero. The change in the sensor reading s then gives the matrix element M_{sc} .

The color map of a matrix \mathbf{M} measured in this fashion is shown in Fig. 4.1. The results are reasonable considering the design of the system. The system was designed to compensate magnetic field of order 100 nT for currents of 200 mA, which would imply the matrix elements should be of scale 500 nT/A. Generally this agrees with the color scale seen in Fig. 4.1. Furthermore, the strongest matrix elements are those where the coil is closest to the sensor in question. For example, 8y is closest to coils C_y^- and C_x^+ . It also makes sense that 8y would have strong matrix elements here because it is near the corner of the magnetic shield which causes for example the C_x^+ coil to be converted into a strong y component. The red and blue colors are a result of the definitions of positive/negative current in relation to coil in question's orientation and the sensor axis definition.

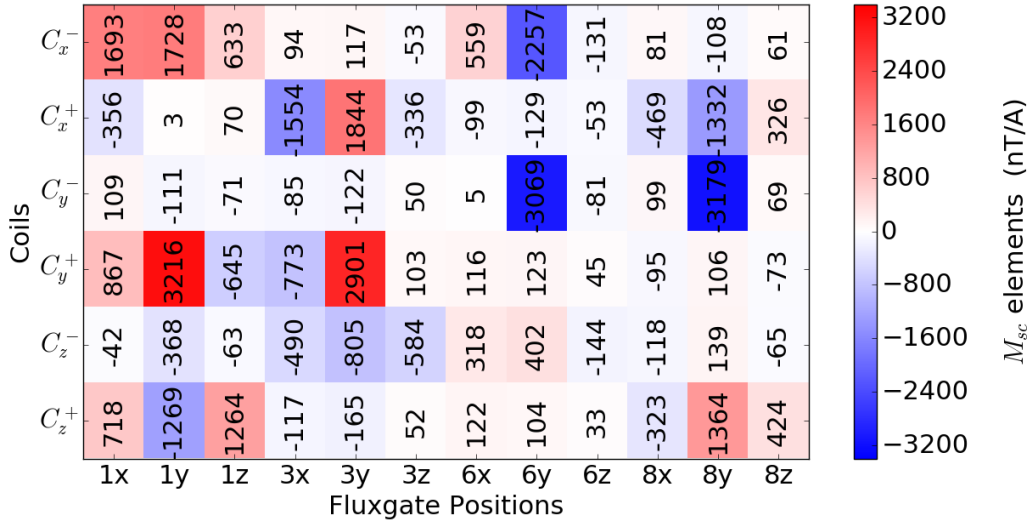


Figure 4.1: Color map of \mathbf{M} measured using the scheme indicated in the text. Horizontal axis indicates the various sensors, which are counted using the index s . Vertical axis indicates the various coils, which are counted using the index c . The color axis (z -axis) indicates the value of the matrix element. Red elements indicate positive values while blue elements indicate negative values. Elements that appear white are near zero in the matrix element.

4.3 Implementation of PI Control Algorithm

In our algorithm, the magnetic field is measured using the fluxgates and used to define the setpoints. As will be shown, when the field changes, the error in the field can be translated into an error in current based on inverting Eq. (4.1). New current values are then calculated that must be fed to the coils completing the PI control loop.

The typical magnetic field of the surroundings has been measured using a fluxgate and is reported in Table 4.2. The values are similar in scale to Earth’s magnetic field. These are the typical scale of the setpoints.

Axis	Typical B field (μ T)
x	10
y	42
z	-5

Table 4.2: Typical magnetic field values of the environment surrounding the prototype obtained from fluxgate measurements when the x , y and z axis represent the northward, vertical downward, and westward direction respectively.

For PI control, the setpoint is measured using the fluxgate array by applying 100 mA current to the coils. Our current sink (see Section 3.6) can generate 0-200 mA current. So, the 100 mA current has been chosen to utilize the full capacity of the current sink to compensate the field fluctuations in either direction. After finding the setpoint from the first measurement of the fluxgates, the change in the fluxgate signal is

$$\Delta B_s^n = B_s(\text{setpoint}) - B_s^n(\text{measure}). \quad (4.2)$$

For iteration $n = 1$, Eq (4.2) will give zero value as the first measurement is acting as to be setpoint, as explained earlier. The consecutive measurements are used in the control algorithm.

Using the relationship between the sensor readings and the coil currents as explained in Eq. (4.1) and the ΔB_s^n obtained from Eq. (4.2), the error in terms of the

current will be

$$\Delta I_c^n = \sum_{s=1}^{12} M_{cs}^{-1} \Delta B_s^n. \quad (4.3)$$

Here, M_{cs}^{-1} are the elements of the inverse of the matrix \mathbf{M} . The inversion of the non-square matrix is a subtle problem and is discussed in Section 4.4. ΔI_c^n is the error for n^{th} measurement on the basis of which the new set of currents will be calculated using a PI control algorithm. That is, the control variables in our case are the currents in the coils. The errors are also currents, those deduced from matrix inversion and magnetic sensor deviations from setpoints. In the algorithm, the new current [69] is

$$I_c^n = I_c^0 + k_c^p \Delta I_c^n + k_c^i \sum_{j=1}^n \Delta I_c^j, \quad (4.4)$$

where I_c^0 indicates the initial value of current for the set of the coils when the setpoint has been set (100 mA). ΔI_c^n is the error found using Eq. (4.3) and the sum is over iterations n . The term k_c^p is the proportional gain (P) and k_c^i is the integral reset (I) for a particular coil. The gains k_c^p and k_c^i terms need to be tuned properly as will be explained in Section 4.5. The index c in k_c^p and k_c^i terms represents that the P and I value for for each coil could in principle be different. But throughout the thesis, same values of k_c^p and k_c^i in all six coils have been used. We found derivative term (D) in a typical PID scheme was unnecessary because it relates to optimizing fast response and our chief concern is long-term stability.

Fig. 4.2 shows a simple one-dimensional control example implementing PI control algorithm. It is seen that the magnetic field change on sensor position 1z has been compensated successfully due to coil current C_x^- .

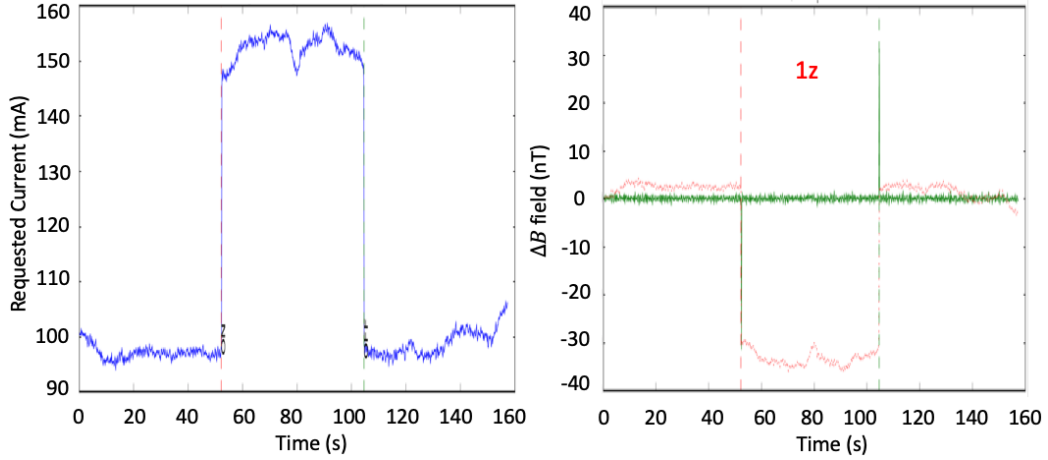


Figure 4.2: The C_x^- coil current (left) and magnetic field ΔB (right) for sensor 1z with $k_c^p = 1.0$, and $k_c^i = 0.0$. Green curve: measured field. Red curve: predicted uncompensated field (Eq. (4.20)). Vertical dashed lines indicate the time of the perturbation coil being turned on and off.

4.4 Inversion of Matrix

This Section describes in detail the inversion process of the 12×6 (sensors \times coils) non-square matrix \mathbf{M} and issues encountered. It also discusses the solution to inversion which uses regularization by random fluctuations, a strategy pursued previously by other groups.

The Moore–Penrose pseudo-inverse can be used for the inversion process. A tutorial review of the pseudo-inverse can be found in Ref. [84]. The pseudo-inverse of a matrix can be computed using singular value decomposition (SVD). SVD is a factorization or diagonalization of a matrix. The matrix can be a real or complex square or rectangular matrix. The SVD [85–87] of a real rectangular matrix \mathbf{M} with dimension

$m \times n$ and $m > n$ is

$$\mathbf{M} = \mathbf{U}\mathbf{\Sigma}\mathbf{V}^T, \quad (4.5)$$

where \mathbf{U} and \mathbf{V} are matrices with dimensions $m \times m$ and $n \times n$ respectively and \mathbf{V}^T is the transpose of \mathbf{V} . \mathbf{U} and \mathbf{V}^T are composed of the left and right singular vectors representing the orthonormal eigenvectors of $\mathbf{M}\mathbf{M}^T$ and $\mathbf{M}^T\mathbf{M}$ respectively. $\mathbf{\Sigma}$ is a real non-negative diagonal matrix with the same dimension as \mathbf{M} and can be written as

$$\mathbf{\Sigma} = \begin{bmatrix} \Sigma_{11} & 0 & \cdots & 0 \\ 0 & \Sigma_{22} & \cdots & 0 \\ \vdots & \vdots & \ddots & \vdots \\ 0 & 0 & \cdots & \Sigma_{nn} \\ \vdots & \vdots & \vdots & \vdots \\ 0 & 0 & \cdots & 0 \end{bmatrix}, \quad (4.6)$$

where $\Sigma_{11}, \dots, \Sigma_{nn}$ are diagonal values of $\mathbf{\Sigma}$ with $\Sigma_{11} \gg \dots \Sigma_{nn} \geq 0$. The positive square roots of the non-negative eigenvalues of $\mathbf{M}^T\mathbf{M}$ yield the $\Sigma_{ii} (i = 1, \dots, n)$, and are called the singular values of \mathbf{M} .

The point of SVD is that this is easy to invert because the transpose of an orthogonal matrix is equal to its inverse. That is $\mathbf{U}^T = \mathbf{U}^{-1}$ and $\mathbf{V}^T = \mathbf{V}^{-1}$ and

$$\mathbf{\Sigma}^{-1} = \begin{bmatrix} \frac{1}{\Sigma_{11}} & 0 & \cdots & 0 & \cdots & 0 \\ 0 & \frac{1}{\Sigma_{22}} & \cdots & 0 & \cdots & 0 \\ \vdots & \vdots & \ddots & \vdots & \cdots & \vdots \\ 0 & 0 & \cdots & \frac{1}{\Sigma_{nn}} & \cdots & 0 \end{bmatrix}, \quad (4.7)$$

The pseudo-inverse of \mathbf{M} will be then the inverse of \mathbf{U} , $\mathbf{\Sigma}$ and \mathbf{V}^T and can be written

as

$$\mathbf{M}^{-1} = \mathbf{V}\mathbf{\Sigma}^{-1}\mathbf{U}^T. \quad (4.8)$$

Figure 4.3 shows the diagonal matrix $\mathbf{\Sigma}$ for our measured \mathbf{M} . It is a diagonal with the singular values arranged from Σ_{11} to Σ_{66} in a decreasing order, each having a non-negative value. It is also noticeable that Σ_{66} is very small compare to Σ_{11} . Since no. of coils (c) is less than no. of fluxgate sensors (s), it is easily thought of as the representation modes of the coil set. If $\Sigma_{nn} \ll \Sigma_{11}$ it means that mode corresponding to Σ_{nn} requires a much larger current in order to generate the same scale of magnetic field as for the Σ_{11} mode.

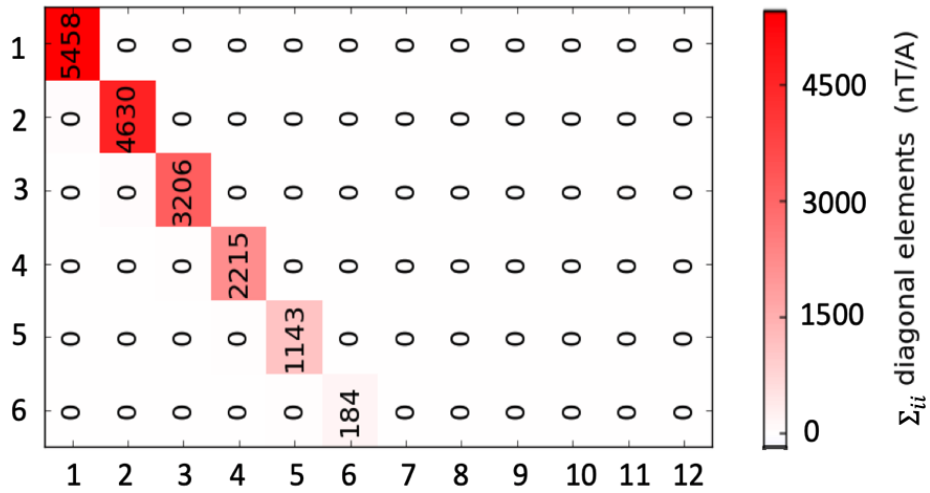


Figure 4.3: Color map of $\mathbf{\Sigma}$ for transpose of \mathbf{M} shown in Fig. 4.1. $\mathbf{\Sigma}$ is positive square roots of the non-negative eigenvalues of $\mathbf{M}^T\mathbf{M}$ in sensors \times coils dimension for 12 sensors and 6 coils in nT/A. Red elements indicate positive values while blue elements indicate negative values. Elements that appear white are near zero in the matrix element.

In Section 5.7, this effect has been analyzed further in both simulation and ex-

periment. For now, the strategy of Ref. [69] is presented which was followed initially. The strategy involves matrix regularization.

Regularization methods help to reduce the dominance of singular vectors corresponding to small singular values. Tikhonov regularization [85, 87–89] is a commonly used regularization method which solves the problem by minimizing

$$\|\Delta\vec{B} - \mathbf{M}\Delta\vec{I}\|_2^2 + \alpha^2\|\Delta\vec{I}\|_2^2, \quad (4.9)$$

where $\|\Delta\vec{B} - \mathbf{M}\Delta\vec{I}\|_2^2$ is due to the Moore–Penrose pseudo-inverse. Here, $\|\cdot\|_2$ is the Euclidean norm for vector and Frobenius norm for matrix [90, 91]. Tikhonov regularization tries to make a compromise between $\|\Delta\vec{B} - \mathbf{M}\Delta\vec{I}\|_2^2$ and $\|\Delta\vec{I}\|_2^2$ so that both of them are smaller. Tikhonov regularization makes that possible by introducing a filter α which sets the relative importance of the two terms. The filter α modifies the diagonal elements of Σ^{-1} from Eq. (4.8) as

$$\frac{1}{\Sigma_{ii}} \rightarrow \frac{\Sigma_{ii}}{\Sigma_{ii}^2 + \alpha^2}. \quad (4.10)$$

In Ref. [69], Tikhonov regularization has been further modified by defining $\alpha = 10^r$ nT/A where r is called the regularization parameter. If $r \rightarrow -\infty$, Eq. (4.10) becomes the same as Eq. (4.7) indicating no regularization whereas $r \rightarrow +\infty$ results in $\mathbf{M}^{-1} \rightarrow 0$ resulting no control (as no changes to currents, and independent of \vec{B}). Generally, r should be of order $\log(\Sigma_{ii})$ in order for regularization to have its desired effect of making the diagonal values of Σ^{-1} more equal to one another. For example, suppose $\Sigma_{11}=100$ and $\Sigma_{ii}=1$. The choice $\alpha=10$ results in

$$\frac{1}{\Sigma_{11}} \rightarrow \frac{100}{100^2 + 10^2} = \frac{1}{101} \text{ and}$$

$$\frac{1}{\Sigma_{ii}} \rightarrow \frac{1}{1^2 + 10^2} = \frac{1}{101}$$

and the singular values thereby become equalized.

The value of r may be selected using several iterative methods. The obtained r can be directly used in feedback algorithm to determine \mathbf{M}^{-1} . Because \mathbf{M}^{-1} appears in the definition of the error in current (Eq. (4.3)), it has also an effect on the PI parameters. The PI parameters can be tuned in concert with r by observing the effect on current response and this is studied further in Section 5.5.1.

An iterative method has been discussed in the previous study [69] to find r . This concept was applied to our system which will be discussed next.

4.4.1 Regularization by Random Fluctuation

The method of a previous study [69] was adapted for the prototype to determine a value of r by studying its effect on the ability to cancel random field fluctuations without generating unacceptably large current fluctuations.

For this method, sets of reasonable random magnetic fields (B_s^{rand}) are generated according to the normal distribution and standard deviation of 1.5 nT. As in Ref. [69], the reasonable value for the standard deviation was determined by the scale of the fluctuations seen from second to second by the sensor array (presented in Fig. 3.11). The exact value of the standard deviation will turn out to be unimportant in the way Ref. [69] finally deduces r using normalized field and current fluctuations.

Using the setpoint as zero, according to Eq. (4.2) the change in the sensed field is

$$\Delta B_s^{\text{sim}} = 0 - B_s^{\text{rand}} = -B_s^{\text{rand}}. \quad (4.11)$$

The array of the current errors as function of r due to the change in field ΔB_s^{sim} is

then calculated using the regularized pseudo-inverse using Eq. (4.3) as

$$\Delta I_c^{\text{sim}}(r) = \sum_{s=1}^{12} M_{cs}^{-1}(r) \Delta B_s^{\text{sim}} = \sum_{s=1}^{12} M_{cs}^{-1}(r) (-B_s^{\text{rand}}). \quad (4.12)$$

To estimate the overall current response from the array, the root mean square (RMS) of $\Delta I_c^{\text{sim}}(r)$ is calculated as

$$\Delta I_{\text{RMS}}^{\text{sim}}(r) = \sqrt{\frac{1}{6} \sum_{c=1}^6 (\Delta I_c^{\text{sim}}(r))^2}. \quad (4.13)$$

This is calculated as a function of r for different sets of B_s^{rand} (Fig. 4.4). With the increase of r , the current fluctuations $\Delta I_{\text{RMS}}^{\text{sim}}$ vanish as expected.

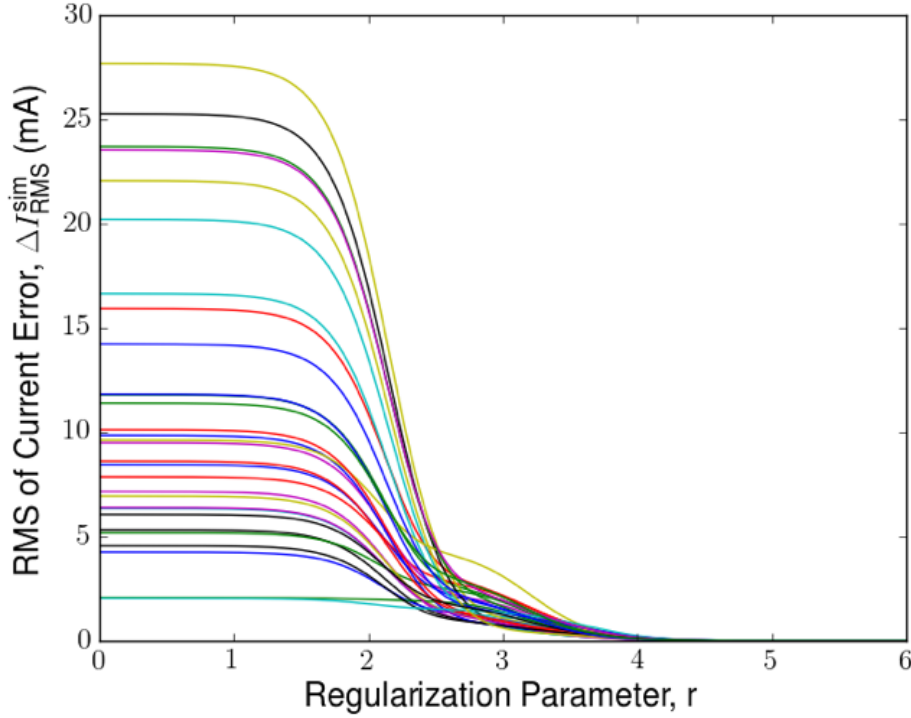


Figure 4.4: The effect of r on the coil currents for 30 different sets of B_s^{rand} generated according to the normal distribution with a central value of 0 and standard deviation 1.5 nT.

The field produced by ΔI_c^{sim} can be calculated using Eq. (4.1). The total field at each sensor s will be the superposition of B_s^{rand} and the response produced by $\Delta I_c^{\text{sim}}(r)$ *i.e.*

$$B_s^{\text{sim}}(r) = \sum_{c=1}^6 M_{sc} \Delta I_c^{\text{sim}}(r) + B_s^{\text{rand}}. \quad (4.14)$$

For a perfectly compensated system, the field produced by ΔI_c^{sim} would equal $-B_s^{\text{rand}}$ which in turn would make the $B_s^{\text{sim}}(r)$ in Eq. (4.14) identically zero. In practice, this is rarely the case. To quantify the effectiveness of the compensation, the ratio of RMS of $B_s^{\text{sim}}(r)$ to the RMS of B_s^{rand} is calculated as

$$F(r) = \frac{\sqrt{\frac{1}{12} \sum_{s=1}^{12} (B_s^{\text{sim}}(r))^2}}{\sqrt{\frac{1}{12} \sum_{s=1}^{12} (B_s^{\text{rand}}(r))^2}}. \quad (4.15)$$

The function $F(r)$ would be zero for a perfectly compensated system and unity for an uncompensated system. In Ref. [69], $F(r)$ is called the “remaining noise”. The values of $F(r)$ shown in Fig. 4.5 are for the same sets of B_s^{rand} used in Fig. 4.4. It is seen that with the increase of r , the field produced by ΔI_c^{sim} to compensate B_s^{rand} increases, resulting in more field fluctuations. It is also noticeable that the system cannot be fully compensated because $F(r)$ never goes to zero. The lowest $F(r)$ is 0.45, indicating the system will not be terribly successful at correcting random fluctuations. We think this is mainly due to the limited coil design used for this prototype, which was designed instead to focus on issues in multi-dimensional PI control.

It is seen from Figs. 4.4 and 4.5 that with the increase of r , current fluctuations decrease but field fluctuations increase. Ref. [69] suggested a compromise between them be struck to determine the value of r , *i.e.* that reducing current fluctuations ($r \rightarrow +\infty$) be traded off against reducing magnetic field fluctuations ($r \rightarrow -\infty$). To

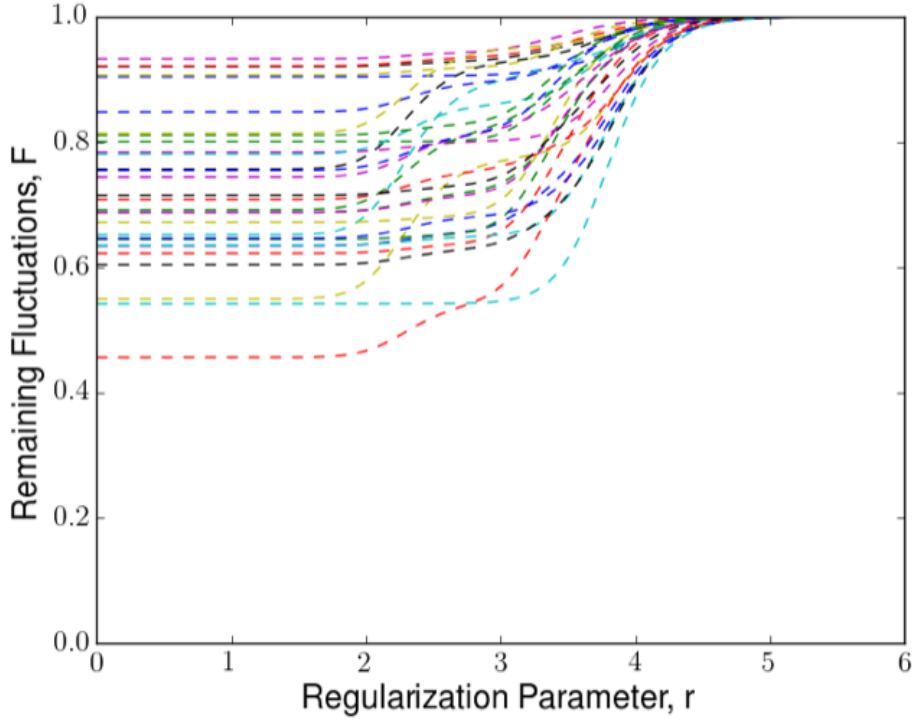


Figure 4.5: The effect of r on the effectiveness of field compensation indicated by the remaining fluctuation $F(r)$. The different curves indicate 30 different sets of B_s^{rand} .

decide the value of r , $\overline{\Delta I_{\text{RMS}}^{\text{sim}}}(r)$ and $\overline{F}(r)$ were normalized to make their range extend from 0 to 1 using

$$\overline{\Delta I_{\text{RMS}}^{\text{sim}}}(r) = \frac{\Delta I_{\text{RMS}}^{\text{sim}}(r)}{\Delta I_{\text{RMS}}^{\text{sim}}(r \rightarrow -\infty)}, \text{ and} \quad (4.16)$$

$$\overline{F}(r) = \frac{F(r) - F(r \rightarrow -\infty)}{F(r \rightarrow \infty) - F(r \rightarrow -\infty)}. \quad (4.17)$$

The effect of r on $\overline{\Delta I_{\text{RMS}}^{\text{sim}}}$ and \overline{F} is shown in Fig. 4.6. With an increase in r , $\overline{\Delta I_{\text{RMS}}^{\text{sim}}}$ decreases and \overline{F} increases as expected from the discussion earlier. Two values of r were then found for each B_s^{rand} by alternatively setting r on $\overline{\Delta I_{\text{RMS}}^{\text{sim}}}(r)$ and $\overline{F}(r)=0.5$. This is indicated schematically by the horizontal line in Fig. 4.6. The values of r so determined are averaged over a large number of B_s^{rand} ($= 30$). The optimized r in the

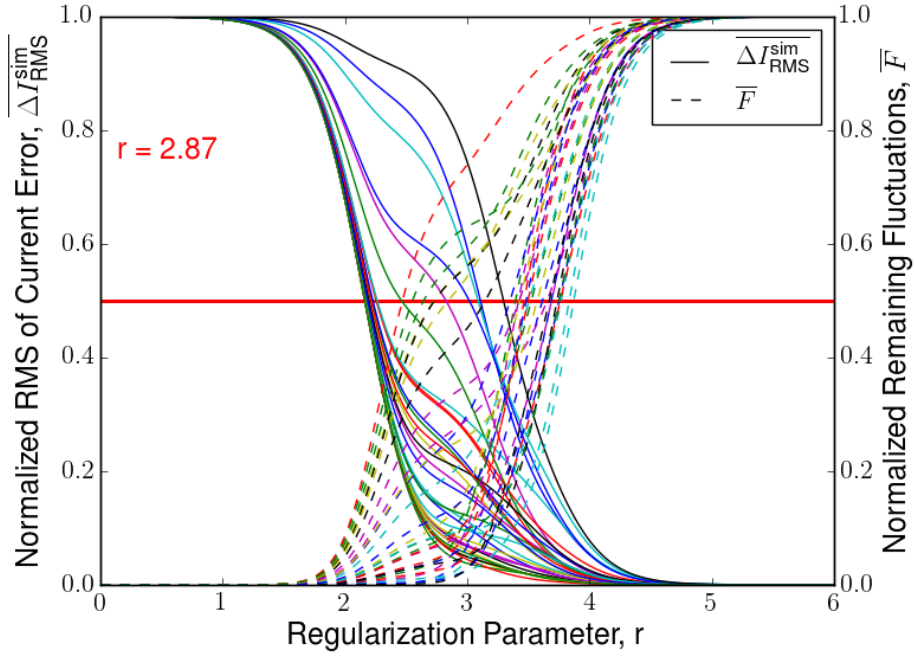


Figure 4.6: The normalized $\overline{\Delta I_{\text{RMS}}^{\text{sim}}}$ and \overline{F} for 30 sets of B_s^{rand} . The red line indicates the 0.5 level.

example of Fig. 4.6 is found to be 2.87.

The calculation to find r gives insight about the effect of regularization on current and field fluctuations, resulting in a compromise that adequately reduces both. With r in hand, \mathbf{M}^{-1} and thus the current error may be determined which is used in the PI algorithm.

4.5 Tuning of PI Parameters

This section describes the tuning of the proportional gain k_c^p and integral reset k_c^i terms appearing in Eq. (4.4) to compensate the changes in magnetic fields measured by the fluxgate sensors.

The PI parameters can be tuned using various methods [92]. A common tuning method is Ziegler-Nichols closed tuning method [93]. We usually used this method as an initial guess for the PI parameters. In the Ziegler-Nichols method, k_c^i is first set to zero and k_c^p is increased until the currents in the coils start oscillating. The k_c^p value for which the current in the coils start oscillating is denoted the ultimate gain G_u and the period of the oscillation is denoted the ultimate oscillation period T_u . The value of k_c^p and k_c^i are then determined based on the PI row of Table 4.3. Table 4.3 is a modified version of the Table 4 in Ref. [94] where the formula for integral time $T_i = T_u/1.2$ has been used and the notation and other factors have been adjusted for this case.

Controller	Gain (k_c^p)	Reset (k_c^i)
P	$0.5 G_u$	0
PI	$0.45 G_u$	$\left(\frac{0.54G_u}{T_u}\right) \Delta t$

Table 4.3: Ziegler-Nichols tuning method for P and PI controllers.

The quantity Δt in Table 4.3 is the time to complete one feedback loop iteration.

Figure 4.7 shows the first step in the tuning process. For simplicity, zoomed version of the current in coil C_x^+ is shown only. At $k_c^p=1.34$ and $k_c^i=0$, the current in the coils oscillates allowing us to identify $G_u=1.34$. The ultimate period is $T_u=0.287$ s. Now, according to Table 4.3, the proportional gain and integral reset are

$$k_c^p = 0.45 \times 1.34 = 0.60 \quad \text{and} \quad k_c^i = \left(\frac{0.54 \times 1.34}{0.287}\right) \times 0.146 = 0.37. \quad (4.18)$$

They can be further tuned for the individual coil currents if necessary but we chose not to study this. In general, we treated them as free parameters and studied the

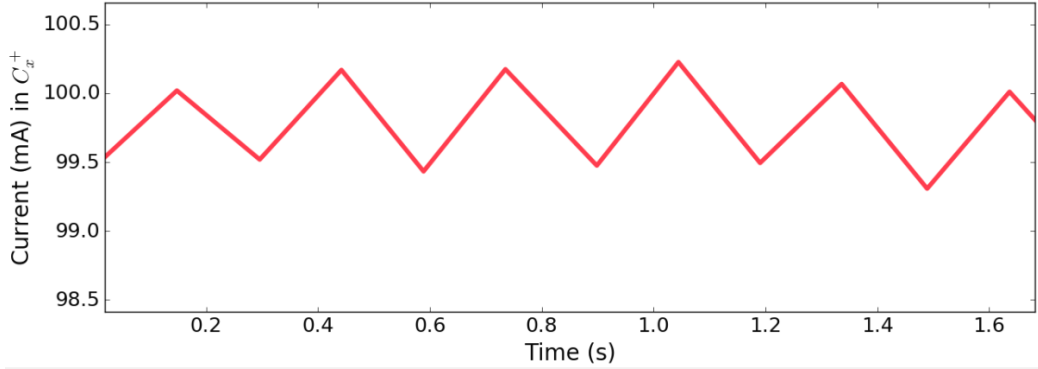


Figure 4.7: Zoomed current behaviour in coil C_x^+ with $k_c^p = 1.34$ and $k_c^i = 0$. Vertical axis represent the currents in coil C_x^+ with initial current being 100 mA. For position of the coil see Fig. 3.3.

impact of changing them on system response. More about PI tuning will be discussed in the next chapter with compensation results.

4.6 Quantitative Measures of Magnetic Compensation Performance

Three main metrics were considered, which are based on previous studies of others [69–71]. They are the following:

1. Condition Number,
2. Reduction of Magnetic Field Fluctuation and PI Behavior upon Stimulus, and
3. Allan Deviations and Shielding Factor

Each will be described. In Chapter 5, these definitions will be used to study them under various conditions.

4.6.1 Condition Number

The condition number of the matrix \mathbf{M} can be determined from the diagonal matrix Σ as

$$\text{cond}(\mathbf{M}) = \frac{\max(\Sigma_{ii})}{\min(\Sigma_{ii})} = \frac{\Sigma_{11}}{\Sigma_{nn}}. \quad (4.19)$$

The condition number of a matrix is ≥ 1 by definition. Low condition number indicates a well-conditioned matrix while large indicates an ill-conditioned matrix. Sample diagonal elements Σ_{ii} were shown in Fig. 4.3. Using Eq. (4.19), $\text{cond}(\mathbf{M}) = 5448.0/184.0 = 29.61$ which indicates an ill-conditioned matrix.

In testing the active compensation system, the goal is to have matrix condition number as close to 1 as possible. If Σ_{nn} is small (for example zero), it means that the B_s never change no matter what the current for that mode. Consequently, on inverting, large currents are driven for that mode with practically no change in the B_s . Tikhonov regularization is one method of reducing the condition number closer to 1 but later we discovered that designing a well-conditioned system is a better method. A comparison of those methods is discussed in Section 5.7.

4.6.2 Reduction of Magnetic Field Fluctuation and PI Behavior upon Stimulus

For active magnetic compensation, the measured field by the fluxgate sensors $B_s^n(\text{meas})$ is the superposition of the uncompensated field and the field created by the compensation coils $B_s^n(\text{coils})$ at the sensor positions for $n = (1, \dots, N)$ number of measurements. The uncompensated field is thus estimated to be the magnetic field without the com-

pensation effect by subtracting the $B_s^n(\text{coils})$ from the $B_s^n(\text{meas})$ *i.e.*

$$B_s^n(\text{uncomp}) = B_s^n(\text{meas}) - B_s^n(\text{coils}), \quad (4.20)$$

where $B_s^n(\text{coils})$ is determined using Eq. (4.1).

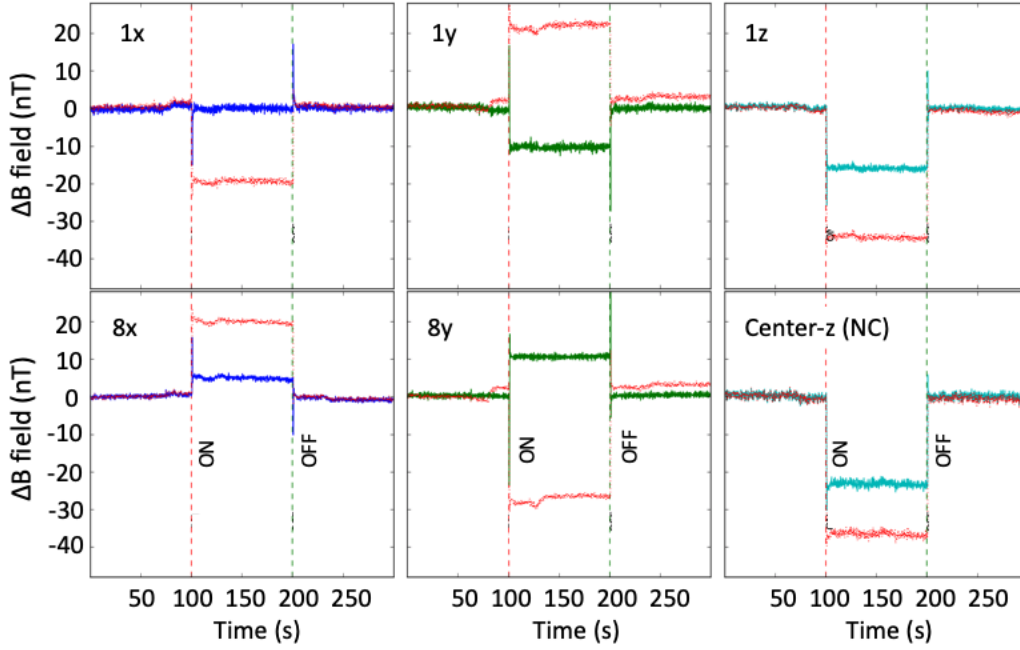


Figure 4.8: Magnetic field reduction at some of the sensors closer to the perturbation coil and the central position. Color curves: measured field change = $B_s^n(\text{meas})$. Red curves: extracted uncompensated field change $B_s^n(\text{uncomp})$. Vertical dashed lines indicate the time of the perturbation coil being turned on and off.

The PI feedback and control system can be tested by its response to a step in the perturbation coil current. This can also be studied by monitoring the central sensors within the passive magnetic shielding system. An example of this is shown in Fig. 4.8 where both $B_s^n(\text{meas})$ and $B_s^n(\text{uncomp})$ are shown. The active compensation reduces the effect of the perturbation coil current in the sensors. The response of the central

sensor is also compensated somewhat. We expect the limitation in the correction is due to limitations in the coil design.

The RMS current change and RMS field change for both the measurement and in the uncompensated case can be determined experimentally under application of the perturbation coil current.

The remaining fluctuations can also be quantified experimentally as

$$F(\text{exp}) = \frac{\sqrt{\frac{1}{12} \sum_{s=1}^{12} (\Delta B_s(\text{meas}))^2}}{\sqrt{\frac{1}{12} \sum_{s=1}^{12} (\Delta B_s(\text{uncomp}))^2}}. \quad (4.21)$$

where, $\Delta B_s(\text{meas})$ and $\Delta B_s(\text{uncomp})$ represent step changes in the measured and uncompensated magnetic fields, respectively, under application of the perturbation coil current.

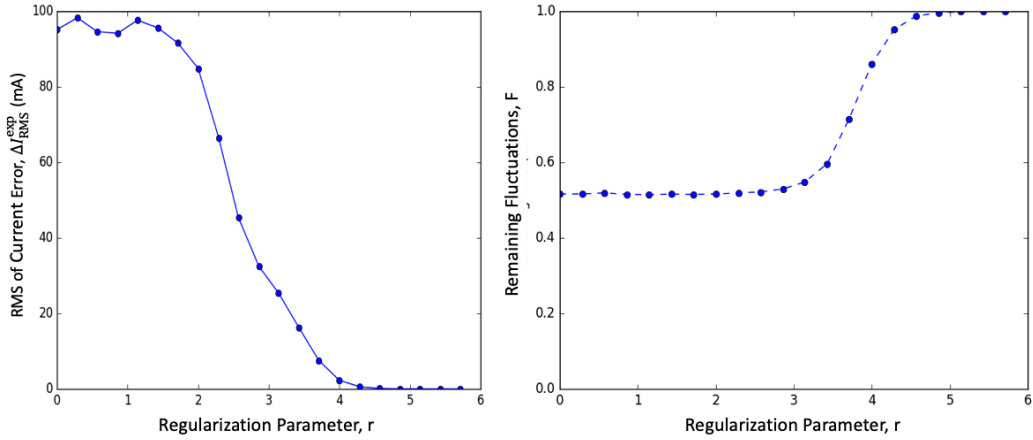


Figure 4.9: Experimentally determined effect of r on (left) RMS current change and (right) remaining field fluctuations $F(\text{exp})$ for $k_c^p = 1.0$ and $k_c^i = 0.0$. Fluxgates were located at positions 1, 2 and 7 in this study, and 100 mA current was supplied in the perturbation coil.

An example of the effect of r on the RMS current change and $F(\text{exp})$ for a partic-

ular perturbation coil current step is shown in Fig. 4.9. It is seen that around 100 mA RMS of current array is required to compensate the perturbation which eventually vanishes with r increment as expected (Fig. 4.9(a)). Furthermore, field fluctuations are reduced to 50% of their uncompensated values (Fig. 4.9(b)).

4.6.3 Allan Deviations and Shielding Factors

The Allan standard deviation [95] is used to test the time stability of clocks, amplifiers and oscillators. The same concept can be applied to time series of the magnetic field measurements. In this case, the Allan standard deviation is defined as [69]

$$\sigma_{Adev}(\tau) = \sqrt{\frac{1}{2(N-1)} \sum_{l=1}^{N-1} (\overline{B_{l+1}}(\tau) - \overline{B_l}(\tau))^2}, \quad (4.22)$$

where $\overline{B_l}(\tau)$ is the average magnetic field for a subset l over integration time τ and $\tau = \frac{T}{N}$ with T the total measurement time, and N the total number of subsets. The Allan standard deviation σ_{Adev} depends on τ as follows: $\sigma_{Adev} \propto 1/\sqrt{\tau}$ indicates the data are statistically distributed with the same mean in the values; $\sigma_{Adev} \propto \sqrt{\tau}$ indicates a random walk in the values; and $\sigma_{Adev} \propto \tau$ indicates a linear drift [96, 97].

An example of the process of calculating the Allan deviation for magnetic field data is shown in Fig. 4.10. In this example, the feedback system was switched off. The top panel in Fig. 4.10 demonstrates the eight divisions in the time series over $\tau = 128$ s-long subsets. The red line indicate the average of each subset B_l^T . The Allan deviation formula (Eq. (4.22)) is applied to these averages to arrive at the data point at $\tau = 128$ s (red star marker) in the bottom panel's Allan deviation plot in Fig. 4.10. It is seen that σ_{Adev} rises by about one decade for every two decades in

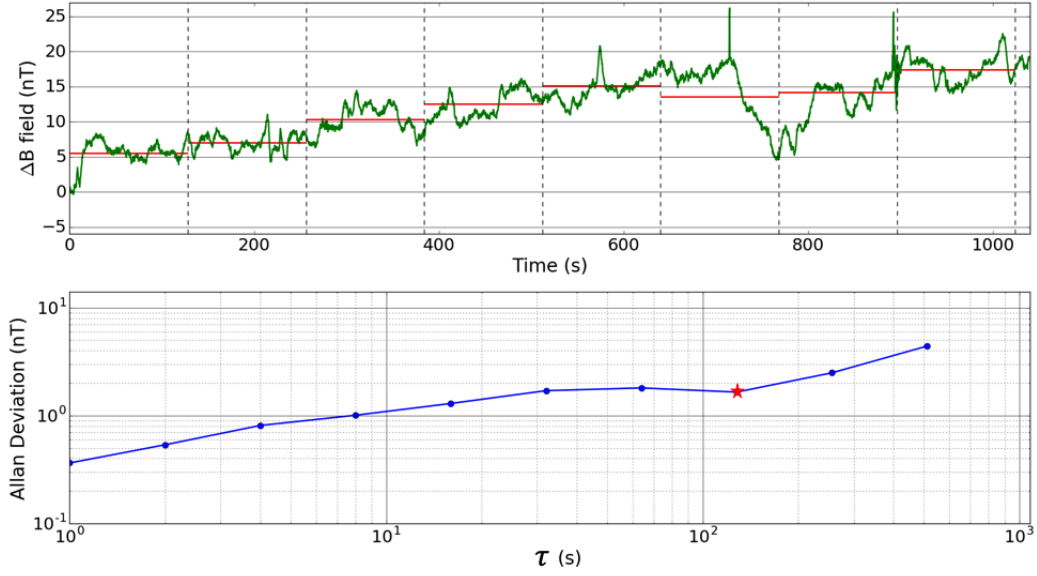


Figure 4.10: (top) Field fluctuations ΔB for sensor 8x with the feedback switched off, (bottom) corresponding Allan standard deviation. Red horizontal lines represent $\overline{B}_l(\tau)$ for 8 subsets over integration time $\tau = 128$ s separated by the vertical dashed lines.

τ . This indicates that $\sigma_{Adev} \propto \sqrt{\tau}$ which refers random walk in the field values when there is no compensation system is running. The largest integration time over which σ_{Adev} can be determined is $\tau_{\max} = T/2$ as can be seen from the horizontal axes of Fig. 4.10. The total number of subsets for τ_{\max} is $N = \frac{T}{\tau_{\max}} = \frac{T}{T/2} = 2$.

The goal of the active compensation system is to reduce the Allan deviation to be less than the Allan deviation of the uncompensated magnetic field. This would indicate that the magnetic field is more stable with compensation than without. The shielding factor [69] is defined as the ratio of Allan deviations *i.e.*

$$\text{sf}(\tau) = \frac{\sigma_{Adev}^{\text{uncomp}}(\tau)}{\sigma_{Adev}^{\text{meas}}(\tau)}. \quad (4.23)$$

The shielding factor $\text{sf}(\tau) > 1$ indicates that the magnetic environment was improved.

$\sigma_{Adev}(\tau_{\max})$ will be neglected for calculating the $\text{sf}(\tau)$. Because $\sigma_{Adev}(\tau_{\max})$ is statistically insignificant while comparing the Allan deviation measurements since there is only one subtraction in Eq. (4.22). The shielding factor is discussed further in Section 5.8.2.

Chapter 5

Quantification of Active Magnetic Compensation Prototype

In Chapter 4, the magnetic control process and the quantitative measures of the magnetic field compensation performance suggested by the Refs. [69–71] were discussed. While implementing the magnetic control process, problems occurred in terms of slow current response in the compensation coils. We did different experiments with different parameters to understand the problem and devise a solution. The system was made faster by introducing filters which enabled us to change the sample frequency without adding noise. The effect of the filter is discussed in Section 5.1. The results of PI tuning are discussed in Section 5.2, and revealed that the introduction of the integral term was related to the current drifting problem in the coils. Additional fluxgates, altering the positions of the fluxgates, and removing the passive shielding system were found to have little impact on the current drifting problem. These studies are discussed in Section 5.3. A simulation involving mag-

netic field calculations done in a finite element analysis code was combined with a PI algorithm. The simulation correctly reproduced the current drifting problem, as discussed in Section 5.4. The current drifting problem could be reduced by lowering the value of r , similar to using it as a tuning parameter, although additional noise was introduced. This is discussed in Section 5.5. In Section 5.5.2, an alternative method is proposed to find r based on lowest matrix condition number. A new control algorithm suggested by Ref. [71] was also implemented and compared with the existing one suggested by Ref. [69], and the equivalence of the algorithms (which I found) is discussed in Section 5.6. Eventually it was realized that the matrix for the prototype was ill conditioned because one of the current modes produces zero net current. The matrix condition number can be improved significantly by removing the bad coil mode which in turn eliminates the current drifting problem, as discussed in Section 5.7. Finally, the system is characterized using a number of standard metrics in Section 5.8.

New directions for future studies are presented in Chapter 6.

5.1 Sampling Frequency and Filtering

In Chapter 3, low-pass analog Butterworth filters which were built and implemented into the system were discussed. The filters were designed with 10 Hz corner frequency with the goal to remove high-frequency noise. This would allow the ADC to operate with shorter averaging, increasing its effective sampling frequency (denoted by the “resolution index” in Table 3.5). The filter gives us more freedom in terms of

- using different sampling frequencies of the ADC,

- reducing magnetic field compensation response time,
- reducing coil current response time, and most importantly
- maintaining our design sample rate with better reduction of noise.

Studies of the effectiveness of the filters in achieving these points are described in this section.

Without the filters, the noise on the fluxgate signals are dominated by 60 Hz and higher frequency noise. As a consequence, resolution index 11 or 12 was always used in order to remove this noise. Resolution index 12 would correspond to averaging over roughly 10 power line cycles (PLC), as indicated in Table 3.4, and would therefore significantly reduce the noise. The problem with this solution is that the feedback and control loop cycle time for all 14 ADC channels would be limited to ~ 0.5 Hz, which does not meet the design goal of $\gtrsim 6$ Hz.

Figure 5.1 shows an example of the importance of using the filter, comparing an unfiltered signal to one filtered by Bartington SCU1 10 Hz low pass filter, and comparing with our filter. For this study the fastest effective sampling rate (resolution index 1) has been used. The loop sampling frequency is found to be ~ 220 Hz limited by the polling time for all 14 channels and additional delays arising from LabJack communications.

It is seen that the signal is very noisy without any filter. The noise is reduced by a factor of ten using Bartington SCU1 10 Hz low pass filter. Our filters gave slightly better performance (lower noise) than the Bartington SCU1 module, likely due to slight differences in components and design. It is also seen that the outputs are limited in their time response by the filters, as expected.

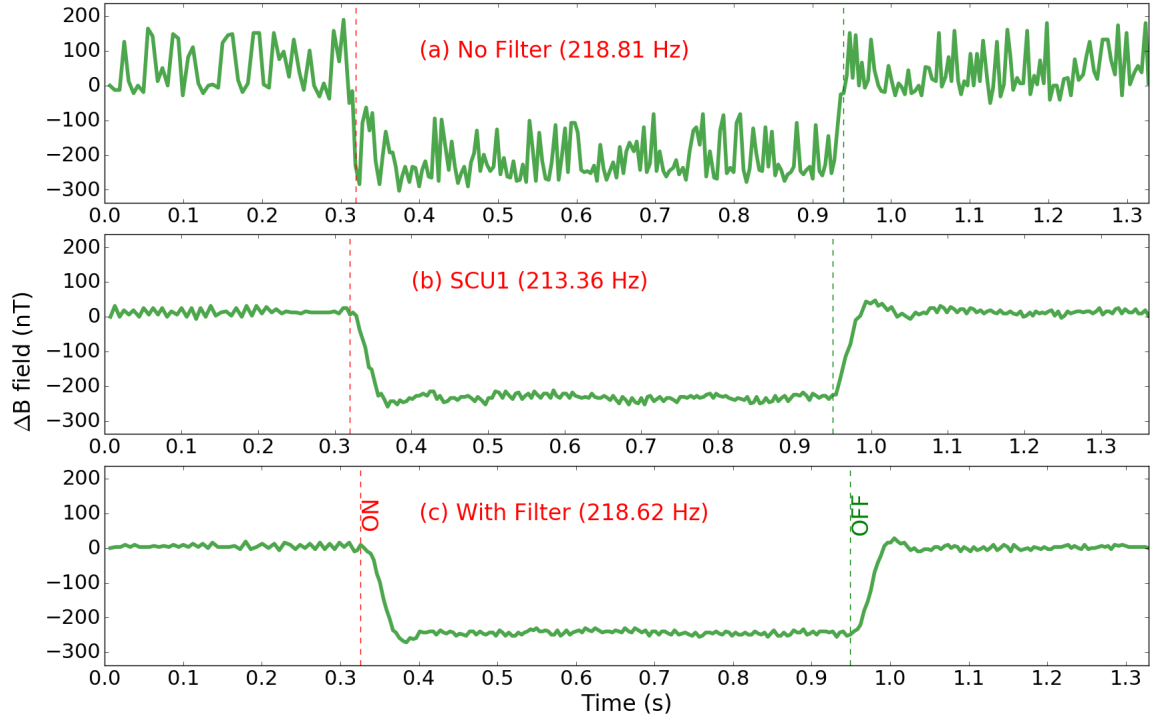


Figure 5.1: Filtering effect on the magnetic field signal measured at the 1x position. For this measurement, the PI control system was switched off so that it would not affect the noise. Vertical axis represent ΔB (see Eq. (4.2)) found from the measurement of sensor (a) without filter, (b) with Bartington SCU1 (Signal Conditioning Unit) and (c) with our filter. Vertical dashed lines indicate the time of the perturbation coil being turned on and off. The current supplied on perturbation coil was 100 mA and resolution index 1 was used for the ADC. The loop sampling frequency for (a), (b) and (c) are shown in Hz and is limited by the polling time for the 14 sensors.

The conclusion is that the filter is capable of reducing high frequency noise and allows us to go to higher effective sample rate. Given this additional freedom we can even do additional software averaging within the feedback and control loop in order to further reduce the noise.

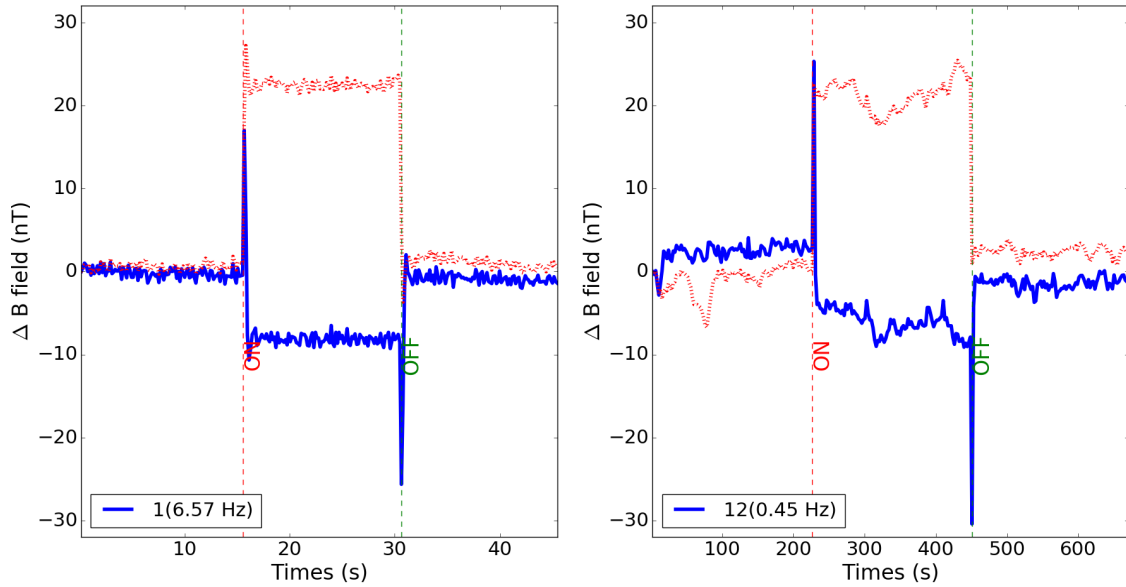


Figure 5.2: Magnetic field at sensor position 1y using resolution index 1 with 50 software averages per cycle (left) and resolution index 12 (right) when the active magnetic compensation system is switched on. Blue curves: measured field change ΔB . Red curves: predicted uncompensated field (Eq. (4.20)) change. Vertical dashed lines indicate the time of the perturbation coil being turned on and off.

Figure 5.2 shows an example of using the filters with the active compensation system switched on (left). Only one of the 14 sensors being used in the system has been displayed. In this case, 50 software averages could also be conducted, achieving a loop cycle rate of 6.57 Hz. This can be compared with the right panel of Fig. 5.2, where the analog filters were not used, necessitating PLC averaging using the largest resolution index of the ADC. In this case a loop cycle rate of 0.45 Hz is achieved. Although both schemes achieve similar noise performance, the analog filtering solution can increase the loop cycle rate by a factor of $6.57/0.45 \approx 15$. The two panels of

Fig. 5.2 appear on different time bases because the number of feedback control loops has been equalized.

Another significant problem that we faced in this experiment was that the current would drift during compensation although field would not change significantly. This is discussed further in Sections 5.2, 5.3, and 5.4. For this reason, we were often concerned with any sources of slow current response. The main point of the remainder of this section is to study the trade-offs involved in the resolution index, the loop cycle rate, and the number of software averages, and their effect on changes in the coil currents driven by the compensation system.

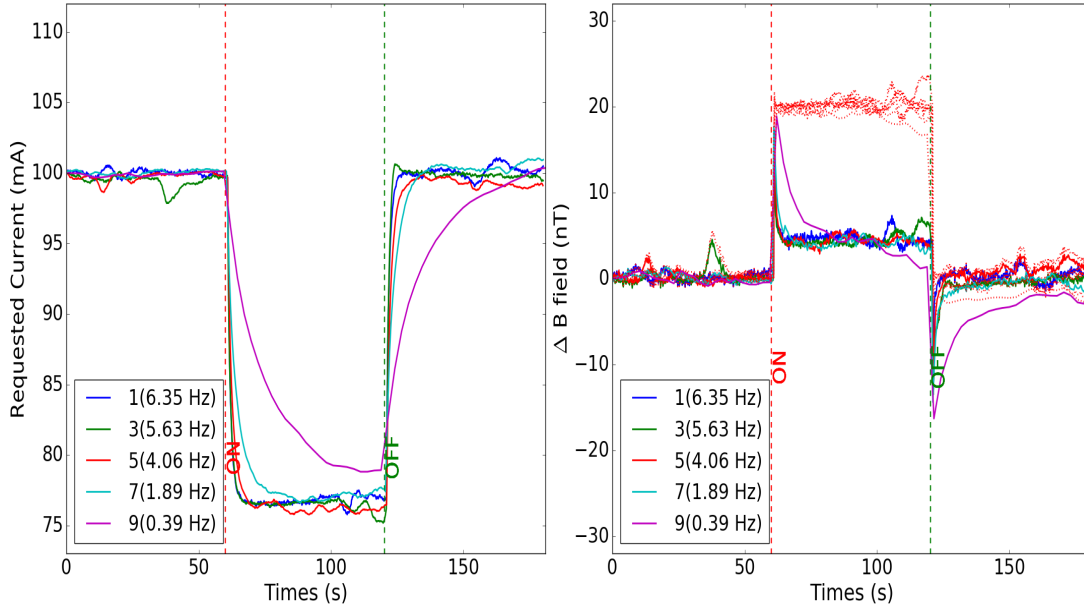


Figure 5.3: The C_x^- coil current (left) and magnetic field ΔB (right) for sensor 8x for various resolution indices. The resolution indices are represented by 1, 6, 7, 8 and 9 with the corresponding loop sampling frequencies indicated. In each case, 50 software averages were done in the loop as well. Vertical dashed lines indicate the perturbation coil state.

Figure 5.3 shows an active compensation result displaying the current in one of the 6 coils and the field in one of the 14 fluxgate axes, when the resolution index is changed. For each case, 50 software averages have always been done in the feedback loop, further reducing the loop cycle rate. Increasing the resolution index slows the response of the system, and most notably increases the current response time. For example, it takes ~ 7 s for the C_x^- coil current to settle after the perturbation coil is switched on when the loop sampling frequency is 6.35 Hz. It is also seen that the loop cycle rate slows to 1.1 Hz and 0.39 Hz by resolution index 8 and 9 respectively. The results look similar to resolution index 12 (without filter) but are generally much less noisy, and smoother over longer periods of time as well.

Another option is to run with fewer averages than 50 and at higher resolution index, while still achieving the 6 Hz loop rate design goal. Figure 5.4 shows a study where, as the resolution index is increased, the number of software averages is decreased, so as to maintain nearly the same ~ 6 Hz loop cycle rate. As expected, they all have a similar effect on the magnetic compensation result. But the coil current and magnetic field for resolution index 7 is noisier compared to others.

We expect that the advantage of resolution index 1 with larger software averaging is due to the fact that the 12 channels are sampled more continuously over the entire course of one loop cycle. This potentially gives a more accurate measurement of the true magnetic field, averaged over that cycle.

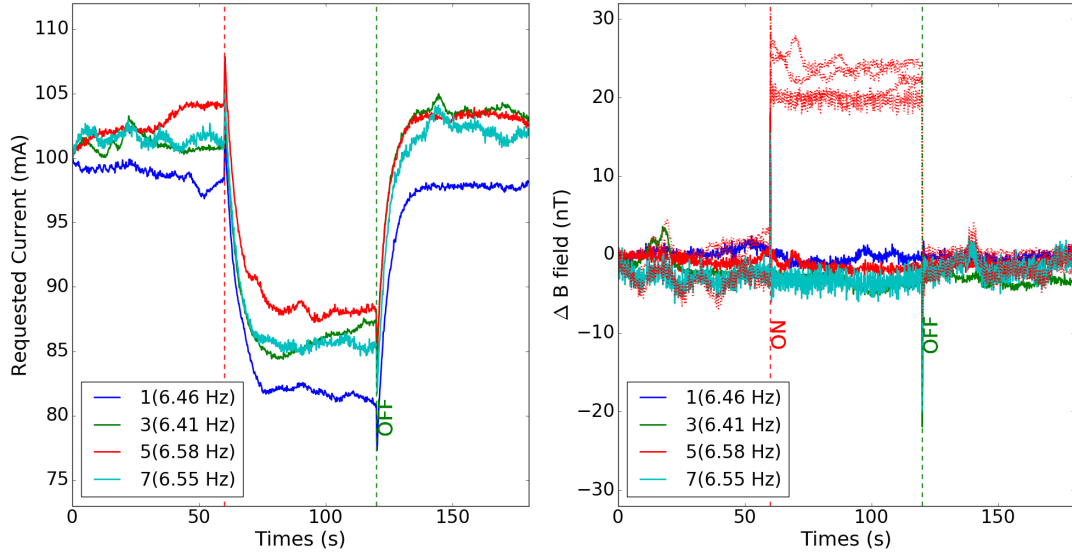


Figure 5.4: Active magnetic field compensation for resolution indices 1, 3, 5 and 7 and for 50, 45, 29 and 13 software averages respectively. These settings achieve nearly the same loop cycle rates (~ 6 Hz, indicated in parentheses). Only the C_x^- coil current (left) and ΔB for fluxgate 8x (right) are shown. Vertical dashed lines indicate the time of the perturbation coil being turned on and off.

5.2 PI Tuning General Behavior

The tuning method of proportional gain k_c^p (P) and integral reset k_c^i (I) have been discussed in Section 4.5, for example in Eq. (4.4). This Section describes the effect of changing the P and I terms on feedback system performance when they are changed individually or together.

A problem that became more apparent in the course of these studies was long-term drifting of the applied currents in the feedback system. A major conclusion of this section is that adjustments of the PI parameters could not fix this problem, which is discussed further in later sections.

5.2.1 Effect of changing P term

For these studies, the proportional gain k_c^p was varied while the integral reset k_c^i was set to zero. We expected that this would result in a form of multidimensional proportional droop. Proportional droop occurs because the proportional term contains only the instantaneous error function. A controller using only P-control therefore requires a non-zero error in order to function. This results in the error never being fully corrected and hence “droop”. Raising k_c^p can decrease the droop but will eventually result in system oscillation.

The effect of changing k_c^p is shown in Fig. 5.5. The current supplied to the perturbation coil was 10 mA when on. Resolution index 1 with 50 averages per feedback loop iteration were used. The resultant loop sampling frequency was found to be ~ 6.5 Hz.

Increasing k_c^p from 0.25 to 1.25 gives larger correction currents and better reduction of the changes induced by the perturbation coil. However this comes at the expense of larger oscillations at higher frequency in both the currents and the fields for the larger value of k_c^p . Both effects are as expected based on proportional droop.

The aggregate effect of k_c^p on the current error and remaining field fluctuations, in another similar test, is shown in Fig. 5.6. Measurements were conducted using the system for various k_c^p . Beyond $k_c^p \approx 1.3$, the system would start to oscillate. This is reflected in the RMS current error taking a value of 200 mA, which is approximately the dynamic range of the current sinks used to power the coils.

The “remaining fluctuations” F shown in the right panel of Fig. 5.6 are based on the reduction of the measured field compared to the predicted uncompensated field.

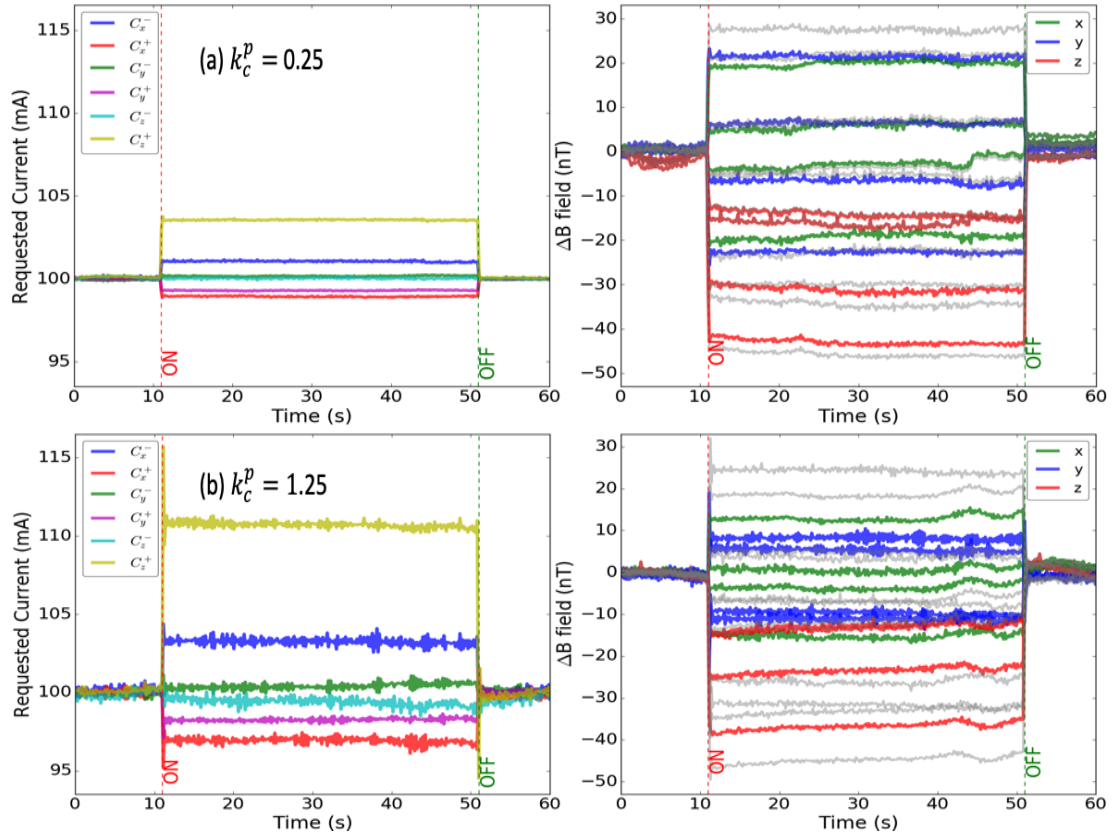


Figure 5.5: Currents (left) in all six coils (C_x^\pm , C_y^\pm and C_z^\pm) and field change ΔB (right) for 12 fluxgate axes with fluxgate positions 1, 3, 6 and 8. (a) $k_c^p = 0.25$, (b) $k_c^p = 1.25$. In both cases $k_c^i = 0$. Grey curves denote the uncompensated ΔB whereas colors indicate the compensated values with one color denoting each axis. Vertical dashed lines indicate the perturbation coil being turned on and off.

When the system is oscillating, both the measured and uncompensated fields are seen to oscillate, which is inaccurate (the uncompensated field obviously should not oscillate). As a consequence the system believes it is reducing the field fluctuations when in fact it is inducing oscillation. This is the reason the fluctuations apparently decrease in the right panel.

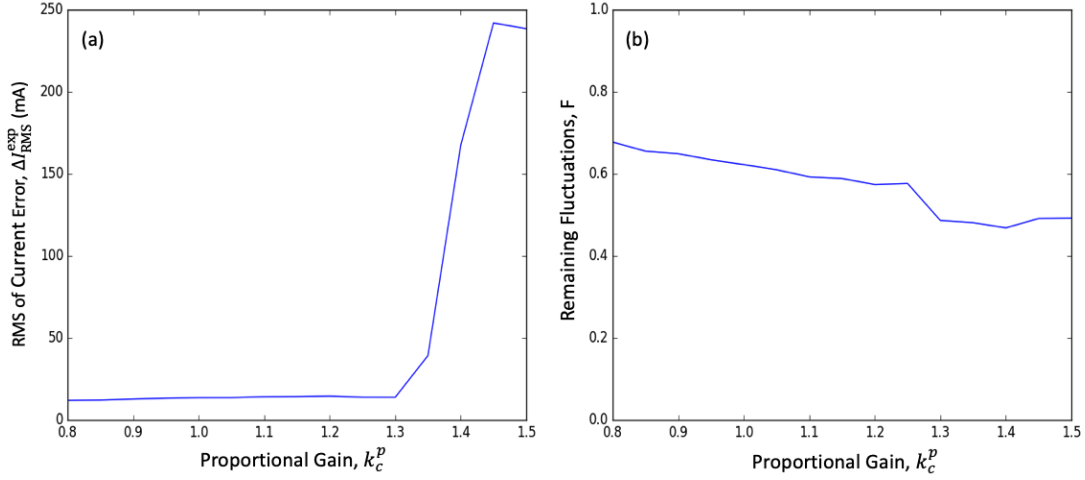


Figure 5.6: The effect of k_c^p on (a) current error and (b) remaining field fluctuations with the system operating on fluxgate positions 1, 2, and 7 (9 axes of control). Here, 100 mA current has been supplied in the perturbation coil.

We also studied the effect of varying the regularization parameter r . As expected, when r is increased, it decreases the amount of the control. The proportional gain would therefore have to be increased in order to provide compensation. Further studies of the adjustment of r are presented in Section 5.5.

The above results confirm that increasing k_c^p reduces difference between the setpoint and the actual measurements of the magnetic field, at least until the point when the system starts to oscillate.

5.2.2 Effect of the I term

In using integral reset, the error (the difference between setpoint and actual measurement) is accumulated (integrated) over the series of measurements. The accumulated error keep tracks of the offsets (proportional droop) that should have been corrected

previously. The integral reset (I) term multiplies that accumulated error with a constant gain k_c^i .

The value k_c^i also determines how fast the feedback loop will respond to changes in the error signal. A large value of k_c^i will result in a faster response. If k_c^i is increased too much, eventually it results in overshoot i.e. exceed the setpoint.

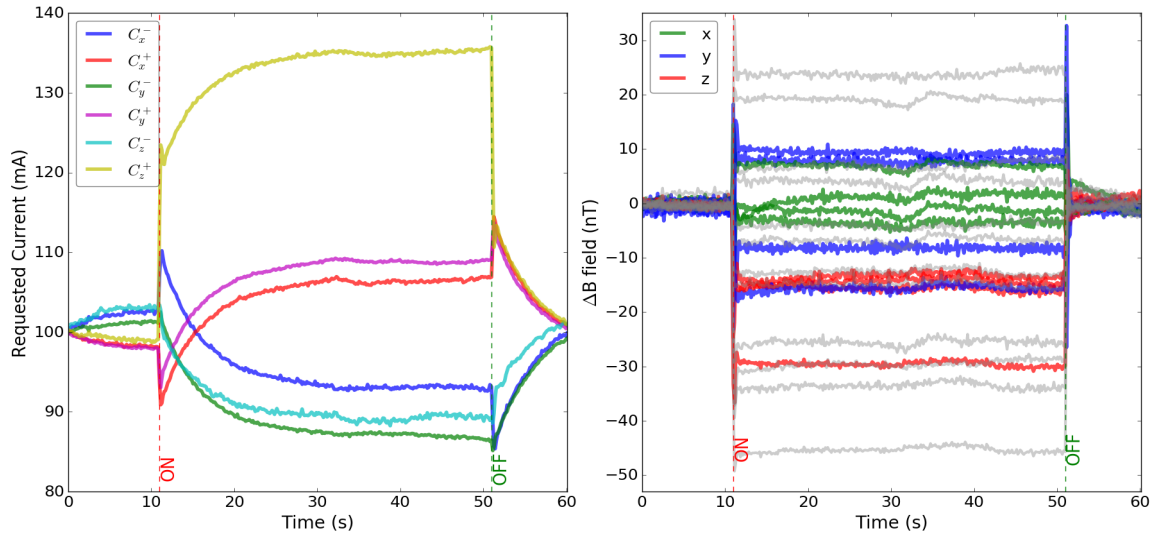


Figure 5.7: Currents (left) in all six coils with field change ΔB (right) at 12 fluxgate sensors with fluxgate positions 1, 3, 6 and 8 for $k_c^i=1.25$ with $k_c^p = 0$. Grey curves denote the uncompensated field change while color curves denote the measured field change. Vertical dashed lines indicate the perturbation coil being turned on and off.

In this study we tried running the system with $k_c^p = 0$ and then adjusting k_c^i . The results are shown in Fig. 5.7. As for Fig. 5.5, the current supplied to the perturbation coil was 10 mA when it was switched on. Resolution index 1 with 50 averages per feedback loop iteration were used. The resultant loop sampling frequency was found to be ~ 6.5 Hz.

A reasonably good value of $k_c^i = 1.25$ was used for Fig. 5.7.

It is seen that coil currents range from 137 mA to 85 mA, which is a large spread compared to Fig. 5.5. It is also seen that the range of ΔB is smaller indicating better compensation. In contrast to the right panel of Fig. 5.5, the results in Fig. 5.7 have reduced high-frequency noise. So clearly this is a system that is operating in a better state than proportional-only control.

The other observation is that in the left panel of Fig. 5.7, the currents drift for very long periods of time. This may be contrasted with the right panel of Fig. 5.7, where it is clear that the fields do not drift with such long timescales. This can also be compared with Fig. 5.5 where no such long-term drift of the currents can be seen either.

Eventually we figured out this problem was due to ill conditioning, and it is discussed further in Section 5.7. But at the stage we decided to characterize the problem further by adjusting the PI parameters to see what effect that might have.

The above results show that using only the I term provides better compensation, but then it gives rise to slowly-varying currents that take a long time to settle. We often refer to this problem as the “current drifting problem” in the remainder of this thesis.

5.2.3 Effect of adjusting both P and I

In this section, the P and I terms were tuned following the Ziegler-Nichols procedure (discussed in Section 4.5). The tuned values were found to be $k_c^p = 0.60$ and $k_c^i = 0.37$.

The results of running the system with these parameters is shown in Fig. 5.8(a). It is seen that the coil currents (left) and ΔB (right) graphs have similar pattern to

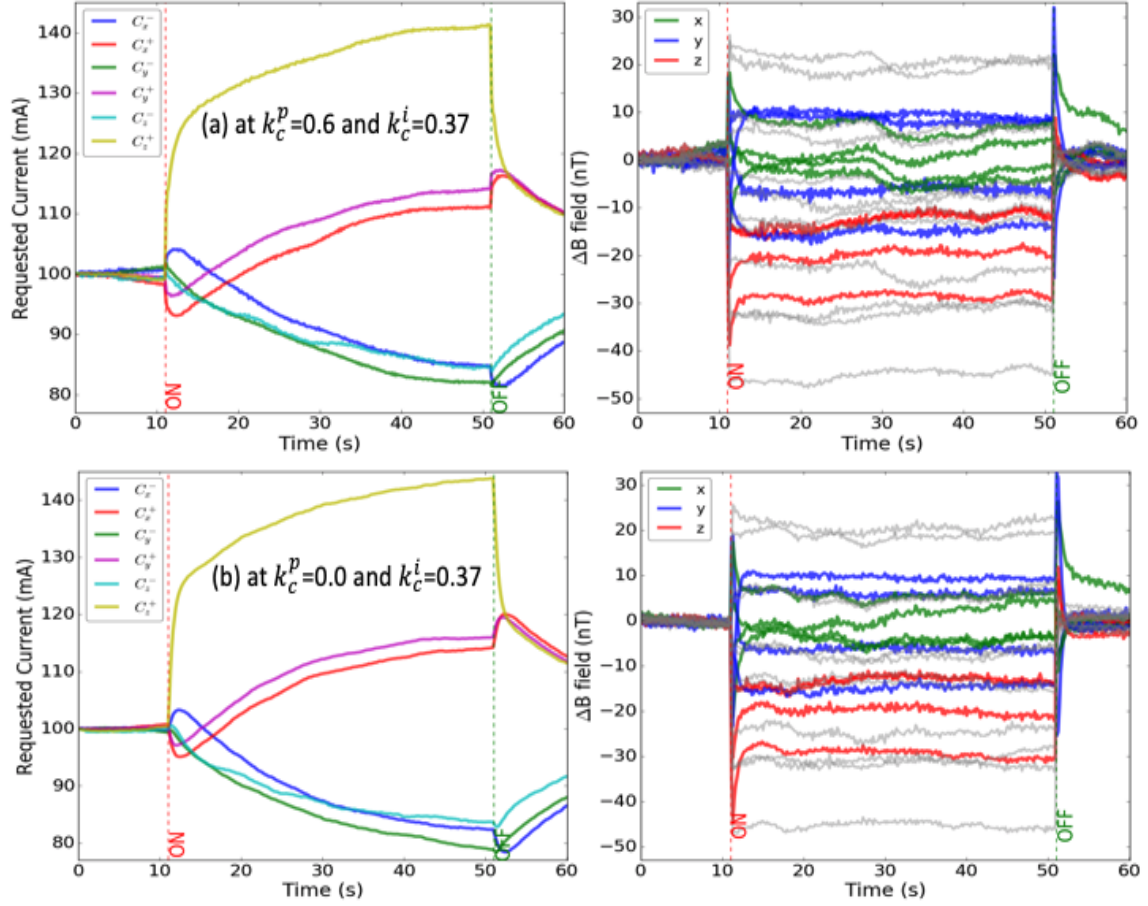


Figure 5.8: Currents (left) in all six coil sides with field measurements ΔB (right) from 12 sensor axes with fluxgate positions 1, 3, 6 and 8 for $k_c^i = 0.37$ and adjusting (a) $k_c^p = 0.6$ to (b) $k_c^p = 0$. Grey curves denote the uncompensated field change.

only I term pattern which is shown in Fig. 5.8(b) where only $k_c^i = 0.37$ is used.

The conclusion is that the P term has a smaller effect compared to the I term which is seen from comparing Fig. 5.5 with Fig. 5.7 and Fig. 5.8. It is also clear that the Ziegler-Nichols tuning does not necessarily give substantially different results compared to the $k_c^p = 0$ case. Figure 5.8(b), in comparison to the Ziegler-Nichols results in Fig. 5.8(a), looks better in some respects. The recovery time for the ΔB

is somewhat faster upon application of the perturbation coil current, and the general high-frequency noise on the ΔB is somewhat reduced. It should also be noted that there are some lower frequency bumps in the ΔB graphs in Fig. 5.8. These were caused by a somewhat unstable magnetic environment during the measurement and are not reflective of the tuning parameters.

Unfortunately, neither applying Ziegler-Nichols nor doing any additional tuning was able to change the current drifting problem. Although it does not appear when only the P term is nonzero, this was deemed undesirable because of proportional droop and the fact that the compensation results for the magnetic field were clearly better when using the I term or combined PI tuning.

5.2.4 The “Current Drifting Problem”

Because of the current drifting problem, we changed a large number of parameters in order to try to determine its cause. For example, one suspicion was that it could be due to malfunctioning power supplies that were themselves drifting, while the feedback loop was stabilizing. This was ruled out by careful tests of the power supplies, and by running the system with a reduced number of axes of control. For example, when only one axis of control was used, the system performed just like a usual PI loop with properly adjusted currents and fields. This is one reason the studies presented in Section 4.4 were done.

Section 5.3 represents other studies that were geared mostly at solving this problem. In these studies the positioning of the fluxgates were changed and the passive shield within the coils was removed. As will be shown, neither had an impact on the

current drifting problem.

In Section 5.4, simulation results are presented and compared with the data. It was at this point that we started to gain confidence that this was a true problem of multidimensional control, because, surprisingly the simulations agreed perfectly with the data and even reproduced the current drifting problem.

By studying the simulation results and the conditioning of the matrix (Section 5.5.2), we eventually determined that ill conditioning was the main problem. The next several sections all follow this theme of developing a better understanding of multidimensional control and ultimately showing that the simulation tools we developed are the best way to design the control system.

5.3 Fluxgate Placements and Impact of Passive Shield

An observation of the previous section was that the coil current does not settle properly although the field seems to be compensated on shorter timescales than the settling time for the currents. We called this the “current drifting problem” as noted in the previous Section. We developed hypotheses to try to explain this observation and then began to test these hypotheses experimentally.

The two hypotheses to explain the current drifting problem that are addressed in this Section are:

1. The fluxgate positions might be affecting the measurement. To address this, we adjusted the fluxgate positions to try to reduce the condition number and

see if this had a positive effect. We tried different positions mainly in corners and center of each of the coil faces, and at various distances inside and outside the coil cube. The conclusion of this study was that we could not change the condition number or the current drifting problem significantly.

2. The slow current response might be due to slow magnetic responses. To address this, we tried removing the magnetic shielding system from the coil cube and re-tuning the system. The conclusion of this study was that it also did not fix the problem.

In this Section, the results of these studies are shown and discussed. As will be shown in Section 5.7, the problem originates from having too many degrees of freedom in the coil system itself. Nonetheless these studies are important to show the process by which we learned this.

5.3.1 Fluxgate Placements

Previous work of others did not fully investigate the principles by which the fluxgate positions should be decided. The strategy of Ref. [69] was to place a larger number of fluxgates than required at conveniently mounted locations, distributed within the region of the coils and magnetic shield.

Based on this reference, we started taking data with 4×3 -axis fluxgate magnetometers placed just inside various corners of our coil cube. One hypothesis was that increasing the number of sensors would eliminate the problem of current drifting. To test this, we implemented additional fluxgate sensors and build an additional break-out box (see Section 3.4) so that we could acquire magnetic field data from them.

This still gave anomalously slow responses in the coil currents.

Another hypothesis was that placing the magnetometers at the center of each of the faces of the coils could improve the current response, or that more generally a broader range of positions should be tried. A general finding was that this also had not much effect on reducing the condition number significantly, nor did it have an effect on the current drifting problem.

The results for condition number are summarized for a representative subset of these tests in Table 5.1. Both the condition number of the matrix (equivalent to the condition number of the unregularized pseudoinverse) and the condition number of the regularized pseudoinverse are reported. Two very similar regularization parameters r and r' are reported. The regularization parameter r' was determined by a new method we developed which will be discussed further in Section 5.5.2.

The positions of the fluxgates are defined by the numbers for corner positions (see Fig. 3.3) and when they are in the center of each of the coil faces they are termed as Center (C_x^\pm , C_y^\pm , and C_z^\pm). Center-6cm means all the sensors in the center of the coil faces have been brought 6 cm towards the origin at the center and Center+6cm means they are 6 cm farther away from the center.

The matrix can be created for an arbitrary number of sensor positions by moving the sensors and recording field data for the various coil settings in subsequent runs. This has been done for example in the lowest row of the table where 14×3 -axis fluxgates have been incorporated into the matrix.

The general conclusion of Table 5.1 is that while the fluxgate positions have some impact on the condition number of both the unregularized and regularized pseudo-

Fluxgates Position	M Condition No.	M^{-1} Condition No.	r	r'
1, 3, 6 and 8	33.25	2.63	2.97	2.95
2, 4, 5 and 7	28.55	1.98	3.04	3.06
Center (C_x^\pm , C_y^\pm and C_z^\pm)	36.24	1.8	2.47	2.49
Center-6cm (C_x^\pm , C_y^\pm and C_z^\pm)	98.61	3.05	2.36	2.34
Center+6cm (C_x^\pm , C_y^\pm and C_z^\pm)	80.74	1.49	2.26	2.02
1, 2, 3, 4, 5, 6, 7 and 8	28.30	1.94	3.17	3.19
1, 2, 3, 4, 5, 6, 7, 8 and Center (C_x^\pm , C_y^\pm and C_z^\pm)	21.84	1.8	3.23	3.37

Table 5.1: Matrix properties for different numbers of fluxgate sensors at different positions. The nomenclature for the positions of the fluxgates is explained in Fig. 3.3. The column r represents the regularization method which is explained in Section 4.4.1 and r' represents the regularization method which will be explained in Section 5.5.2.

inverse, they do not solve the problem of ill-conditioning: the matrix must still be regularized or the current fluctuations driven by the compensation system would be unacceptably large. Even with significant changes in the fluxgate positions (for example corners vs. center faces) the condition number changes at most by a factor of three in the unregularized pseudo-inverse and a factor of < 2 for the regularized pseudo-inverse. Interestingly, even if a large number of sensors are included (*e.g.* the final two rows of the table), this does not necessarily have a positive impact on the condition number.

Another conclusion is that an over-constrained system (more fluxgate axes than coils) is not necessarily sufficient in order to have a well-conditioned problem. It is not even clear whether an over-constrained system is absolutely necessary to generate good control. For example, at the center face positions, the fluxgates only ever sense a large magnetic field in one particular direction, because the magnetic field must be perpendicular to the magnetic shield at this point. It effectively reduces the number of fluxgate axes to six, which is equal to the number of coils being used for control. And yet this gives an almost the same ill-conditioned properties for the matrix as any other row in the Table. We also tried studies where we used only those six axes in the control system, with very similar results to the corner-placement positions.

In Section 5.4, a simulation will be reported which is successful in reproducing these results. Although not shown here, the results of PI tuning of the systems for which we had enough sensors were also acquired. None of the positions gave particularly better PI control than any of the others and all of them generally suffered from the same current drifting problem.

We also tried slight adjustments to the corner positions and this had a similar small effect. It will be discussed further in Section 5.5.2 that it is also noticeable that regularization by two different methods (the method of Ref. [69] and our new method) agree.

5.3.2 Impact of Passive Shield

Fluxgate placements failed to solve the slow coil current response. Another hypothesis developed around this time was that increasing sampling frequency would solve the problem. So, besides the advantages discussed in Section 5.1, solving the slow current response time was also a motivation to build the filters as that would allow us to use the fastest sampling frequency of the ADC. As can be seen in that Section, using the filter, we successfully reduced the response time but still suffered from current drifts over long timescales.

Then we thought the passive shielding layer might have caused some slower response of the system, perhaps due to slow changes in the magnetization of the shield. To test if this affected the feedback and control system, we conducted tests where we removed the magnetic shield from within the coil cube.

Figure 5.9 compares the response of the system with the outermost magnetic shield layer inside the coil cube, to the response when no magnetic shields are present within the coil cube. When the shield is removed, it changes the matrix elements significantly. The matrix was therefore remeasured and the regularization process redone. It was possible to get satisfactory results for the inversion of both matrices (shield and no shield) using $r = 2.8$. Figure 5.9 demonstrates that removal of the

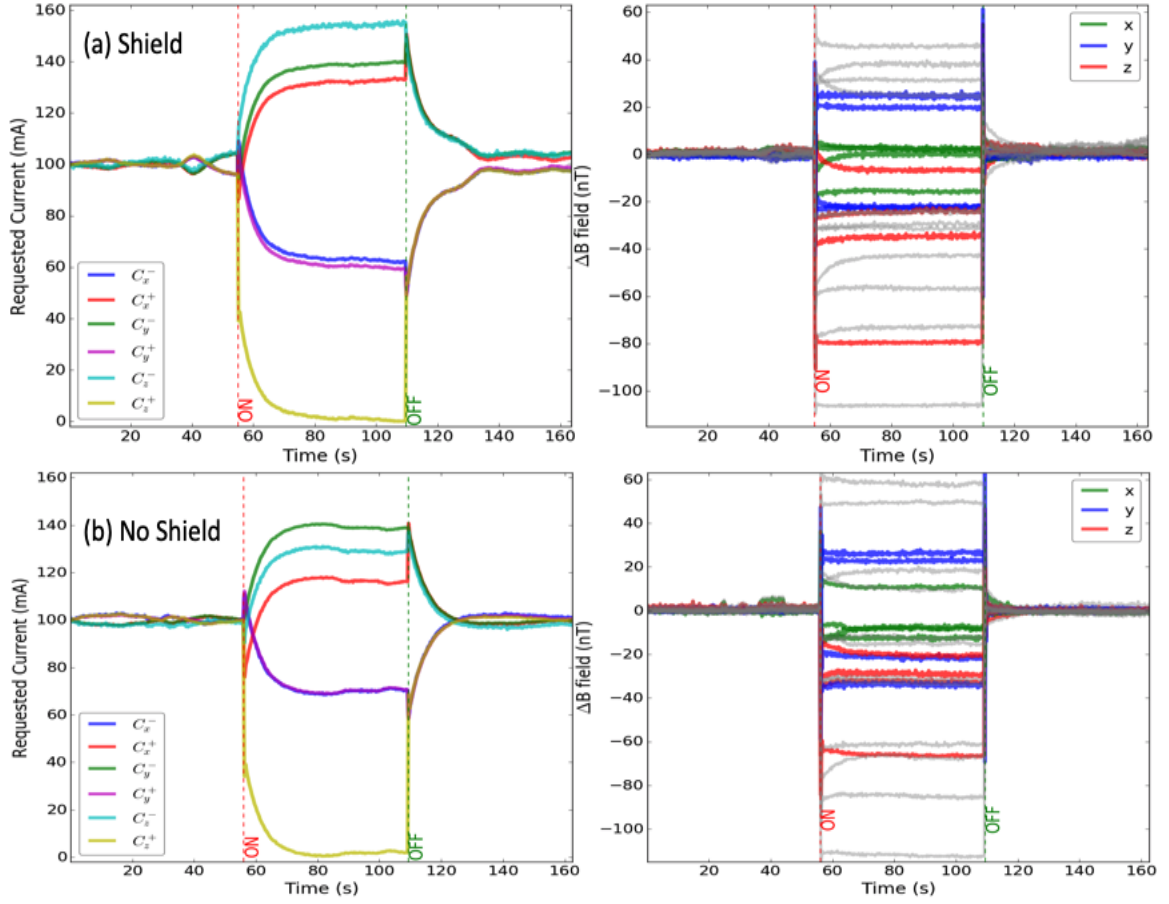


Figure 5.9: Magnetic compensation results (a) with shield and (b) without shield within the coil cube. The fluxgate positions are 1, 3, 6 and 8. The feedback and regularization parameters are $k_c^p = 0.0$, $k_c^i = 1.0$, and $r = 2.8$. The current supplied to the perturbation coil was 25 mA when switch on. Resolution index 1 with 50 averages per cycle were used.

magnetic shield, while having a significant impact on the matrix elements, does not have much impact on the effectiveness of the system to compensate the field. It also has no impact on the current drifting problem, although the pattern of currents has changed somewhat, because of the change in the matrix elements.

Another difference between Fig. 5.9 and Fig. 5.7 is that the connection of the coils to current sinks was changed, resulting in a change in the sign of some of the currents. These kinds of changes were also done often in order to try to address the current drifting problem and conduct tests of the current sinks.

In the end, neither fluxgate placement nor shielding effect provided a solution of the current drifting problem. How we really started to determine the source of the problem was by simulating the full, multidimensional feedback and control system.

5.4 Simulation of Multidimensional Feedback System

We developed a variety of simulation tools in order to understand the behavior of the multidimensional PI control loop:

1. **Three-dimensional finite-element analysis simulations in OPERA.** These were used to simulate
 - (a) the quasi-static magnetic response of the magnetic shield to Earth's field
 - (b) the magnetic response of the magnetic shield to changes in coil-cube currents (in turn enabling us to determine \mathbf{M}), and
 - (c) the magnetic response of the magnetic shield to the perturbation coil (in turn allowing us to simulate the PI system response to this perturbation.
2. **Field Map Processing in Python.** The OPERA simulations provided full three-dimensional field maps. Python scripts were written to process and sim-

plify the information into for example the matrix \mathbf{M} , or the changes seen at each fluxgate position when the perturbation coil was energized.

3. **PI Simulation in Python.** With this reduced information in hand, the full PI loop was also simulated in Python in real time. This allowed us to simulate the full time-dependent response of the feedback and control system to the perturbation coil.

As will be shown, these simulations were quite successful in describing the system including: the matrix \mathbf{M} and its inverse, and the time-dependent response of the PI loop to perturbation.

5.4.1 Simulation in OPERA to Generate Field Maps in Coil Cube

OPERA 3D Finite Element Analysis (FEA) [98] simulation software was used for simulating the prototype and generating field maps within the coil cube of the prototype. OPERA is a multi-physics software package. We have used the Opera Static Electromagnetics module which computes magnetostatic and electrostatic fields in three dimensions. The module solves Maxwell's equations for the static case in a discretized model using FEA. For calculating magnetic fields from coils, the module uses the Biot-Savart integral equation.

Geometry Definition in OPERA

Figure 5.10 shows the geometry as defined in OPERA, both with and without the magnetic shields. The dimensions of the prototype passive shielding layers and the

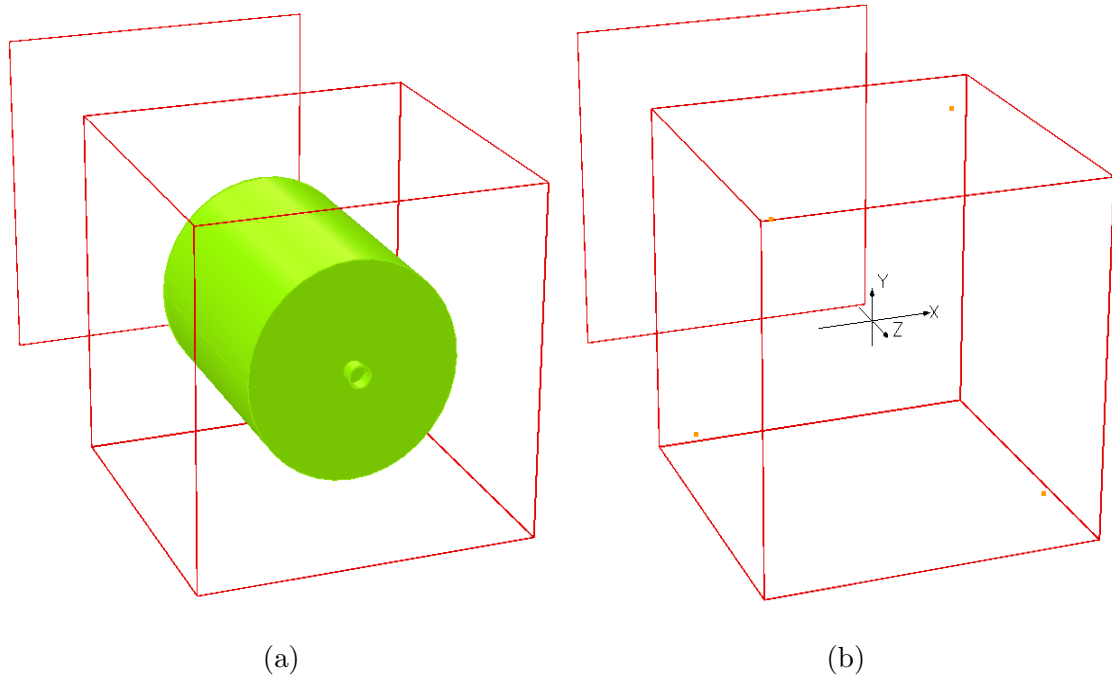
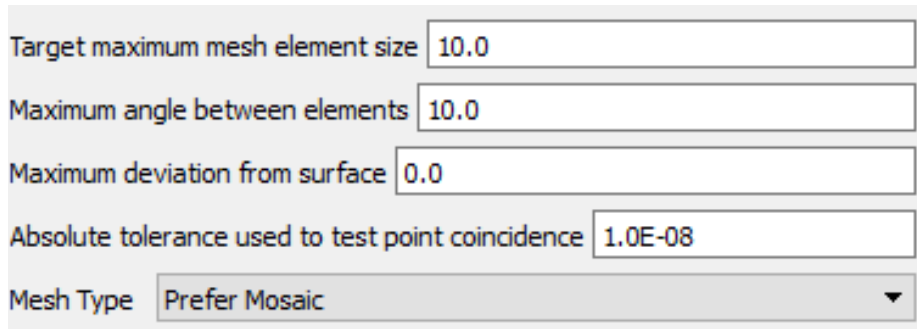


Figure 5.10: Geometry in OPERA simulation (a) with passive shielding, and (b) without passive shielding. The square in the back, appearing in both drawings, is the perturbation coil. The direction of each of the three axes may be seen in (b).

stove pipe were given in Table 3.1. These were implemented using simple cylindrical and planar shapes available in OPERA. The dimensions of the coils were given in Table 3.2. These were implemented as wires of square profile $1.24 \text{ m} \times 1.24 \text{ cm}$. The perturbation coil is 1.68 m away from the origin, which is at the center of the coil cube.

The material of the magnetic shield was chosen to be linear with relative magnetic permeability $\mu_r = 20,000$. Some air volumes were also drawn near the shields to aid in meshing near the thin layers. A cubic mother volume with side length 4 times the side length of the coil cube was used.

All the information has been written in the `comi` format file which is the command language in OPERA. Another `comi` file was made with no shield (Fig. 5.10(b)) for simulation of that experiment. The dots in Fig. 5.10(b) represent some fluxgate positions. But in general both simulations outputted full field maps so that the fluxgate positions could be adjusted arbitrarily after the simulation was complete.



The image shows a screenshot of the OPERA software's meshing settings window. It contains five input fields and one dropdown menu, all with a light gray background and a thin border. The settings are as follows:

Parameter	Value
Target maximum mesh element size	10.0
Maximum angle between elements	10.0
Maximum deviation from surface	0.0
Absolute tolerance used to test point coincidence	1.0E-08
Mesh Type	Prefer Mosaic

Figure 5.11: Settings to generate surface mesh in OPERA.

In OPERA, surfaces are first meshed, and then these meshes are extended into the volume with a subsequent volume meshing step. The settings used to generate the surface mesh are presented in Fig. 5.11, where a portion of the settings window is shown. To generate the volume mesh there is one additional setting which is another absolute tolerance; it was set to 1×10^{-8} .

Simulation Applying Current in Compensation Coils

In order to simulate the matrix \mathbf{M} we need to energize each coil in turn and measure the magnetic field change at each fluxgate position.

In OPERA, a coil was energized by setting its current density to 1 A/area, where the area is determined automatically by the OPERA based on the dimensions provided. To conduct the finite element analysis, the TOSCA magnetostatic module

of OPERA was used. The numerical solution convergence tolerance was set to be 1×10^{-13} .

A visualization of the magnetic field calculation in OPERA is shown in Fig. 5.12. In this example, the upper (C_y^-) coil has been energized. The magnitude of the magnetic field is seen to decrease as the distance from the energized coil increases. In this particular example, the passive magnetic shield was not present.

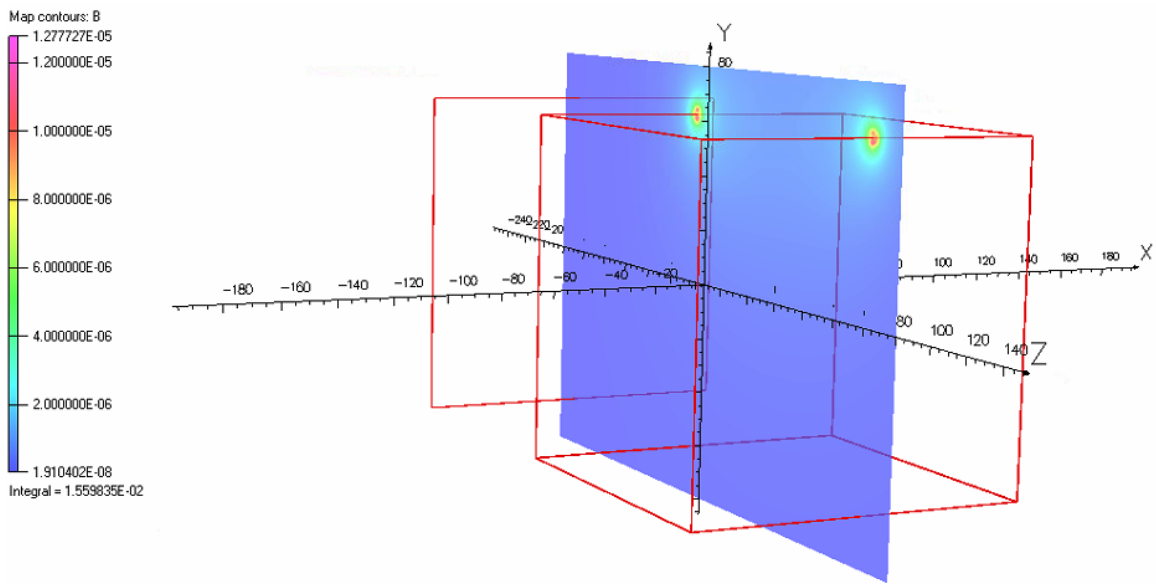


Figure 5.12: Map of the magnitude of the magnetic field in the yz -plane when the C_y^- coil is supplied with 1 A current.

Once the solution for a single energize coil was completed, the field map was outputted to a file using the post-processor of OPERA. The unit of the magnetic field was set to be T, and we used the GRID command which evaluates the fields over a uniform 3D grid. The grid started from -62 cm in x , y and z coordinates with an increment of 1 cm and ends at $+62$ cm which covers the full cube dimensions. The output of the GRID command gives a text (csv) file with 6 columns, where the first

3 columns indicate the coordinates of the grid point (x,y,z) and the last 3 columns indicate the magnetic field (B_x,B_y,B_z) at that point. In this way 6 field maps are stored in 6 csv files, one for each of the 6 coils.

The Effect of Earth's Field and of the Perturbation Coil

The field maps of the previous section were calculated in the absence of Earth's field. In general, the fluxgate setpoints were decided by first measuring the field and then selecting the setpoint based on that measurement. The feedback system would then try to lock the fields to those setpoints.

The average field measured by fluxgates surrounding the prototype without any compensation system running were given in Table 4.2. This information was used to try to simulate the setpoints. This was done for two field maps: one with no current in any coils and another with current only in the perturbation coil. So, the field map with no current in any coil will generate the setpoint i.e. $B_s(\text{setpoint})$ and the field map with current in perturbation coil will generate the actual measurement i.e. $B_s(\text{measure})$. The difference between $B_s(\text{measure})$ and $B_s(\text{setpoint})$ will generate the change in field ΔB .

The six field maps generated by the coil-cube simulation of the previous section can be added to these maps without loss of generality under the assumption of linear material properties.

We used the same meshing as described earlier. The perturbation coil was energized, or left unenergized, in a similar fashion as used for the coil-cube. The main difference compared to the previous coil-cube simulation was that the external mag-

netic field \mathbf{H} on TOSCA analysis module was set according to Table 4.2. Otherwise the field was solved and outputted to a `csv` file as in the previous section. Two `csv` files (one each for the perturbation coil switched on and off) were created.

When the perturbation coil was switched on, its current density was set to 770 mA/area. The reason is that, in the experiment, 10 mA current was normally provided to the perturbation coil which has 77 turns.

5.4.2 Field Map Processing in Python

A set of Python codes are used to generate files containing the matrix \mathbf{M} and ΔB perturbations from the OPERA field maps. The codes accept as input the field maps and the coordinates for the fluxgate positions, and then output the relevant field values from OPERA.

For comparison with the experimental \mathbf{M} , the simulation \mathbf{M} has been made by choosing coordinates of the points as same as the sensor positions in the experiment. Then the absolute differences between the experimental and simulated matrix elements are calculated as

$$\Delta|M_{sc}| = |M_{sc}^{\text{exp}}| - |M_{sc}^{\text{sim}}| \quad (5.1)$$

where, $|M_{sc}^{\text{exp}}|$ and $|M_{sc}^{\text{sim}}|$ indicate the absolute values of the M_{sc} elements both in experiment and simulation respectively. The absolute value is taken to avoid any potential sign errors in the coil directions in experiment compared to simulation.

The resultant differences $\Delta|M_{sc}|$ are presented in Fig. 5.13. These can be compared with the experimental values which were presented in Fig. 4.1.

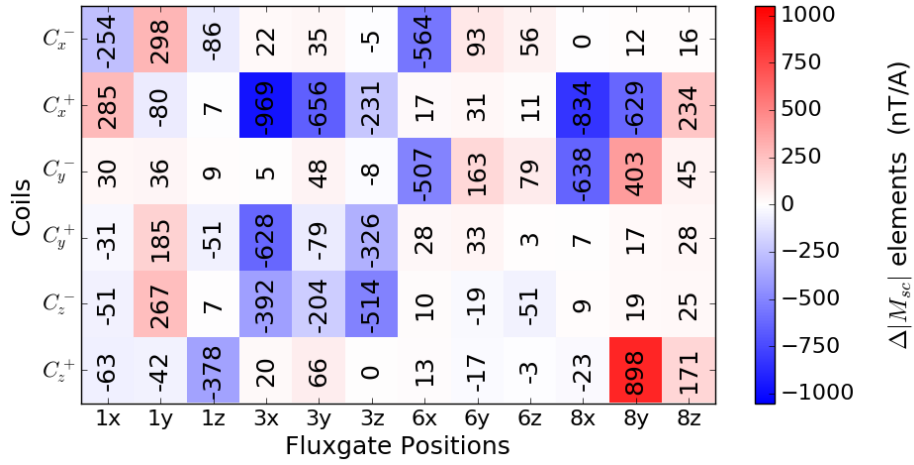


Figure 5.13: Differences between absolute experimental and simulated matrix elements $\Delta|M_{sc}|$ (defined in the text). Horizontal axis indicates the various sensors, which are counted using the index s . Vertical axis indicates the various coils, which are counted using the index c .

In general, the simulated values are somewhat larger than the experimental values resulting in Fig. 5.13 having more blue than red numbers. This is particularly true of fluxgate sensor position 3 (3x, 3y, and 3z). The largest difference seen is in the 3x sensor in its response to the C_x^+ coil. On average, the matrix elements agree within about 30% with the matrix elements in Fig. 4.1, as can be seen from the change in the color scales on the figures. The mean of the absolute values of the entries in Fig. 5.13 is found to be 168 nT/A, and the root mean square of the values is found to be 291 nT/A. These are indications of the average absolute deviation of the simulation from the experimental values.

We expect that most of the differences can be attributed to discrepancies in the sensor placements between the experiment and simulation. Experimentally, the value

of the field measured and its slope with current are very sensitive to location in this region between the coils and the shield. For example, the field near the surface of the magnetic shield can be enhanced by a factor of 2 to 3 over the general background field far from the shield.

Interestingly, the condition number of the two matrices are very similar. The experimental \mathbf{M} has a condition number of 29.6 and the simulated one is 30.5. Recall that the condition number is the ratio of the maximum and minimum singular values. This likely indicates that ratios of the important matrix elements are reproduced better than the absolute difference would indicate. The singular value decomposition also tends to correct sensor misalignment. In other simulations, we found that moving sensors slightly or changing their alignment had little to no effect on the condition number, even though the matrix elements might change.

In another experimental study, the stability of the matrix elements was measured over an eight-hour period, continually ramping the currents on each coil and measuring the slope over and over again. We found that the measured matrix elements were reproducible at the level of 100 nT/A. We also discovered a technical issue that the C_x^- coil current had stability issues, which turned out to be due a bad connection, which was repaired.

Of course, the effect of the perturbation coil on the fluxgate signals was also compared between experiment and simulation. We discuss these results further in the case of the PI system operating, in the next section.

5.4.3 PI Simulation in Python

The matrix \mathbf{M} and perturbation coil ΔB simulations can now be implemented into a dynamic PI simulation. The ΔB perturbation can be turned on at a particular time. Errors in the coil currents (Eq. (4.3)) are generated using ΔB and the regularized pseudoinverse of the simulated \mathbf{M} . The same values of k_c^p and k_c^i are used in the simulation as in the experiment.

We decided to simulate the PI loop in real-time. In Section 4.5, the time difference between two consecutive feedback loop is found to be 0.146 s. To match the same time of completing a feedback loop both in simulation and experiment, we added a time delay of 0.146 s in the PI simulation code. After adding the time delay, The same process have been repeated for the same time duration as the experiment.

The comparison of the experimental and simulated PI loops is shown in Fig. 5.14. It is seen that the coil current responses and field changes have similar pattern in the simulation, when compared to the experiment.

The most amazing aspect of the graph is that the current drifting problem is reproduced. The currents drift for long periods of time, whereas the field corrections appear to occur on a much more rapid timescale.

Seeing this anomalous effect reproduced so accurately in the multidimensional PI gave us confidence that it is a real effect which is somehow due to the algorithm that we were following. This led to additional simulations and the discovery of new ways to deal with the current drifting problem, without making large changes to the apparatus.

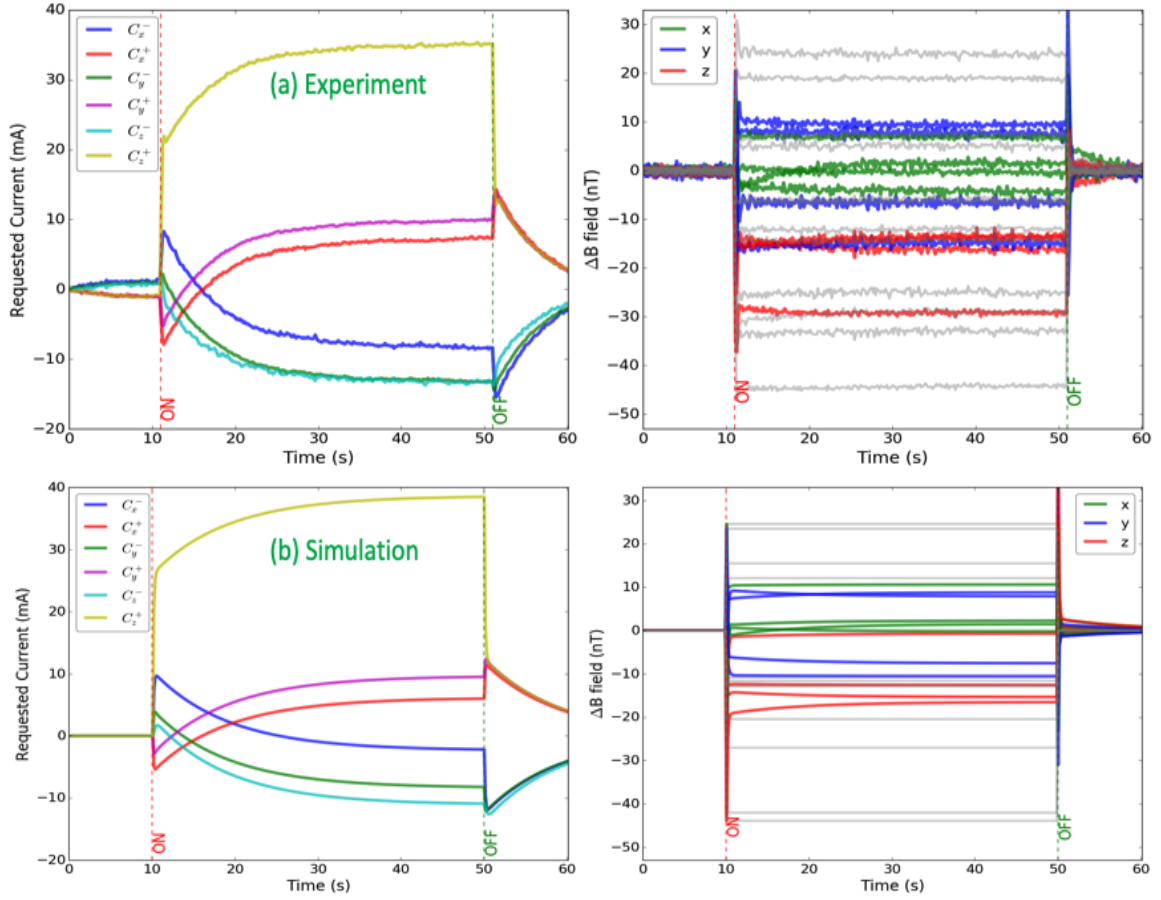


Figure 5.14: Magnetic field compensation results in (a) experiment and (b) simulation. The fluxgate positions are 1, 3, 6 and 8. The feedback and regularization parameters are $k_c^p = 0.0$, $k_c^i = 1.0$, and $r = 3.1$. The current supplied to the perturbation coil was 10 mA when switched on. Resolution index 1 with 50 averages per cycle were used.

5.5 Studies on the Regularization Parameter r

In Section 4.4, the regularization parameter r was introduced and then regularization by random field fluctuations was discussed in Section 4.4.1 which is based on the previous study from Ref. [69].

These studies were expanded in relation to the current drifting problem. We

found that the current drifting problem can be reduced by adjusting r and the PI parameters, treating r more-or-less as another free parameter. But this is generally at the expense of also introducing higher-frequency noise.

Finally, a new method of determining the regularization parameter is proposed which is unique compared to the Monte Carlo method introduced in Section 4.4.1 and used in Ref. [69]. The method is based on minimizing the condition number of the regularized matrix, which gives similar results as the Monte Carlo method. The correspondence between the two methods will be discussed in the following sections.

5.5.1 Effect of r on PI Tuning

The discussion on Section 5.2 suggests that the k_c^i term in the PI feedback algorithm is necessary for fast system response, and to reduce proportional droop and hence the error signals. But, in including this term, we found that it also creates problems in terms of the coil currents which take long periods of time to settle (several tens of seconds). We called this problem the current drifting problem. Adjusting the PI feedback parameters changed the problem somewhat but ultimately did not reduce the current drifting time. Here, we focus on the effect of r on this problem, treating it on a more equal footing with the PI parameters.

Figure 5.15 shows an example of the impact of changing k_c^i when k_c^p is held fixed and the regularization parameter r is set to its best value. Only the current in one coil and the field measured in one fluxgate axis are shown so that the impact of changing k_c^i can be observed.

It is seen that there is no current drifting problem if $k_c^i = 0.0$ is used, but that

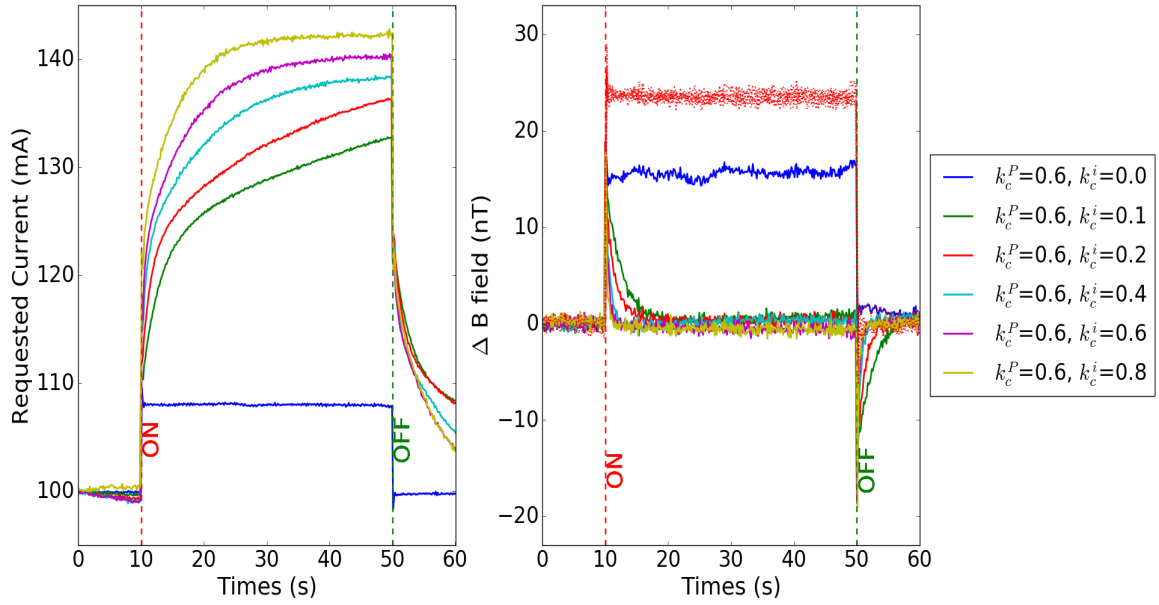


Figure 5.15: The C_z^+ coil current (left) and magnetic field change ΔB for sensor 8x (right) with $k_c^p = 0.6$, $r = 3.04$ and different values of k_c^i . In each case, resolution index 1 with 50 software averages per cycle were used. Vertical dashed lines indicate the perturbation coil state.

the field error is consequently larger. If $k_c^i = 0.8$ is used, the field is corrected in a few seconds to a smaller error, but the current drifts for considerably longer, about 10-20 seconds. This is similar to the observations described in Section 5.2. We have also seen the effect in Section 5.2 that increasing k_c^i after a point makes the current unstable resulting in overshoot.

For these studies, we focused on the C_z^+ coil and the 8x sensor because they are located closer to the perturbation coil and hence see the effect most.

We then tried changing r while keeping k_c^i and k_c^p terms fixed. Figure 5.16 shows the active compensation for same fluxgate positions and same settings as in Fig. 5.15,

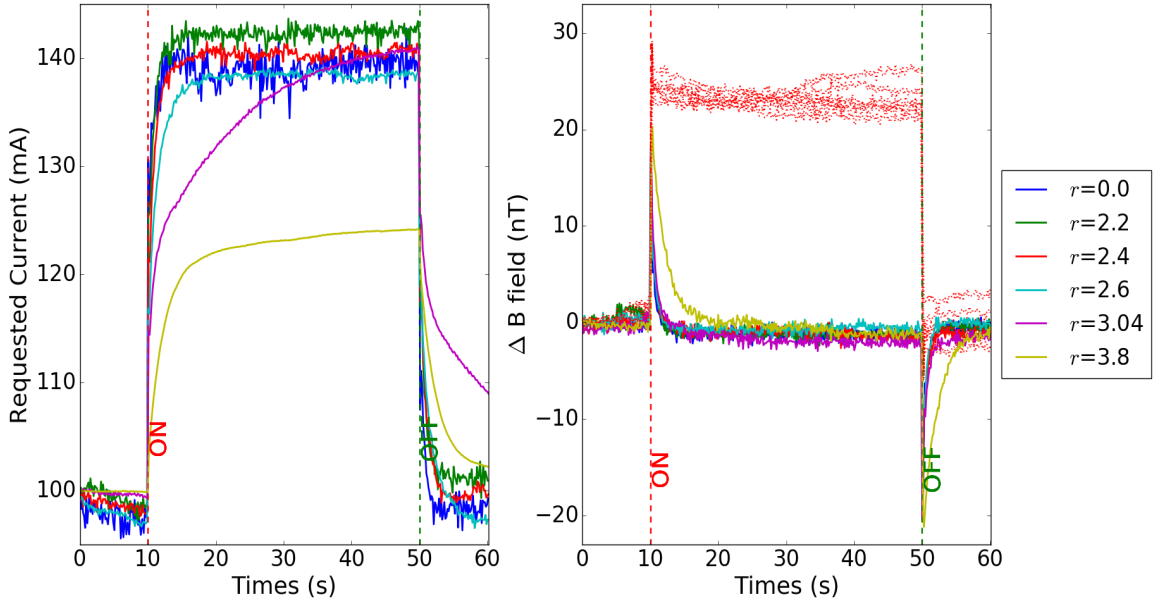


Figure 5.16: The C_z^+ coil current (left) and magnetic field change ΔB (right) for sensor 8x with $k_c^p = 0.6$, $k_c^i = 0.37$ and different values of r . In each case, resolution index 1 with 50 software averages per cycle were used. Vertical dashed lines indicate the perturbation coil state.

with $k_c^i = 0.37$, and this time for different values of r . The observation is that for decreasing r , the current drifting problem disappears, but the feedback system introduces high frequency noise (the spiky behavior in the currents, which is also seen at a somewhat reduced level in the ΔB).

It is natural that r should affect the PI control, because the error function involves M^{-1} and therefore r (see for example Eqs. (4.3), (4.4), and (4.10)). If r is larger then M^{-1} generally gets small. So, it would be reasonable to expect that if r increases then we need to increase both k_c^p and k_c^i accordingly (see Eq. (4.4)).

Therefore best that can be done to fix the current drifting problem is that r , k_c^p ,

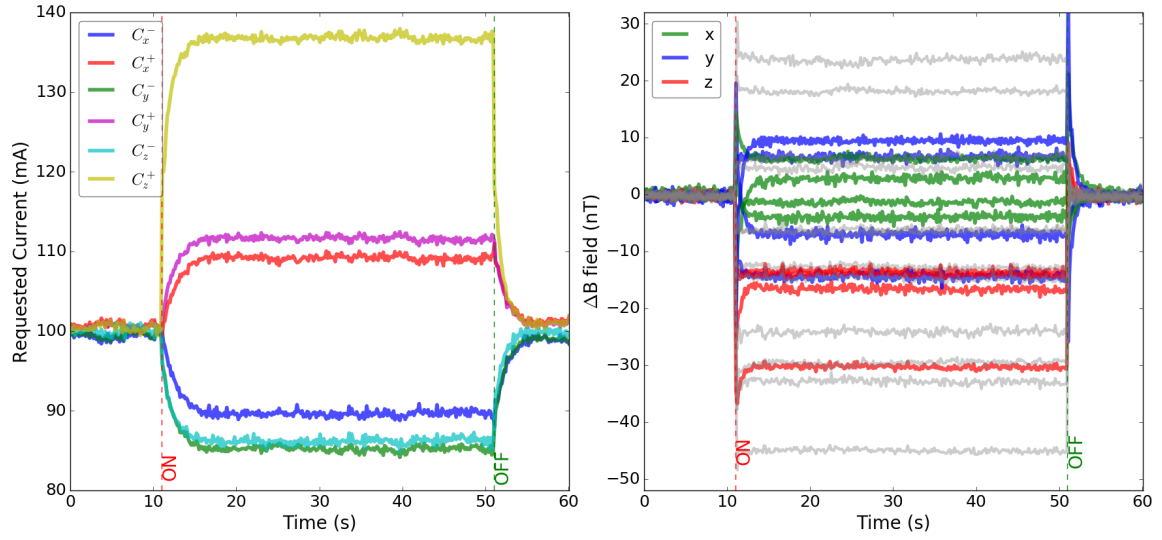


Figure 5.17: Currents (left) in all six coils (C_x^\pm , C_y^\pm and C_z^\pm) and field change ΔB (right). The fluxgate positions are 1, 3, 6 and 8. The feedback and regularization parameters are $k_c^p = 0.6$, $k_c^i = 0.37$, and $r = 2.4$. The current supplied to the perturbation coil was 10 mA when switch on. Resolution index 1 with 50 averages per cycle were used.

and k_c^i be adjusted to reduce the current drifting problem without too much impact on high-frequency noise. An example of an attempt to make this trade-off is shown in in Fig. 5.17. Other than changing r to 2.4, this Figure uses the same settings as Fig. 5.8(a). Indeed reducing r has increased the speed with which the currents settle, but apparently increased high-frequency noise on the currents. However, this increase in current noise does not increase the noise on the field measurements noticeably, which is similar in both cases. In Fig. 5.18, we have retained this value of $r = 2.4$ and adjusted the PI parameters to attempt to further improve the response time on the currents.

Eventually, it was discovered that neither of these solutions was truly optimal.

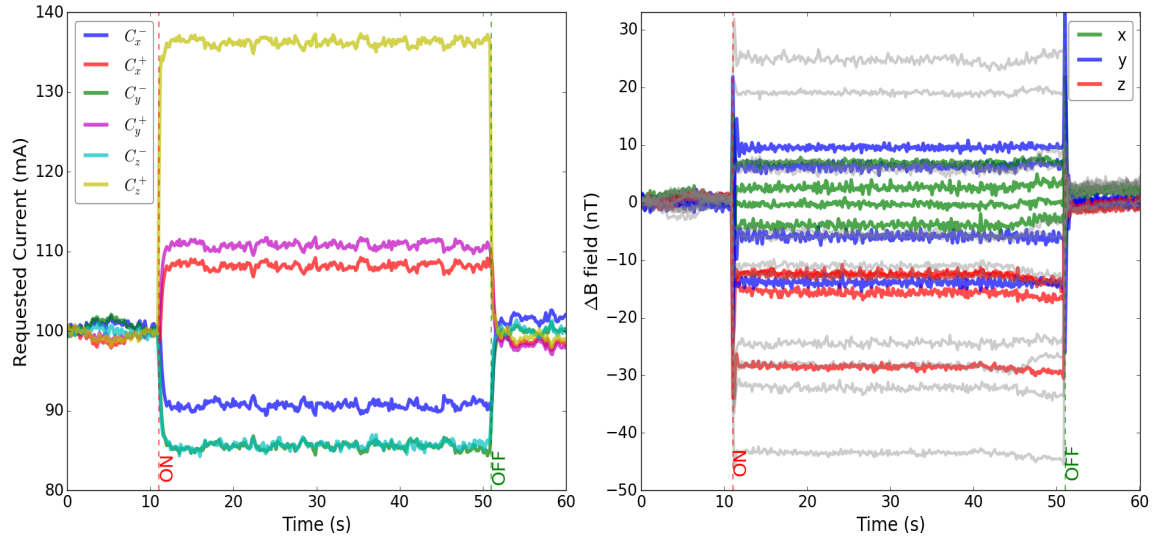


Figure 5.18: Currents (left) in all six coils (C_x^\pm , C_y^\pm and C_z^\pm) and field change ΔB (right). The fluxgate positions are 1, 3, 6 and 8. The feedback and regularization parameters are $k_c^p = 0.0$, $k_c^i = 1.0$, and $r = 2.4$. The current supplied to the perturbation coil was 10 mA when switch on. Resolution index 1 with 50 averages per cycle were used.

We now characterize them as being generally ill-conditioned. The final solution is discussed further in Section 5.7.

The above results show that if r (or the condition number) is bad (too big) then no amount of PI tuning will help speed up the current drifting. If r is set too small, it is expected to have an undesirable impact on the PI parameters. While this might be acceptable in some situations, such as a case where the field noise is already rather large, it is not the best general solution.

5.5.2 Regularization by Matrix Condition Number Method

The condition number of \mathbf{M} and its regularized pseudo-inverse, and the regularization parameter r were introduced in Section. 4.2 while discussing the inversion of the matrix \mathbf{M} . Moreover, in Section 4.4.1, the method of Ref. [69] of selecting the best value for r by randomly generated field perturbations was discussed. The purpose of this section is to report that this method of selecting r is equivalent to minimizing the condition number of the regularized pseudo-inverse \mathbf{M}^{-1} .

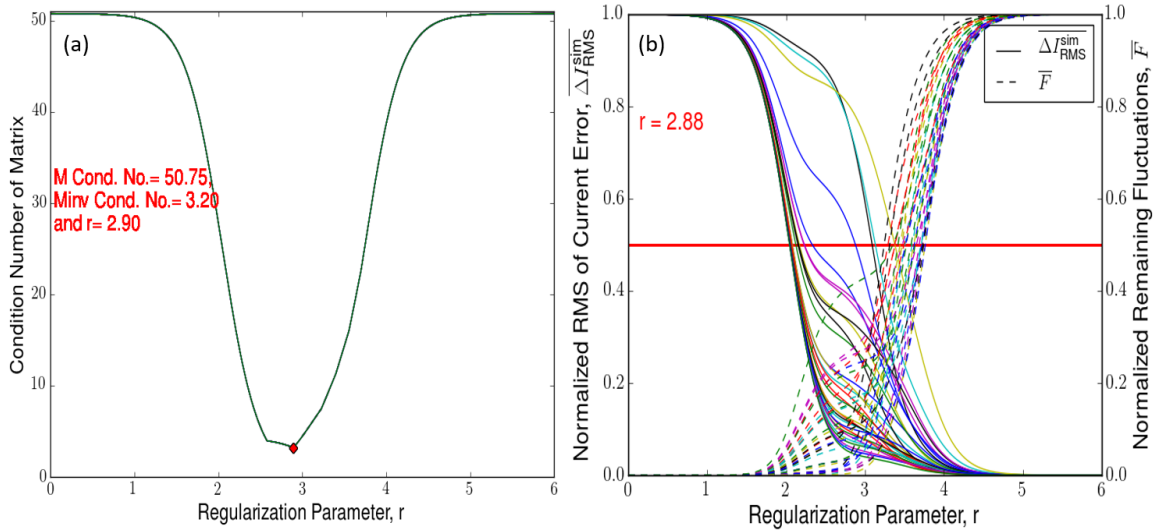


Figure 5.19: (a) Condition number of \mathbf{M}^{-1} vs. r , and (b) determination of r using random field fluctuations. For a more complete description of (b) see Fig. 4.6.

The condition number of \mathbf{M}^{-1} for different values of r is presented in Fig. 5.19(a) and exhibits a clear minimum at $r = 2.90$ (indicated by the red diamond in the Figure). It is seen that for $r = 0$, the condition number of $\mathbf{M}^{-1} \approx 51$ which is by definition the same as the condition number of \mathbf{M} itself. The minimum value of the condition number is 3.2 which is a factor of 17 reduction. Recall that the ideal value

of the condition number is unity.

Figure 5.19(b) shows the same matrix being analyzed using the random field fluctuation method of Section 4.4.1 and Ref. [69], where current fluctuations are traded off against field control. In this study, the “best” value $r = 2.88$ is determined, which can be compared to $r = 2.90$ which minimizes the condition number of the regularized pseudoinverse.

We tried this same comparison for a variety of different \mathbf{M} and always found the same level of agreement in the determination of r . A sample of results was shown in Table 5.1. We think that the method of minimizing the condition number is more robust because it does not involve random number generation and therefore is free of any additional statistical error.

We suspect the excellent agreement seen between the two methods results from the definition of Tikhonov regularization [85, 87–89].

Given a vector of field fluctuations $\Delta\vec{B}$ and a vector of correction currents $\Delta\vec{I}$, the Moore-Penrose pseudo-inverse \mathbf{M}^{-1} can be thought of as the matrix which minimizes $|\Delta\vec{I} - \mathbf{M}^{-1}\Delta\vec{B}|$, which is analogous to chi-squared minimization for a system of linear equations. Tikhonov regularization is used when this problem becomes ill-conditioned, and introduces another constraint that simultaneously minimized the modulus of the vector $|\Delta\vec{I}|$. In a way this is equivalent to the compromise being made in the selection of the “best” r using the random field fluctuation method. Current and field fluctuations are being traded off against one another in order to prevent large current fluctuations from occurring.

We think, it is therefore not surprising that the two methods give good agree-

ment. We feel the minimization of condition number is a better defined solution, not requiring random number generation, and that it is a superior and robust method to determine r .

5.6 “New” feedback algorithm vs. standard PI control

In Sections 4.5 and 5.2, the PI feedback algorithm and the studies of tuning both the PI parameters and the regularization parameter r were discussed. The studies were all based on the work of Ref. [69].

Subsequently, Refs. [71, 99, 100] made the claim that there is no need to use the standard PI feedback algorithm. This led to a number of studies using the “new” feedback algorithm, which indeed seemed to give similar results when compared to the “old” feedback algorithm.

Eventually, we determined this is due to the fact that they are mathematically equivalent under certain conditions which correspond closely to the typical operating conditions of my active magnetic compensation apparatus.

The basis of the “new” feedback algorithm is presented in Ref. [71] as providing an updated version of current \vec{I}^{n+1} which is based on the current determined by the previous step \vec{I}^n . The equation to be used to find the next current in the new algorithm is

$$\vec{I}^{n+1} = \vec{I}^n + \mathbf{M}^{-1}(\vec{B}_{\text{setpoint}} - \vec{B}_{\text{measure}}^n) = \vec{I}^n + \mathbf{M}^{-1}\Delta\vec{B}^n \quad (5.2)$$

which is taken directly from Eq. (28) in Section 5.5 of Ref. [71]. In this equation,

$\Delta\vec{B}^n$ is a vector of magnetic field values measured in the given feedback step. The dimension is equal to the number of fluxgate axes being used for control (12 in our case). The quantity \mathbf{M}^{-1} is the Moore-Penrose pseudo-inverse (a 6×12 non-square matrix, in our case). The quantity \vec{I}^n are a vector of currents (dimension 6, in our case). The index n refers to the present feedback step. The index $n + 1$ on the left-hand-side of the equation is indicating the next vector of currents that will be set based on this feedback algorithm.

This algorithm can be compared with the standard PI algorithm, which were presented in Eqs. (4.3), and (4.4). Naively, the main difference between the two equations appeared to be that the current from the previous step was being used to determine the next current with the error from the present step also being included. Eq. (4.4) on the other hand, refers to the next current to the initial current, and implements two control terms: a proportional term which appears similar to the error term containing \mathbf{M}^{-1} above, and an integral term containing an sum over the past history of errors.

The new feedback algorithm was implemented into our code to test it. Experimentally, it was discovered that the new algorithm gave very similar results to the standard PI algorithm if we set $k_c^p = 0$ and used $k_c^i = 1.0$. The results of such a test are shown in Fig. 5.20, where the two algorithms are compared in both their current and field response, and give suspiciously similar results.

In the case of $k_c^p = 0$ and $k_c^i = 1$, the PI feedback algorithm in Eq. (4.4) can be written as

$$\vec{I}^{n+1} = \vec{I}^0 + \sum_{i=0}^n \mathbf{M}^{-1} \Delta\vec{B}^i, \quad (5.3)$$

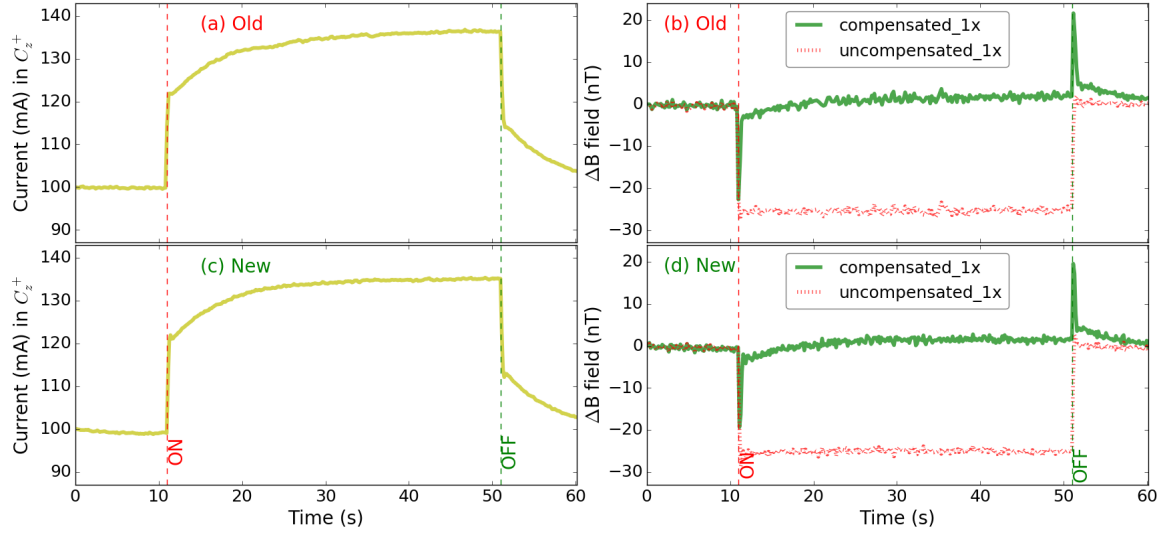


Figure 5.20: “Old” ((a) and (b)) and “new” ((c) and (d)) feedback algorithms compared. Panels (a) and (c) compare the currents in coil C_z^+ , and (b) and (d) the field change ΔB for sensor position 1x. The feedback parameters used for the “old” PI algorithm $k_c^p = 0.0$, $k_c^i = 1.0$. The current supplied to the perturbation coil was 10 mA when switched on. Resolution index 1 with 50 averages per cycle were used.

where the same matrix and vector notation is being used as in Eq. (5.2).

Studying Eqs. (5.2) and (5.3) further, we were able to prove that the similar results actually arise because the two implementations are mathematically equivalent.

Suppose that Eq. (5.3) is true. It will also have been true for the previous step $n \rightarrow n - 1$

$$\vec{I}^n = \vec{I}^0 + \sum_{i=0}^{n-1} \mathbf{M}^{-1} \Delta \vec{B}^i. \quad (5.4)$$

Eq. (5.3) can then be rewritten by removing the final term from its sum, then applying

Eq. (5.4):

$$\begin{aligned}
 \vec{I}^{n+1} &= \vec{I}^0 + \sum_{i=0}^n \mathbf{M}^{-1} \Delta \vec{B}^i \\
 &= \vec{I}^0 + \sum_{i=0}^{n-1} \mathbf{M}^{-1} \Delta \vec{B}^i + \mathbf{M}^{-1} \Delta \vec{B}^n \\
 &= \vec{I}^n + \mathbf{M}^{-1} \Delta \vec{B}^n,
 \end{aligned} \tag{5.5}$$

which is just Eq. (5.2). This was further confirmed by implementing both algorithms in the PI simulation of Section 5.4. In this case, the algorithms indeed gave identical results since there is no experimental noise in the simulation.

Hence, we conclude that the “new” feedback algorithm of Ref. [71] is simply the usual PI feedback algorithm, with the PI parameters being restricted to the particular values $k_c^p = 0$ and $k_c^i = 1$. The recommendation would be to keep these as tunable parameters and allow for the potential of some ability to make adjustments to them as necessary, rather than restricting them to particular values. It is interesting that the particular tuning $k_c^p = 0$ and $k_c^i = 1$ (integral control) does seem to be fairly optimal for this particular system.

Reference [71] further mentions that due to time delays in their active magnetic compensation system, it was logically more correct to use the current from three steps prior to making the correction for the $n + 1$ step

$$\vec{I}^{n+1} = \vec{I}^{n-2} + \mathbf{M}^{-1} \Delta \vec{B}^{n-2} \tag{5.6}$$

(which is Eq. (30) in Section 5.5 of Ref. [71]). This could also be considered as another form of PI tuning where the past history of the system is weighted differently.

5.7 Coil Configuration

In light of the previous studies, there was now strong evidence to suggest that the current drifting problem had more to do with the structure of the non-square matrix than with other possible problems such as instability of the current sinks or issues with the PI feedback loop. In consideration of this, we began to focus more on understanding the matrix, its pseudo-inverse, and the concepts of matrix regularization.

In order to study a broader range of possible coil geometries, another Python code was written which could perform magnetic field calculations for rectangular coils wound in the free space. Since, it would not rely on OPERA simulations, the process of generating matrices then became much faster. Studying such a case was also a reasonable step, since the current drifting problem had been shown experimentally not to depend on whether the magnetic shields were present within the coil cube.

The code generated coil geometries that were highly idealized. They were like the coil cube displayed in Fig. 3.3, but with the currents exactly on top of one another. Fluxgate positions were again generally placed in the corners of a slightly smaller cube, or could alternately be placed in the middles of the faces of cube, much like the studies presented in Table 5.1.

Figure 5.21 shows an example of a matrix \mathbf{M} generated by the code. The magnetic fields generated by the code were cross-checked in multiple ways, since the code uses only one formula for the field due to a straight line segment of current.

The interesting result of the code was that it would always give infinity for the condition number of the matrix \mathbf{M} when six coils were used, no matter what positions for the fluxgates were used nor the number of fluxgate axes used. An example of one

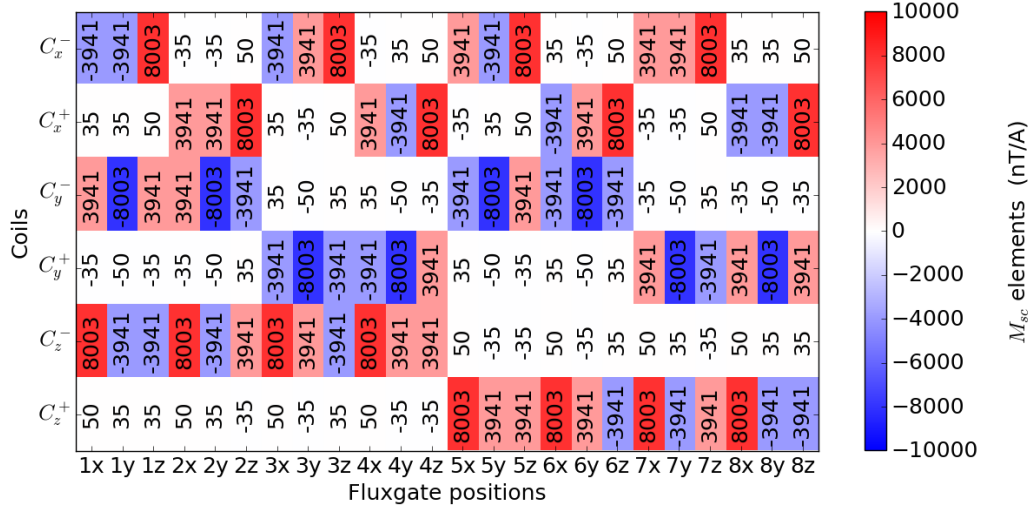


Figure 5.21: Color map of M_{sc} elements for 24 fluxgate axes and 6 coils. In the simulation, the six coils are wound on the edges of the six faces of a cube of side-length 1.24 m, and the fluxgates are placed in the eight corners of a smaller cube of side-length 1.20 m.

such simulation is shown in Fig. 5.22 where the Σ matrix involved in singular value decomposition of the matrix \mathbf{M} is displayed (see Section 4.4 for the description of the process of singular value decomposition). The matrix Σ is a diagonal matrix whose elements are the positive square roots of the singular values of $\mathbf{M}^T \mathbf{M}$, sorted from largest to smallest.

The condition number is the ratio of the largest Σ_{11} component of the Σ_{nn} where $n = 6$ is limited by the number of coils. The key problem with the matrix Σ was that the Σ_{nn} matrix element was always zero. Changing the geometry (coils or fluxgates) would alter the other singular values, but would never make the smallest singular value larger than zero.

We then tried to understand the reason for the minimum diagonal element being

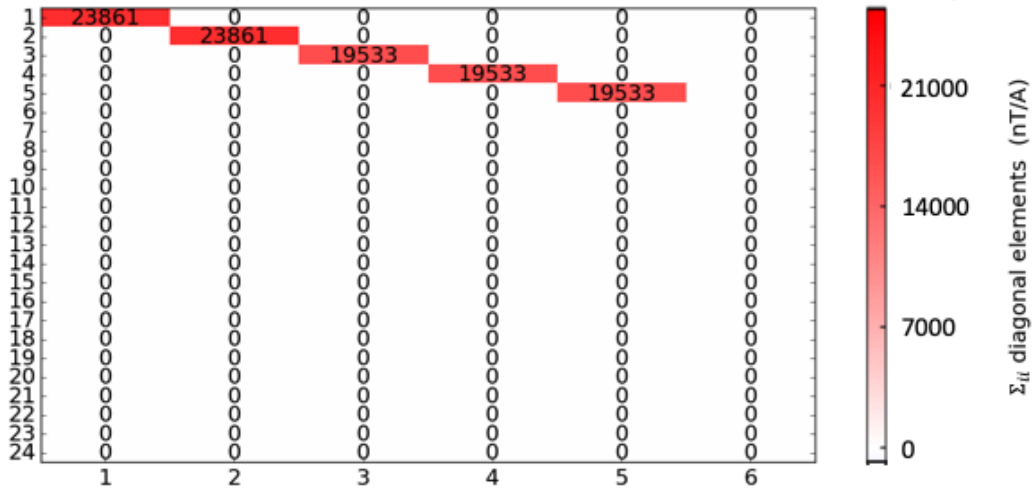


Figure 5.22: Color map of diagonal matrix Σ found by SVD of simulated M for 24 fluxgate axes and 6 coils. Coil dimensions and fluxgate positions are given in Fig. 5.21.

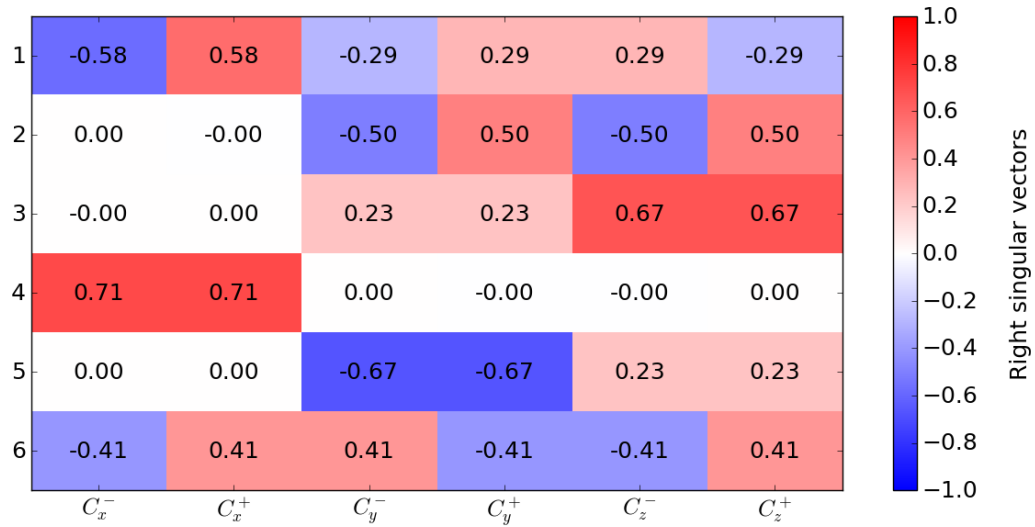


Figure 5.23: Color map of orthogonal matrix V^T found by SVD of M for 24 fluxgate axes and 6 coils. Coil dimensions and fluxgate positions are given in Fig. 5.21.

zero, by studying the right singular vectors, which are represented by the rows of \mathbf{V}^T . This matrix is displayed in Fig. 5.23.

The singular values may be analogized to eigenvalues seen in the case of square matrices. The diagonal matrix represented by the eigenvalues express the same matrix, where an orthogonal similarity transformation to the eigenbasis has been performed. The rows of the orthogonal transformation are the eigenvectors corresponding to each eigenvalue. Likewise the right and left singular vectors for a non-square matrix appears in the rows or columns of the square \mathbf{V}^T and \mathbf{U} , respectively.

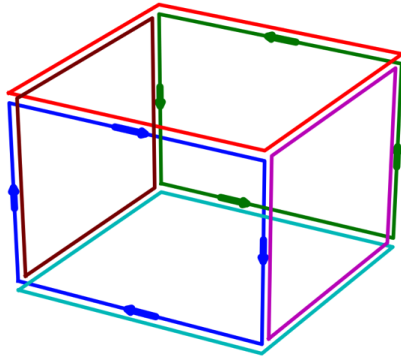
The matrix \mathbf{V}^T corresponds to the right-singular vectors, which in turn correspond to the coil basis. It is a square, orthogonal matrix. As presented in Fig. 5.23, each row corresponds to a singular vector. Row 1 corresponds to the singular value Σ_{11} and row 6 corresponds to the troublesome singular value $\Sigma_{66} = 0$. Examination of the singular vector reveals why this is the case.

We can imagine the elements of the singular vector as describing eigen-currents. In row 6, this would describe a set of currents like those depicted in Fig. 5.24. In this case, if the coils all overlap perfectly, as they do in this simulation, such a mode has a net current of zero. Hence, no matter what the total current applied to this mode, it will never generate a magnetic field. Hence the singular value is always zero.

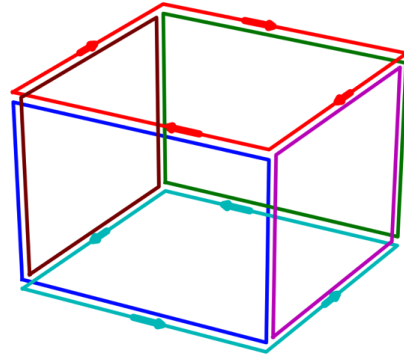
To understand this at a more fundamental level, we can write the field generated by coil c at the point \mathbf{r} as an expansion about the origin in terms of spherical harmonics $\Phi_{l,m}(r, \theta, \phi)$:

$$\mathbf{B}_c(\mathbf{r}) = I_c \sum_{l,m} \chi_c^{l,m} \Psi_{l,m}(\mathbf{r}), \quad (5.7)$$

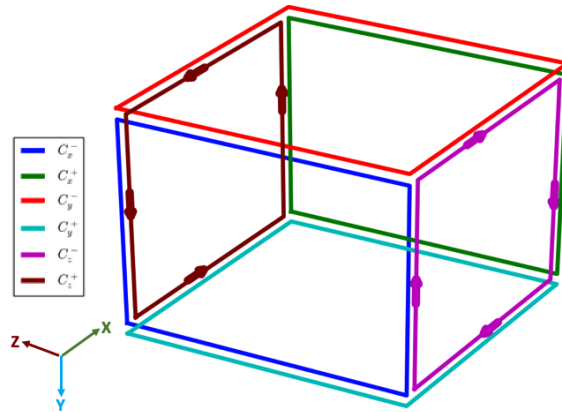
where $\chi_c^{l,m}$ is a constant with units nT/A/m^{l-1} that gives the efficiency of each mode



(a) Current Direction in C_x^\pm



(b) Current Direction in C_y^\pm



(c) Current Direction in C_z^\pm

Figure 5.24: Singular currents corresponding to the singular value $\Sigma_{66} = 0$. The currents are equal in magnitude but opposed in direction for each of (a) C_x^\pm , (b) C_y^\pm and (c) C_z^\pm . When added, the net current (and hence field) is always zero, thus explaining the singular value of zero.

and $\Psi_{l,m}(\mathbf{r}) = \nabla\Phi_{l,m}(r, \theta, \phi)$ gives the spatial dependence of the field components of the l, m -th mode of \mathbf{B} that satisfy magnetostatics in free space (*i.e.*, $\nabla \cdot \mathbf{B} = \nabla \times \mathbf{B} = \nabla^2 \mathbf{B} = 0$). The elements of matrix \mathbf{M} can now be written as

$$M_{sc} = \sum_{l,m} \chi_c^{l,m} \Psi_{l,m}(\mathbf{r}_s) \cdot \hat{\mathbf{e}}_s, \quad (5.8)$$

where $\hat{\mathbf{e}}_s$ is a unit vector along the direction of sensitivity of sensor s . The net field due to all coils detected by sensor s is therefore

$$B_s = \sum_c M_{sc} I_c \quad (5.9)$$

$$= \sum_{l,m} \left(\sum_c I_c \chi_c^{l,m} \right) \Psi_{l,m}(\mathbf{r}_s) \cdot \hat{\mathbf{e}}_s. \quad (5.10)$$

In regard to the matrix \mathbf{M} in Fig. 5.21 for the six overlapping coils, it is clear from Eq. (5.9) that all $B_s = 0$ when $|I_c| = I$ and the appropriate sign of the current in each coil is that shown in Fig. 5.24. What is more illuminating, however, is that the term in brackets in Eq. (5.10) must be uniquely zero for every mode l, m in this case. This insight provides a way forward for understanding and avoiding the ill-conditioned problem.

For example, for a set of cubic coils that are close to each other, but not perfectly overlapping, it will be impossible to make $\sum_c I_c \chi_c^{l,m} = 0$ for all l, m regardless the choices of I_c . This change in the coil configuration is ultimately reflected in different M_{sc} values, which subsequently result in a finite – rather than infinite – condition number, which is a step in the right direction. However, Σ_{66} will still be small in this case (due to the similarity of the new $\chi_c^{l,m}$ values with those of the perfectly overlapping case) and the problem with ill-conditioning would persist. A clear way to avoid ill-conditioning, however, would be to ensure that each coil generates a unique

mode, which is to say through the use of orthogonal coils. In this scenario, there are only as many modes as there are coils, and $\chi_c^{l,m} = 0$ for all but one of the coils for each mode. It is clear, then, that except for the trivial case where all $I_c = 0$, it will not be possible to generate a zero field mode, which is the signature of ill-conditioning.

In regard to the cubic coils of this study, a natural question becomes, in light of this analysis, how might one modify the coils or their operation so as to avoid the zero-field mode. The answer comes from both Fig. 5.24 and Eq. (5.10). From the current diagram in Fig. 5.24, it is clear that the sum of the currents of any two drawings is equal and opposite to that of the third. As a result, by not allowing the latter to exist (*e.g.* by tying the two coils together with the same current direction, say) the zero-field mode cannot be excited. This is equivalent to altering the values of $\chi_c^{l,m}$ through a modified coil configuration, which ultimately eliminates the possibility of the term in brackets in Eq. (5.10) from being zero for every l, m .

This idea was implemented in the Python code by requiring that the currents in the C_z^+ and C_z^- always be in the same direction and have the same value, *i.e.* like the currents in a Helmholtz coil. This means that there are only five independently controlled currents, which we denote C_x^+ , C_x^- , C_y^+ , C_y^- , and C_z^\pm . More about the coils that generate spherical harmonics are discussed in Section 6.2.4.

The simulated matrix \mathbf{M} for this configuration is shown in Fig. 5.25. Naively, it is not considerably different in terms of the corresponding matrix for six coils, which was displayed in Fig. 5.21. However, upon performing the singular value decomposition, the differences become evident.

Figure 5.26 displays the Σ matrix resulting from singular value decomposition.

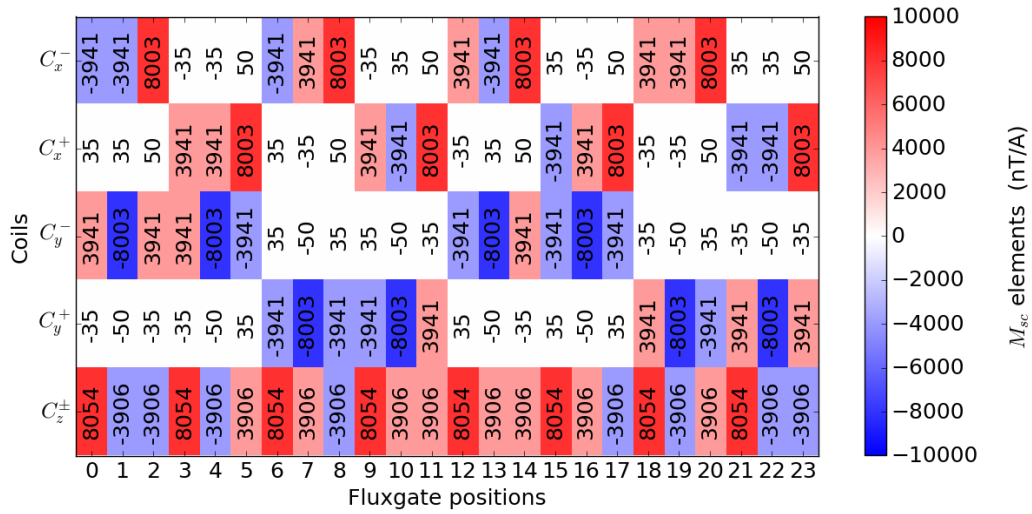


Figure 5.25: Color map of M_{sc} elements for 24 fluxgate axes and 5 coils. Coil dimensions and fluxgate positions are the same as for Fig. 5.21.

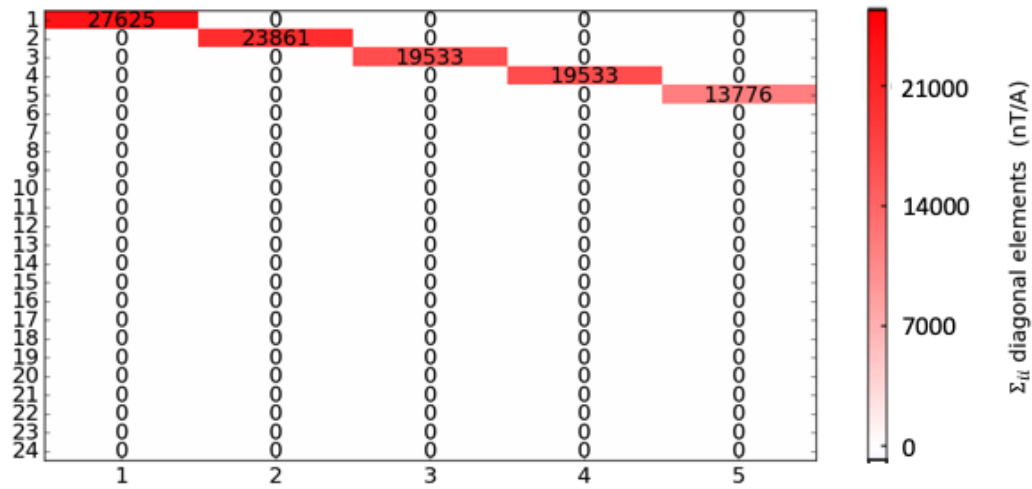


Figure 5.26: Color map of diagonal matrix Σ found by SVD of simulated M for 24 fluxgate axes and 5 coils.

This results in five singular values, one for each coil mode. Most importantly, the singular value which was zero has been removed from the matrix. The remaining singular values are now also all of similar order of magnitude. The condition number

of the matrix is 2.01, which is a considerable improvement compared to the infinite condition number of the six-coil system.

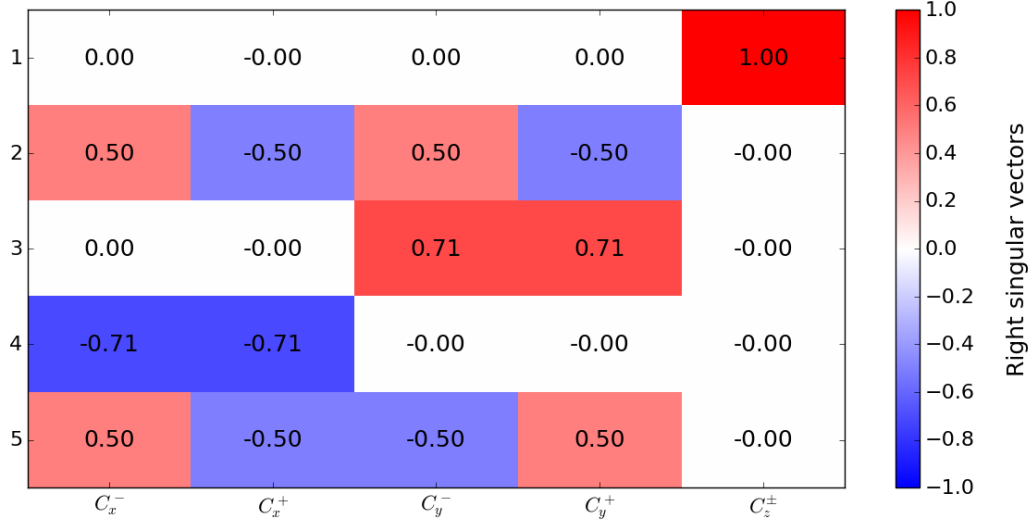


Figure 5.27: Color map of orthogonal matrix \mathbf{V}^T found by SVD of \mathbf{M} 24 fluxgate axes and 5 coils.

The matrix of right singular vectors \mathbf{V}^T is displayed in Fig. 5.27. The uniform field modes are clearly visible in rows 1, 3, and 4, corresponding to Helmholtz-like singular current modes. Two gradient modes also appear in rows 2 and 5, which are different combinations of the anti-Helmholtz-like gradients in each of the x and y directions.

This solution was then implemented into the active magnetic compensation system. Rather than physically wire two coils together, a software solution was used where the currents in one pair of opposing coils were required to be equal and run in the same direction.

The results of matrix measurement followed by singular value decomposition are

Coils	Matrix Condition Number	Inverse Matrix Condition Number	Regularization Parameter r
$C_x^-, C_x^+, C_y^-,$ C_y^+, C_z^- and C_z^+	26.37 (25.96)	1.71 (1.61)	3.04 (2.96)
$C_x^\pm, C_y^-, C_y^+,$ C_z^- and C_z^+	2.26 (2.05)	1.08 (1.06)	3.60 (3.57)
$C_x^-, C_x^+, C_y^\pm,$ C_z^- and C_z^+	2.27 (2.04)	1.09 (1.06)	3.62 (3.54)
$C_x^-, C_x^+, C_y^-,$ C_y^+ and C_z^\pm	2.41 (2.09)	1.10 (1.07)	3.56 (3.50)

Table 5.2: Matrix properties for different 6- and 5-coil configurations for fluxgate sensors at 1, 3, 6 and 8. The values inside the parentheses indicate the calculation done with shield present.

shown in Table 5.2. Since 4×3 fluxgate axes could be instrumented, only such matrices were considered. The measurements shown inside and outside the parentheses were done with and without the magnetic shield within the coil cube. It is seen that they are similar as expected from the discussion in Section 5.3.2.

Table 5.2 shows that the condition number of the matrix is reduced by more than a factor of ten when comparing the six-coil solution to the five-coil solution. Configurations where opposing coils in the x , y , and z directions are alternately selected for the Helmholtz-like current configuration in the five-coil solution. Table 5.2 shows that any of these configurations gave essentially the same results for the condition

number.

Clearly, in the six-coil case, it is an absolute necessity to regularize the matrix. As discussed earlier, this may be done by adjusting the regularization parameter to minimize the condition number of the Tikhonov regularized pseudoinverse. Tikhonov regularization was also studied for the five-coil case, to see if it had any impact on the PI feedback system. Results of the Tikhonov regularization process are also displayed in Table 5.2.

Figure 5.28 shows experimental data which demonstrate the success of the five-coil method compared to the six-coil method. In this case, we have compared the matrices with our regularization method, determining the best value of r based on its ability to minimize the condition number of the resultant pseudo-inverse (see Section 5.5.2). Figs. 5.28(a) and (b) correspond to the settings described in the first two rows of Table 5.2.

The main success is that in the five-coil algorithm, the currents settle rapidly after the excitation coil has been switched on, and return rapidly to their initial values when switched off. This can be contrasted with the six-coil algorithm where the current drifting problem is quite evident: the coil currents take more than ten seconds to settle.

Another clear success is that in the five-coil case, the coil C_z^+ , which is *closest* to the perturbation coil, is the one that has the most current driven by the feedback algorithm. Certainly this would be the expected result. In the six-coil case, Fig. 5.28(a) demonstrates that the initial coil responses are quite similar to the five-coil method (within the first < 1 s), but then the current drifting problem sets in, and the cur-

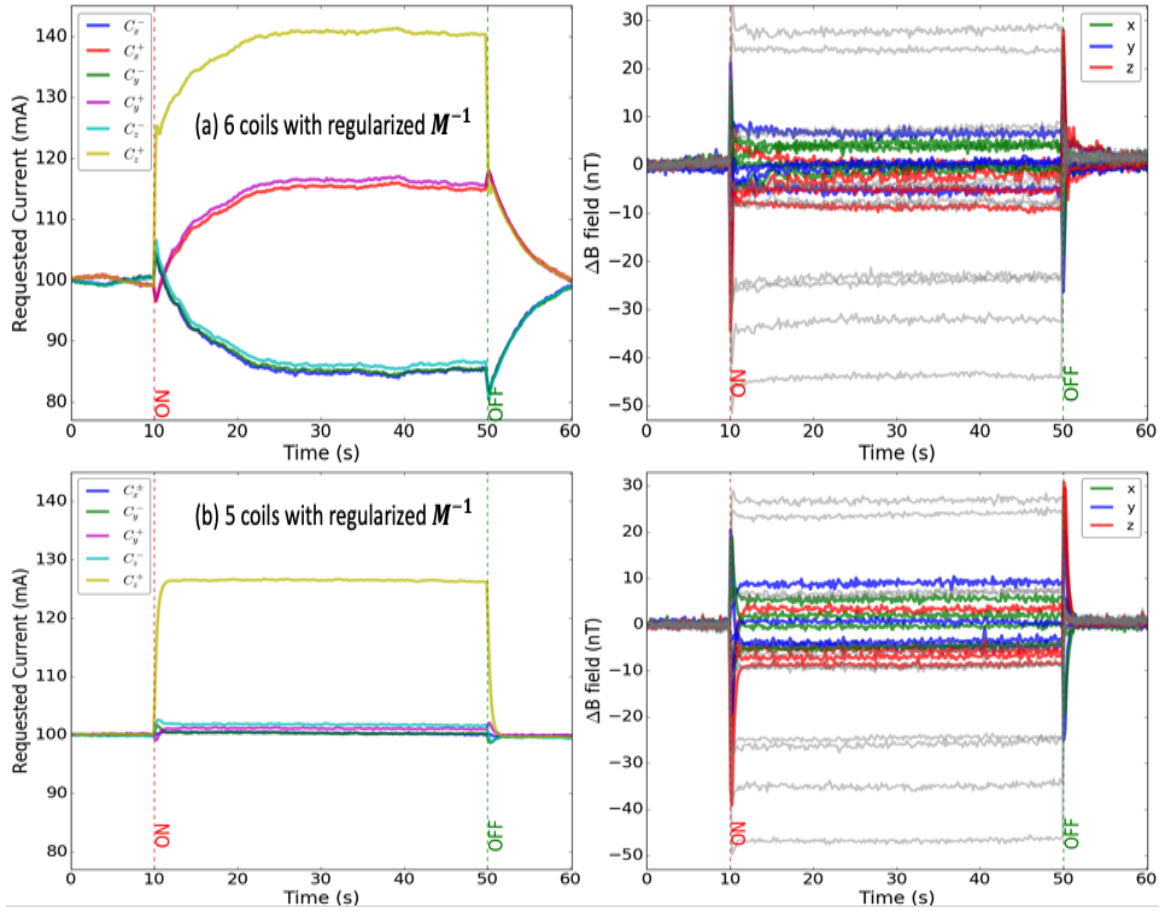


Figure 5.28: (a) 6-coil feedback algorithm compared with (b) 5-coil feedback algorithm, where the only change is that the currents C_x^+ and C_x^- are required to be a common current C_x^\pm . Both pseudoinverses have been regularized using the method described Section 5.5. Coil currents are shown in the left panels while magnetic field changes are shown in the right panels. In both (a) and (b), the feedback parameters are $k_c^p = 0.0$ and $k_c^i = 1.0$.

rents grow in coils where one would expect them to be small. The growth of the problematic mode with singular value zero is also quite evident in the six-coil case: the currents in opposite coils have opposite changes relative to the initial current and

are roughly equal in magnitude. This is the mode that in the ideal simulation does not generate any magnetic field. Because of the smallness of the effect of this mode, the six-coil algorithm tends to set the current to a somewhat arbitrary value.

In both the five-coil and six-coil cases, the overall results for the reduction in the magnetic field at the control sensor positions are quite similar. Some small, longer term drifts in the six-coil case can be seen. We expect that this happens because the field generated by the problematic mode is small but non-zero, because the coils do not exactly overlap as they do in the ideal simulation. There is some evidence that there is additional higher frequency noise in the six-coil case, which could be coming from the considerably larger and less stable currents generated by the problematic mode.

So, while the two algorithms give similar results for the generated magnetic fields, clearly the five-coil algorithm is more desirable because smaller coil currents with smaller random fluctuations are generated. The five-coil system is clearly responding to a field in the z -direction that is located near the C_z^+ coil.

The five-coil algorithm can even be operated without the need for Tikhonov regularization of the pseudo-inverse. Figure 5.29 compares the six-coil and five-coil algorithms when no regularization is performed. The five-coil case performs well, perhaps even better than the results displayed in Fig. 5.28(b) because the field fluctuations are smaller. This might also indicate that the PI feedback parameters are not fully optimal, since more overshoot is also evident in Fig. 5.29(b) when compared to Fig. 5.28(b). For this study, the feedback parameters were held constant, and in Section 5.5, a relationship between these parameters was shown. Additional

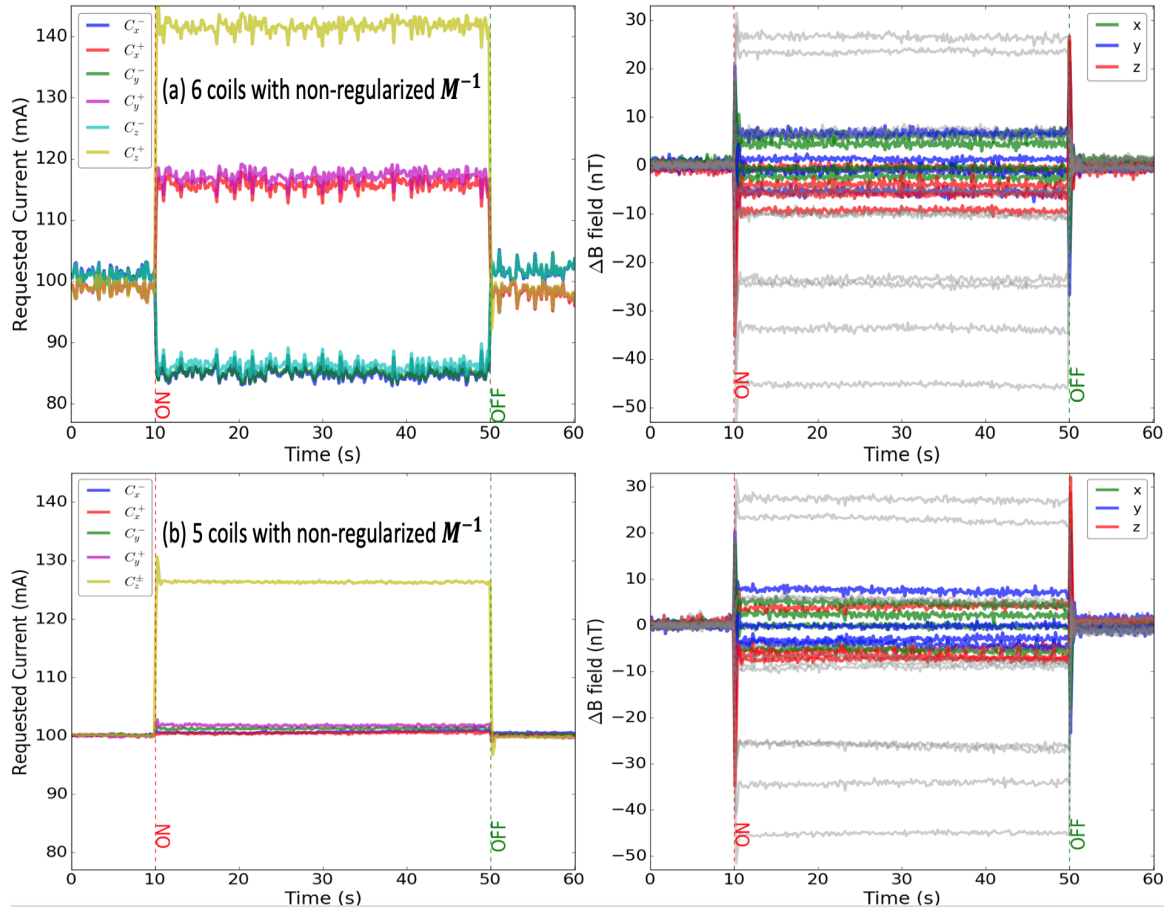


Figure 5.29: (a) 6-coil feedback algorithm compared with (b) 5-coil feedback algorithm, where the only change is that the currents C_x^+ and C_x^- are required to be a common current C_x^\pm . No regularization of the pseudoinverse has been done in either case. All other parameters are the same as for Fig. 5.28.

optimization is possible and could affect this conclusion.

In general, we expect that the non-regularized solution is superior. Tikhonov regularization introduces additional constraints in order attempt to keep a poorly conditioned feedback system from oscillating. It is a superior principle to design the system to be well-conditioned rather than relying on Tikhonov regularization to solve

the problem of ill-conditioning. This is also one of the general conclusions of Ref. [71].

In Figs. 5.21 and 5.25, the ideal simulation results of the matrix \mathbf{M} is shown. The matrix \mathbf{M} measured experimentally is similar in its structure to these simulation results.

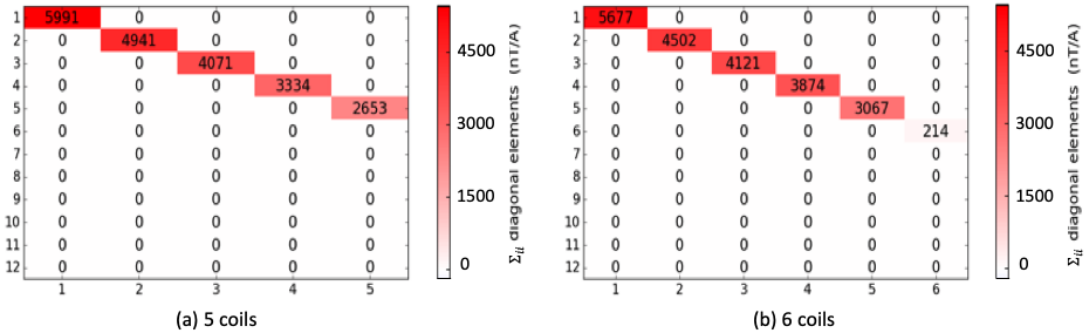


Figure 5.30: Color map of diagonal matrix Σ found by SVD of experimentally measured \mathbf{M} for the available 12 fluxgate axes and for (a) 5 coils, where the C_x^\pm coils are required to carry the same current, and (b) 6 coils which, are permitted to carry any current.

It is interesting to compare the results for the diagonal matrix Σ in simulation and experiment. The experimental results for Σ are presented in Fig. 5.30, for both the five-coil and six-coil case. These can be compared with the simulated results which were presented in Figs. 5.26 and 5.22. It can be seen that, despite having only 12 fluxgate axes available experimentally, the Σ matrices compare favorably with the simulated counterparts. In general the matrix elements are smaller experimentally, but this is simply because the fluxgates were located about 8-10 cm inside the corner positions of the coil cube, whereas in the previously presented simulations, they were only 2 cm inside and hence were closer to the coils.

The main similarity is in the trends of the singular values and in the condition number of the matrix. In the five-coil case, the singular values are all the same order of magnitude, and the condition number is 2.26 (see also Table 5.2). In the six-coil case, the first five singular values are of similar orders of magnitude, and the sixth is significantly smaller. In the simulation (Fig. 5.22), this singular value was exactly zero. We expect the difference (zero vs. non-zero) is due to the currents not exactly overlapping in the experimental case.

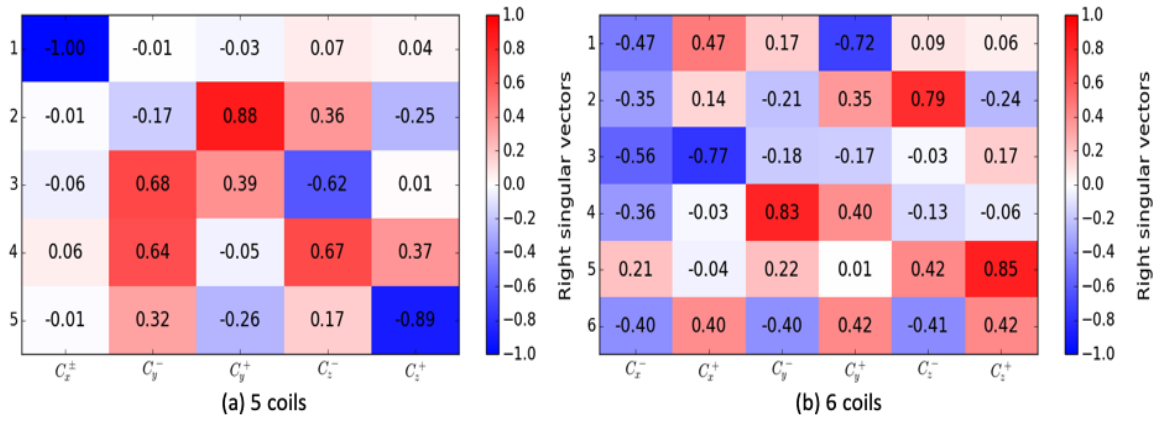


Figure 5.31: Experimentally determined right singular vectors, represented by the rows of the matrix \mathbf{V}^T resulting from SVD of the experimentally measured matrix \mathbf{M} .

Similarities can also be seen in the right singular vectors, described by the rows of the \mathbf{V}^T matrix. The experimental results for the right singular vectors are presented in Fig. 5.31 and can be compared with the simulation results which were presented in Figs. 5.23 and 5.27. In Fig. 5.31(b), the problematic mode corresponding to the smallest singular value can indeed be seen to result from opposing currents of nearly equal magnitude being generated in each of the six coils. In the five-coil experimental

results shown in Fig. 5.31(a), a similar pattern of singular vectors can be seen as for the simulated version presented in Fig. 5.27. Row 1 corresponds to the uniform field in the x -direction. Rows 2 and 5 appear to correspond to admixtures of gradients in the y and z directions. Row 3, having two red values in C_y^+ and C_y^- most closely corresponds to a uniform field in the y -direction, whereas row 4 corresponds most closely to the uniform field in the z -direction. There is some admixture of the identities of the singular vectors which are likely due to some experimental geometrical imperfections.

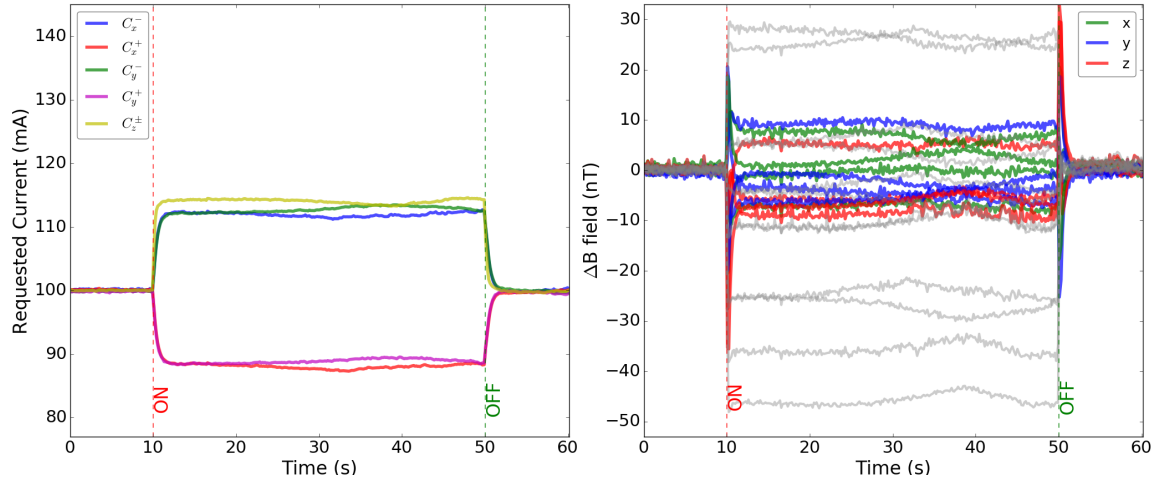


Figure 5.32: Five-coil feedback algorithm, where the currents C_z^+ and C_z^- are required to be a common current C_z^\pm . Tikhonov regularization of the pseudoinverse has been done, although the results would be very similar even without this. All other parameters are the same as for Fig. 5.28.

In Fig. 5.28(b), it was shown that the dominant current response to the excitation coil was in the C_z^+ coil. The reason for this is that the C_z^+ coil is located at the closest position and in the correct direction to cancel the field coming from the excitation coil. For that study, the C_x^\pm coils were required to have a common current. We were

interested to study the effect on the five-coil feedback algorithm if common current was required in the C_z^\pm coils instead.

The results of this alternate choice are shown in Fig. 5.32. Turning on the excitation coil indeed causes the common C_z^\pm current to become more positive with have the change of the previous result for C_z^+ in Fig. 5.28(b). The system now must generate a large gradient in the z -direction. This can now only be achieved by excitation of the other four coils as shown in Figs. 5.24(a) and (b).

We think an interesting point in this case is that, for this particular positioning of the perturbation coil, it would clearly be desirable for the system itself to be able to generate different currents in C_z^+ and C_z^- if aiming to have the smallest changes in the currents.

The tests were also redone with the magnetic shield inside the coil cube. Not surprisingly, the conclusions were the same.

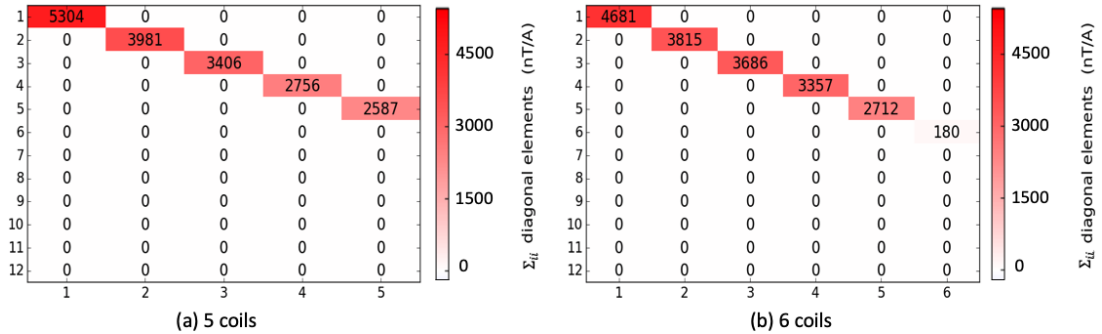


Figure 5.33: Color map of diagonal matrix Σ with the magnetic shield in place found by SVD of experimentally measured \mathbf{M} for the available 12 fluxgate axes and for (a) 5 coils, where the C_x^\pm coils are required to carry the same current, and (b) 6 coils which, are permitted to carry any current.

Figure 5.33 shows the results for the Σ matrix when the magnetic shield is in place. The general trends in the singular values are very similar as in the case without the magnetic shield. As reported in Table 5.2, the condition number in the five-coil case is 2.05 and in the six-coil case it is 25.96.

The right singular vectors corresponding to the coil modes also show similar trends. For the six-coil case, the same problematic mode is present. For the five-coil case, the same general mode structure is apparent, consisting of three uniform field modes and two gradient modes in the same pattern.

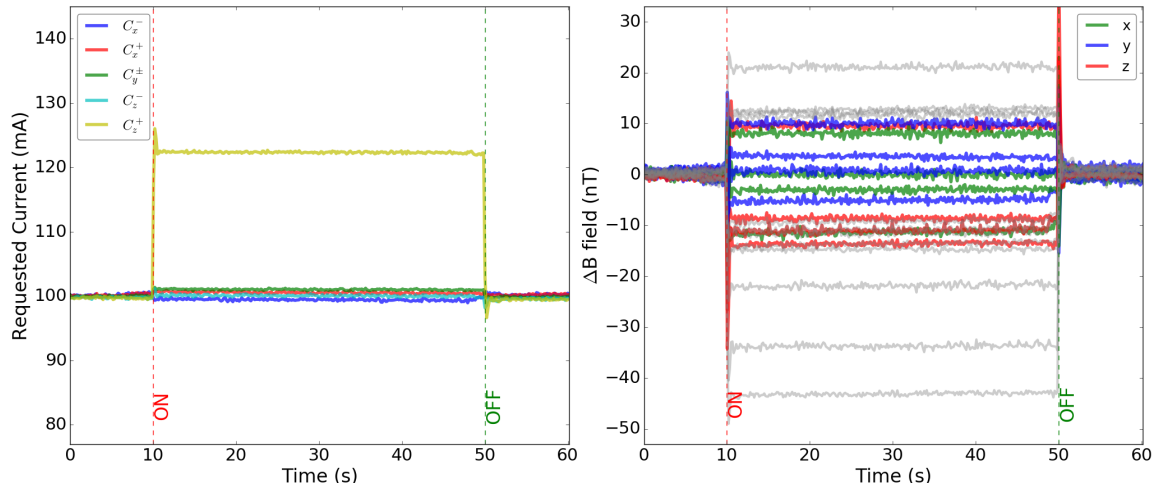


Figure 5.34: Five-coil feedback algorithm with the magnetic shield placed inside the coil cube. The currents C_y^+ and C_y^- are required to be a common current C_y^\pm . All other parameters are the same as for Fig. 5.28.

The improvement in the general feedback system operation for the five-coil feedback algorithm is also very clear when the magnetic shield is within the coil cube. Results of the usual test with the excitation coil are shown in Fig. 5.34, where the non-regularized pseudo-inverse has been used. For Fig. 5.34, the C_y^+ and C_y^- coils

have been required to carry a common current C_y^\pm while the other five coils may be adjusted freely. Even with the magnetic shield present, the results are very similar to Fig. 5.29(b) where no shield was present. The results were also compared with redid in PI simulations and a similar behaviour was observed as expected.

5.8 Other metrics of feedback system performance

In Section 4.6, some additional quantitative measures of the magnetic compensation performance were introduced. These metrics had been used in the previous studies of Refs. [69–71]. The two metrics that will be discussed further in this section are

- the readings of central internal sensors when the compensation system is used, and
- the Allan standard deviation, which is used to gauge the effectiveness of corrections over long timescales.

The general conclusion of these studies is that they are in qualitative agreement with the previous works of others. We also believe that one of the main limiting factors relates to the need for more advanced coil design, which is discussed further in Chapter 6.

5.8.1 Internal Sensor Perturbations

Most of the results that was showed so far are related to the magnetic field measured by 12 fluxgate sensors positioned within the coil cube just outside the region of interest. Normally when these data were taken, we simultaneously acquired data for

two additional fluxgate axes placed centrally within the coil cube. These sensors were not used in the feedback algorithm. The idea was to use these as a way to estimate average feedback system performance within the region of interest.

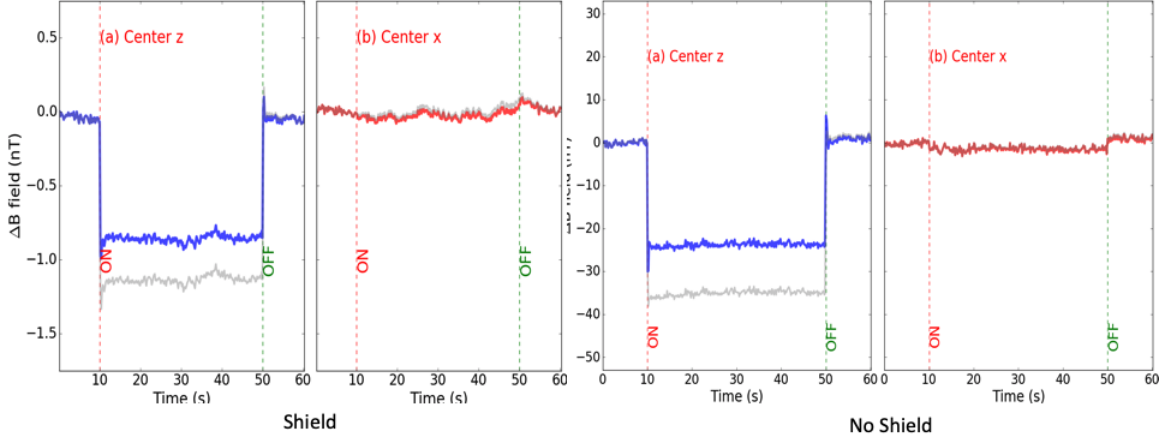


Figure 5.35: Central magnetic field in the z (blue) and x (red) directions. The 6-coil feedback algorithm was used. The left graphs show the case when the magnetic shield (the outermost layer of the 4-shell system) is present. The right graphs show the case when no magnetic shield is present. A current of 10 mA was applied to the perturbation coil.

Figure 5.35 shows the magnetic fluctuation reduction on the central sensors in z , and x axis for the 6-coil feedback algorithm discussed in the previous Section. Results are compared when the outermost magnetic shield of the four-shell magnetic shielding system is present. The presence of the magnetic shield reduces the perturbation of the central field by a factor of 25. Otherwise the results are quite comparable, showing a similar fractional reduction of the effect of the perturbation, which is dominantly in the z direction. The central field in the z direction is reduced by a factor $\sim 2/3$.

The results are virtually identical if the 5-coil feedback algorithm is used (Fig. 5.36).

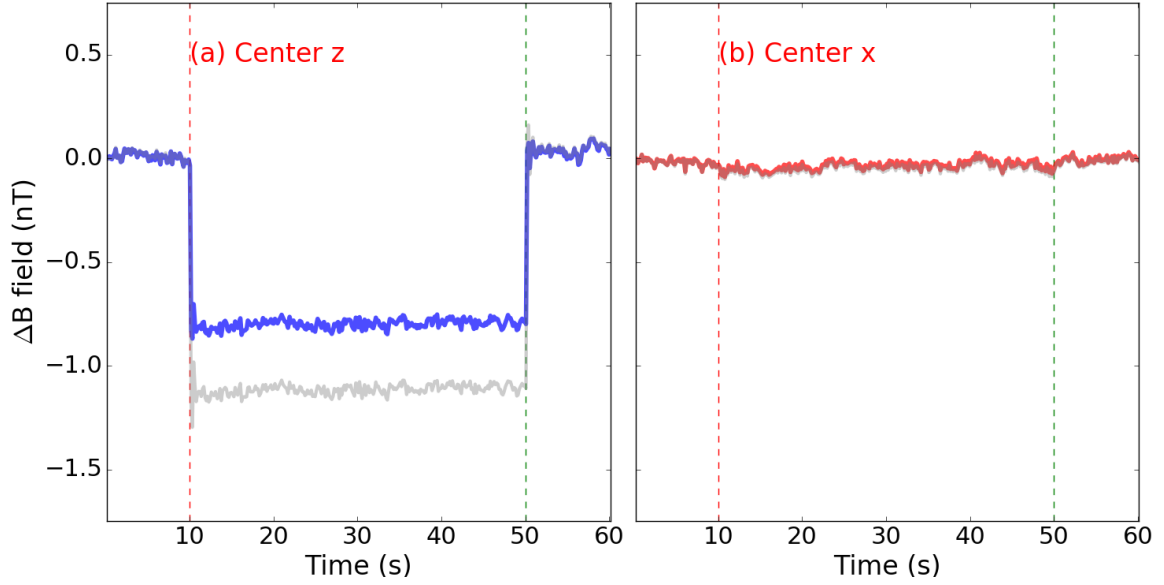


Figure 5.36: Central magnetic field in the z (blue) and x (red) directions. The 5-coil feedback algorithm was used, with the currents C_x^\pm being constrained to be equal. The outermost layer of the magnetic shielding system was placed around the sensors and within the coil cube.

This is not surprising because generally the magnetic field results were often quite similar for the 5- and 6-coil algorithms when properly tuned, despite the currents in the 6-coil algorithm experiencing the current drifting problem.

We also did various other trials varying the feedback system parameters, and adjusting the current applied to the perturbation coil, both with and without the magnetic shield present. In general the reduction in the central z field was similar.

While it is not a large reduction, the result is relatively consistent with our results for the general reduction in the field at the external sensor sites when the feedback system is used to correct the effect of the perturbation coil (see the previous Section). In that case also, the general reduction in the field at the external sensor sites was by

a factor of roughly 1/2 to 2/3 on average. We expect that in order to provide better overall compensation results, the chief improvement will be in coil design, which was beyond the scope of this thesis.

5.8.2 Allan Deviation Results

The definition of the Allan standard deviation and the “shielding factor” were discussed in Section 4.6. Recall that the shielding factor is the ratio of the estimated uncompensated Allan deviation to the Allan deviation of the measured external fluxgate sensors.

This Section presents our results for Allan deviation measurements under two conditions:

- “Natural” fluctuations with feedback on. In this case we tried to compensate typical environmental changes in the magnetic field in the laboratory at U. Winnipeg.
- Simulated drift, where the current in the perturbation coil was ramped slowly over a long time, to see how well the feedback system could correct a linear drift.

In each case, the feedback system provided a shielding factor (ratio of uncorrected to feedback-corrected Allan deviations) larger than one.

Figure 5.37 shows a measurement of fluxgate readings over a 24-hour period with the feedback system switched off. This gives an impression of the overall scale of the fluctuations that the feedback algorithm must correct. It was based on measurements

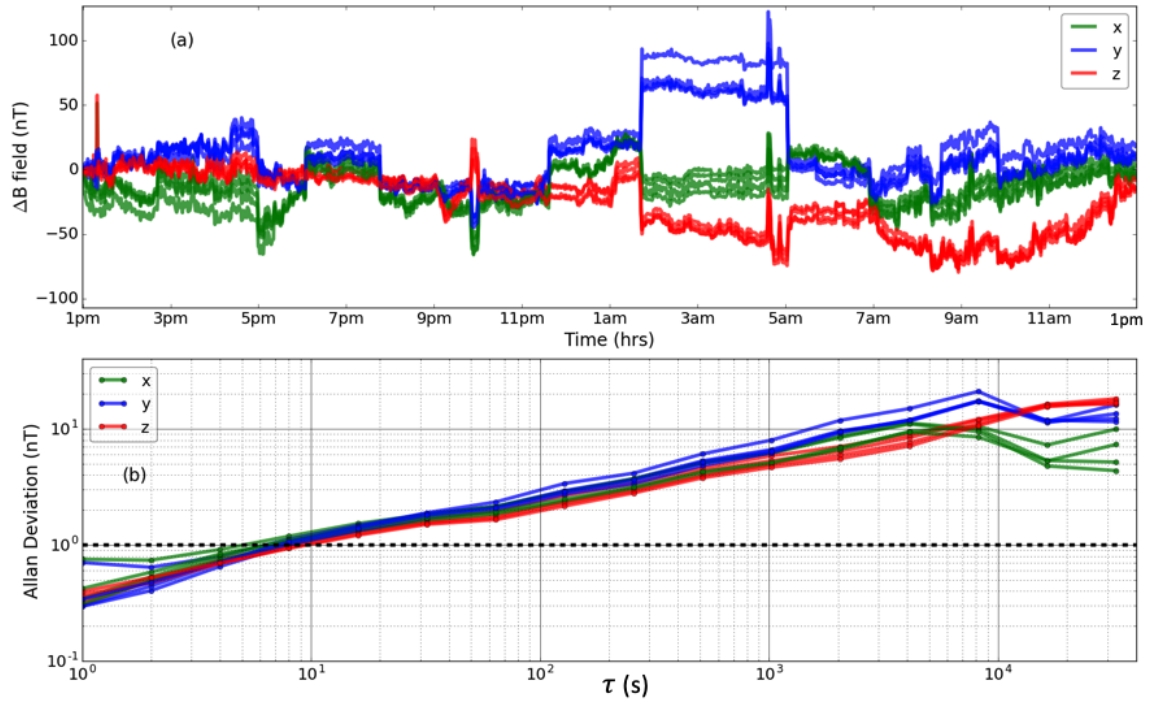
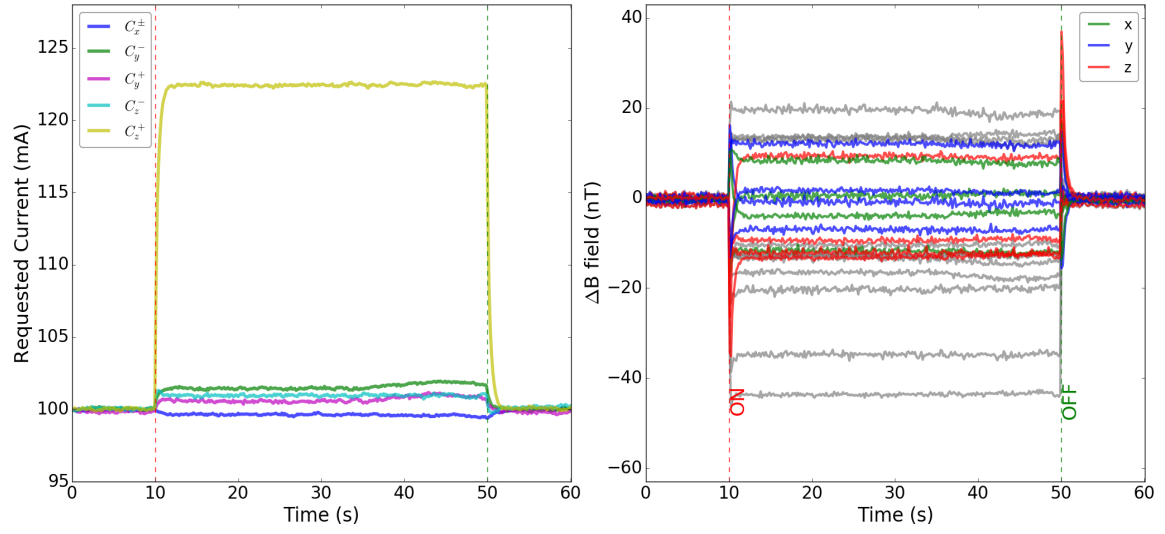


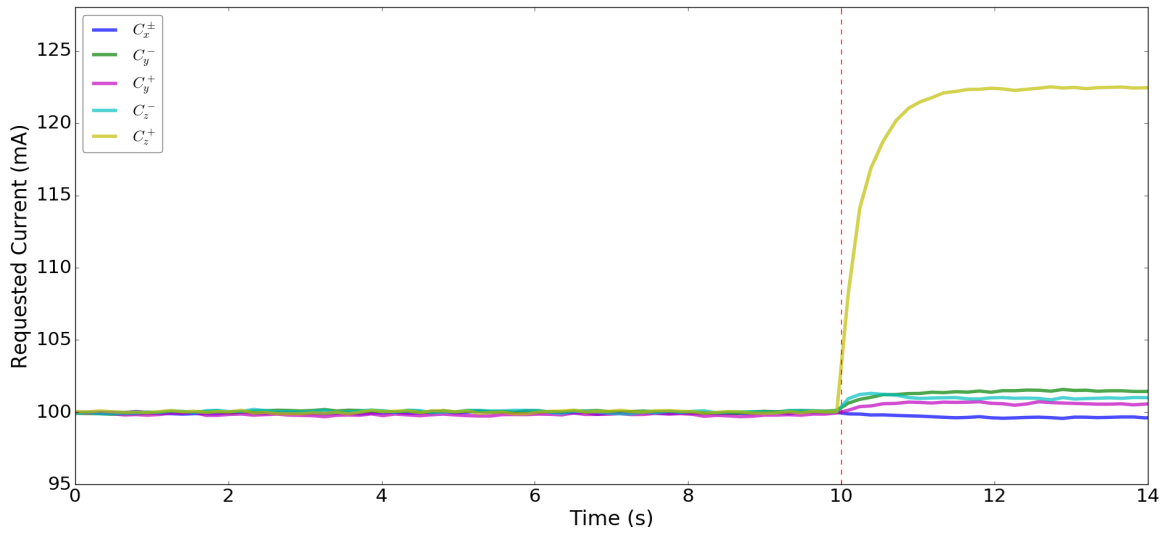
Figure 5.37: (a) Field change ΔB in 12 fluxgate sensors placed within the coil cube for 24 hrs with feedback algorithm switched off. (b) Corresponding Allan deviation.

like this that feedback system was designed with a dynamic range capable of correcting a few hundred nT in the fluxgate readings. The Allan deviation shown in Fig. 5.37(b) typically rises with a $\tau^{1/2}$ - $\tau^{1/3}$ dependence, which is similar to a 1D random walk.

In order to ensure that the feedback system will not induce noise at higher frequencies, the PI parameters were re-tuned, resulting in reasonable values of $k_c^p = 0.1$ and $k_c^i = 0.37$. The response of the system to a step perturbation with this re-tuning is shown in Fig. 5.38. The main feature to be observed is the coil currents do not experience and overshoot and appear more like a critically damped solution than in the previous sections. This does not have much effect on the long-time behavior of the system, and keeps the noise at higher frequencies (near the loop correction frequency



(a)



(b)

Figure 5.38: (a) 5-coil feedback algorithm with the currents C_x^+ and C_x^- required to be a common current C_x^\pm . Coil currents are shown in the left panel while magnetic field changes are shown in the right panel, (b) zoomed coil currents near the time when the perturbation coil is engaged. The feedback parameters are $k_c^p = 0.1$ and $k_c^i = 0.37$.

of 6 Hz) suppressed. In this way the shielding factor (ratio of Allan deviations) at 1 s is always $\gtrsim 1$.

The feedback algorithm corrects the natural field fluctuations well. Figure 5.39 shows the results of a run over a 4096 s period (just over an hour). In Fig. 5.39(a), it can be seen that in general the fluctuations in the fluxgate readings are reduced compared to their expected values. This is also seen in the Allan deviations shown in Fig. 5.39(b), where the uncorrected readings (shown in grey) are seen generally to have a larger Allan deviation than the corrected readings (shown by the colored curves). In Fig. 5.39(c), the ratio of Allan deviations (uncorrected/corrected), which is defined as the shielding factor, is shown. In general the shielding factor is larger than one and less than about 2. For longer averaging times, x - and y -axis shielding factors of some of the sensors drop below one, indicating that the system failed to stabilize the magnetic fluctuations in these directions. However, on average the feedback system improved the fluxgate reading stability over time. For the longest times $\tau \gtrsim 100$ s, there is also some increased statistical fluctuation in the data.

Figure 5.40 shows the behavior of the coil currents for this run over time. It can be seen that the currents are indeed responding to changes seen in the magnetic field, for example the step feature near $t = 3500$ s.

In these particular hour-long runs, a common feature was that the variations in field were smaller than over a typical 24 h period. It is just a coincidence that the environment happened to be quieter during these runs.

The results of another similar hour-long sample run are shown in Figs. 5.41 and 5.42. The general observations are similar. This run had some increased noise

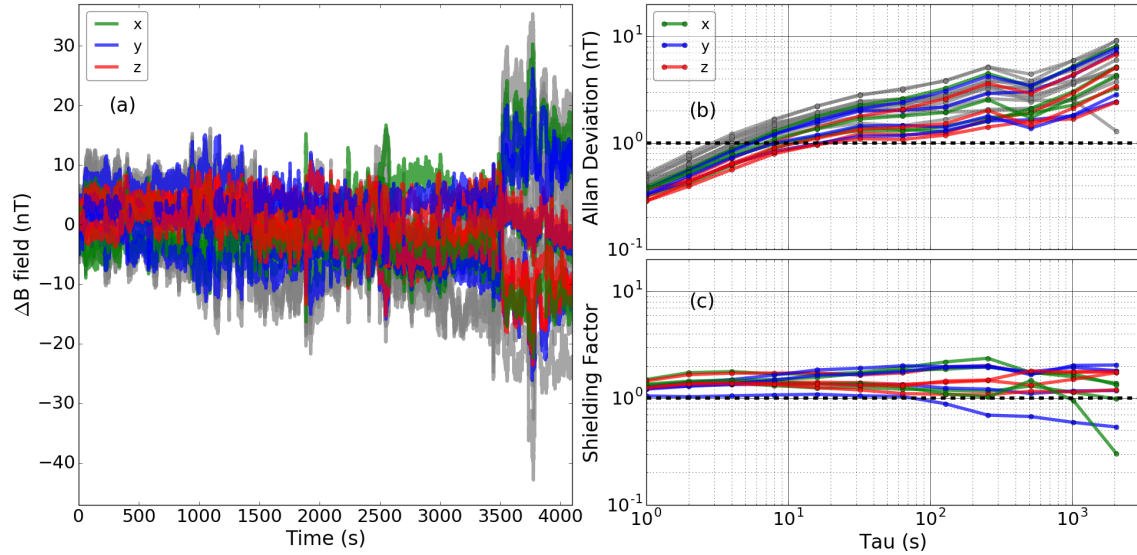


Figure 5.39: 5-coil feedback algorithm for “natural” fluctuations. (a) Magnetic field changes ΔB over time (b) Allan deviation, and (c) shielding factor. Grey curves show the results for the estimated uncorrected field values. The feedback parameters are $k_c^p = 0.1$ and $k_c^i = 0.37$.

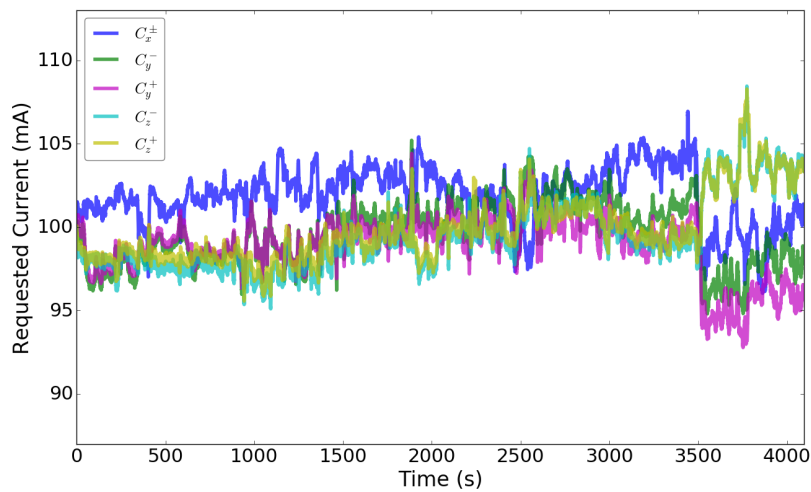


Figure 5.40: Coil currents for the run shown in Fig. 5.39.

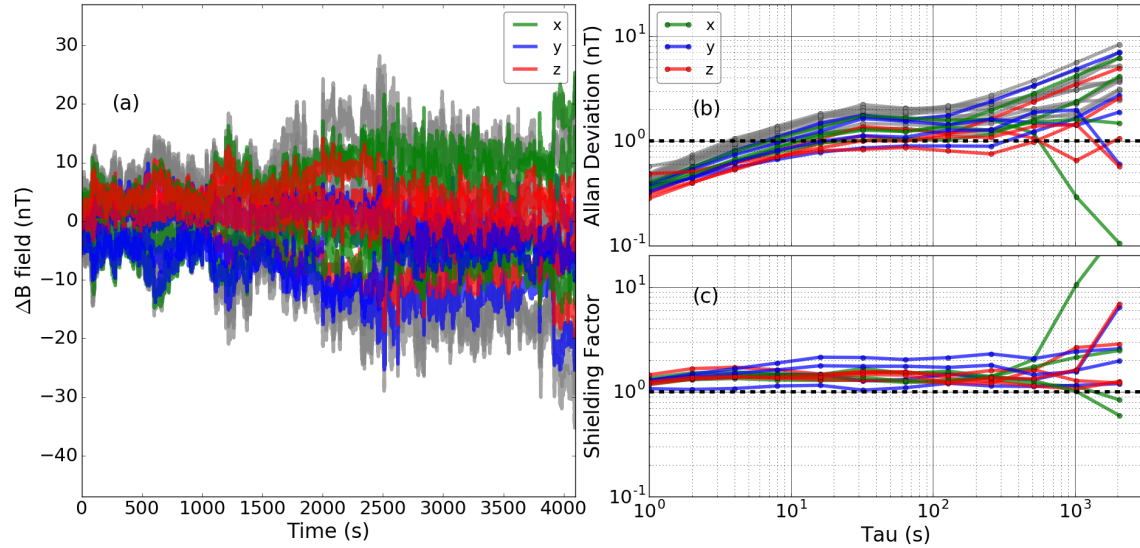


Figure 5.41: Second example run of 5-coil feedback algorithm for “natural” fluctuations. (a) Magnetic field changes ΔB over time (b) Allan deviation, and (c) shielding factor. Grey curves show the results for the estimated uncorrected field values. The feedback parameters are $k_c^p = 0.1$ and $k_c^i = 0.37$.

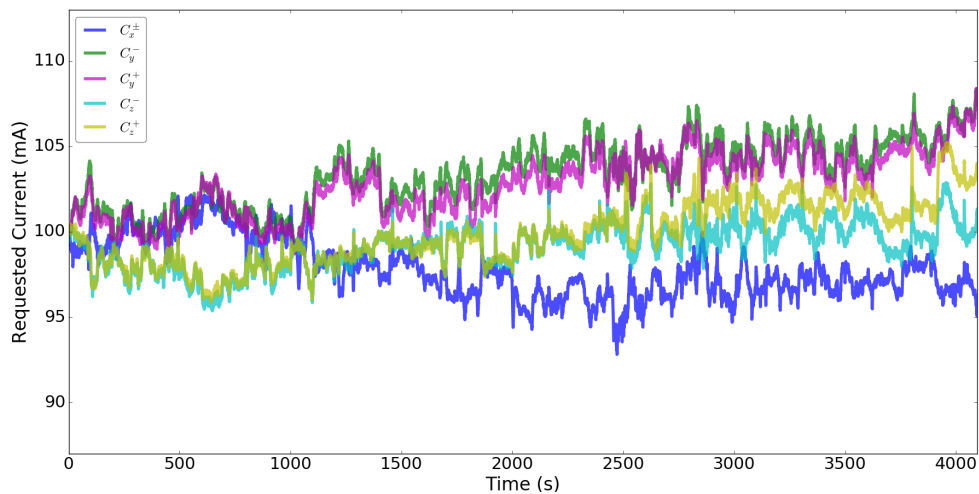


Figure 5.42: Coil currents for the run shown in Fig. 5.41.

which begins at about $t = 2500$ s. Nonetheless the feedback algorithm keeps the shielding factor generally above one.

In order to induce a long-term drift in the fluxgate signals, we also conducted runs where we slowly ramped the current in the perturbation coil over the 4096 s measurement period. The results of one such run are shown in Figs. 5.43 and 5.44. In Fig. 5.43, it can be seen that all the fluxgate signals ramp slowly over time, in addition to experiencing the usual smaller environmental changes. Otherwise, in terms of the Allan deviation, the feedback system performs similarly to before. The different form of the long-term drift in the perturbation manifests itself as a linear dependence of the Allan deviation at long times, as can be seen in Fig. 5.43(b). But the shielding factor (Fig. 5.43(c)) is generally still with the range of 1 to 3. Figure 5.44 shows that the perturbation coil generally affects the current C_z^+ in the coil closest to the perturbation coil, as seen previously when a step in current is applied to the perturbation coil and when using this 5-coil feedback system configuration.

Figs. 5.45 and 5.46 show another example run where the current in the perturbation coil was ramped. This run is somewhat unique in that it experienced very little environmental noise over the course of the run. This is seen through the Allan deviation in Fig. 5.45(b) which rises more slowly than usual, smoothly transitioning to a linear dependence at long times because of the drift induced by the ramping of the perturbation coil. Otherwise the behavior is quite similar to the previous example.

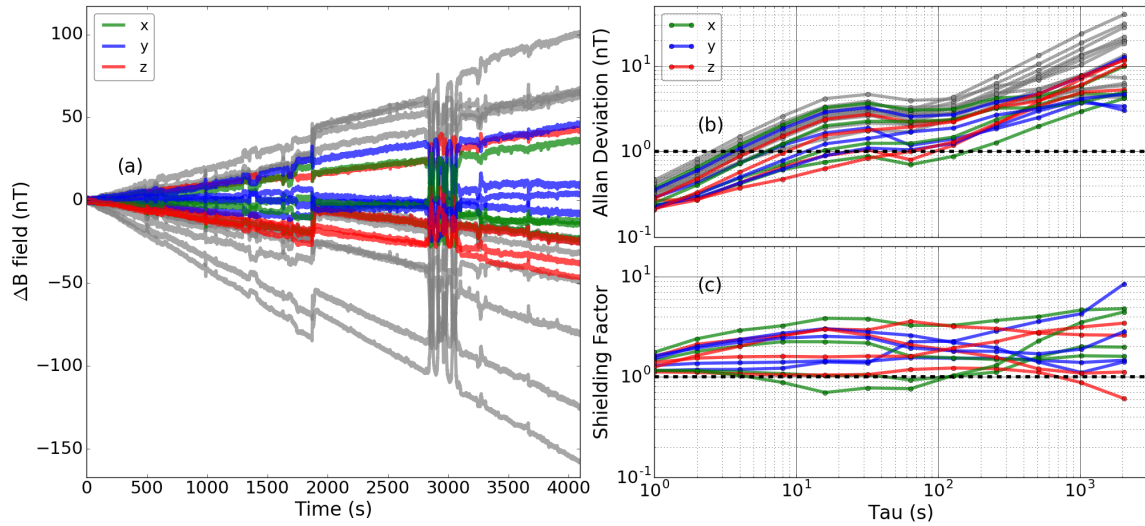


Figure 5.43: Correcting a slowly ramped current in the perturbation coil. (a) Magnetic field changes ΔB over time (b) Allan deviation, and (c) shielding factor. Grey curves show the results for the estimated uncorrected field values.

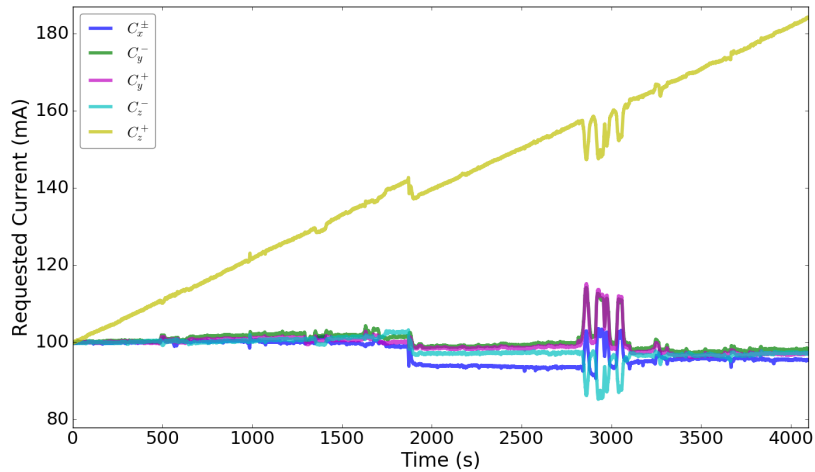


Figure 5.44: Coil currents for the run shown in Fig. 5.43.

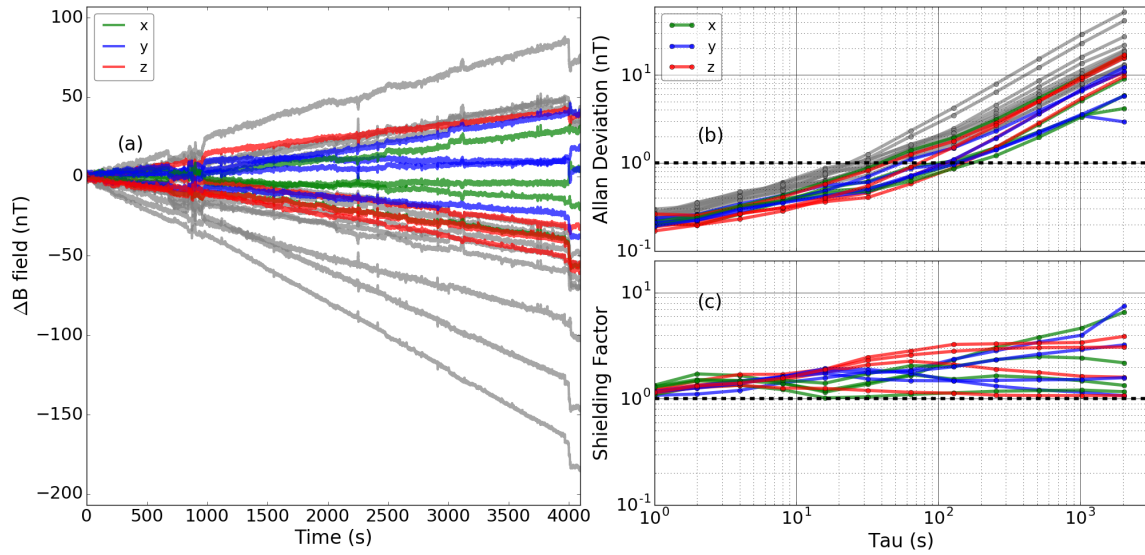


Figure 5.45: Second example run correcting a slowly ramped current in the perturbation coil. (a) Magnetic field changes ΔB over time (b) Allan deviation, and (c) shielding factor.

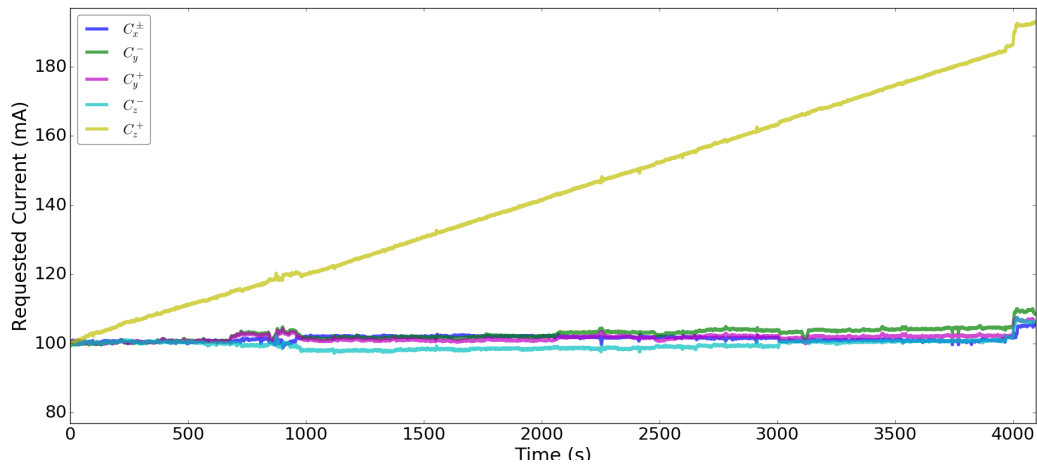


Figure 5.46: Coil currents for the run shown in Fig. 5.45.

Chapter 6

Conclusion

6.1 Key Findings

The goal of my MSc thesis work was to develop a working AMC prototype using multi-dimensional PID control to compensate magnetic field fluctuations, based on the work of Refs. [69, 70]. This primary goal was successfully achieved and the work went beyond well beyond that in several respects. In the process of developing the system, I discovered a host of new challenges, to which I found innovative solutions. Below I list the key improvements made to the system and the results of those improvements. They are the following:

1. **4th order low pass Butterworth filter**

I designed active filters which are excellent in reducing high frequency noise, even slightly better than the low pass filter (LPF) of Bartington's SCU1. The filters will be important for future studies facing high frequency (> 10 Hz) noise issues. The filters could be improved further by designing them with variable

gain and offset, which is an advantage of the SCU1. This would make it easier to adjust the range of values passed to the DAQ module, without much additional noise. An important example would be to amplify and acquire signals from fluxgates located inside the passive shielding where all magnetic fields are very small. In such cases, I used the SCU1 with gain 100 so that it can easily be read by the ADC. This is one reason that in my case, to acquire the fluxgate signals placed inside the shield within the coil cube. In such cases, I used the SCU1 with gain 100 so that it can easily be read by the ADC.

2. Finite Element Analysis and Multi-dimensional PI control simulation

The simulation of the prototype AMC system was vital to demonstrate a full understanding of the experimental results. Finite element analysis (FEA) was used to generate both the matrix \mathbf{M} and the field change ΔB due to the perturbation coil for any number of the sensors placed within the coil cube. The FEA results were then used in a time-dependent PI feedback algorithm implemented in Python. This resulted in a real time PI control simulation which gave agreement with experiment. Problems observed in the data, for example the current drifting problem, were correctly reproduced by the simulation. Even a simulation conducted in free space based on analytical magnetic field calculations (not requiring OPERA) showed many of the same issues. The strong message for future work is to use this kind of simulation as a tool for testing the entire system before it is built.

3. Better understanding of matrix inversion, PI parameters, and tuning

The author of Ref. [69] proposed matrix inversion with Tikhonov regularization, which I followed initially. I realized later, however, that there was more to the story. I noticed there a relationship between the regularization parameter r and the PI parameters. I came to the conclusion that no amount of PI tuning could reduce the current drifting problem even though r was optimized according to Ref. [69]. However, I found that the current drifting problem could be reduced by treating r more-or-less as another free parameter at the cost of introducing high frequency noise. Moreover, I proposed a new method to find r based on the condition number of the matrix which I argue is more robust than the method of Ref. [69]. Eventually, I realized that regularized matrix inversion was nonoptimal. It can be avoided by carefully designing a well-conditioned system. This conclusion is consistent with Ref. [100].

References [71, 100], further proposed a new feedback algorithm. I showed that this was equivalent to a PI system restricted to one particular choice of tuning parameters. It is clearly better not to use a restricted set of tuning parameters.

4. Coil current modes based on coil configuration

Solving the current drifting problem was one breakthrough of this thesis. After many experimental tests, I found that the simulation in free space was very effective in improving the understanding of the problem. I discovered that the 6-coil feedback algorithm always had one mode which generated zero field no matter what the current. This resulted in one singular value that was always near zero. Tikhonov regularization tries to force this mode to be treated on an equal footing with the others. I found a superior solution which connects

two coils in series (a 5-coil feedback algorithm) thus preventing the undesirable mode from occurring. It was then I realized that I did not need to regularize the system if the system is well conditioned in the first place. In the end, I agreed with Ref. [71] that a low condition number (near unity) is a measure of good system design. As further coil design was beyond the scope of this thesis, it suggests future work studying coil design in the context of the condition number to study the ill-conditioning problem.

6.2 Recommendations on the Active Magnetic Compensation System Design Process for TUCAN

In this Section, I make a few general recommendations on how I would proceed if designing the ultimate active magnetic compensation system for the TUCAN nEDM experiment.

6.2.1 Test designs based on known perturbations

One of the key observations that suggested my system was finally working properly was that when the perturbation coil was turned on, the system would respond dominantly by turning on only the nearest coil that generates a field in the same axis as that coil (in the 5-coil system). In the 6-coil system, this was not the case. All 6 coils would eventually engage. Eventually I determined that this was simply an error induced by inappropriate constraints being placed on the system, which were covered up by the process of matrix regularization. What I wish I had done early would have

been to recognized that this is a sign of a failing treatment of the matrix. This would have helped me to focus in on the real problem and solve it faster.

Another recommendation related to this one is to carefully measure the perturbations expected, or to simulate the planned perturbations if driven by a perturbation coil. A plan to measure background field fluctuations at TRIUMF is ongoing at this time [55], and a perturbation coil for testing has already been built there [101, 102]. These should be used, in simulation, to test any planned multi-dimensional PI system. Based on the discussion above, if I had conducted such analysis in simulation first, I would have discovered the solution to the current drifting problem much earlier.

6.2.2 To regularize or not to regularize

My recommendation is to develop a system with sufficient degrees of freedom and with condition number as close to unity as possible.

In my case, the matrix regularization tended to stabilize the magnetic fields properly, but gave a very slow response in the currents. Eventually this was found to be due to a poorly constrained system with too many degrees of freedom. Tikhonov regularization made the system work, after a fashion, but could not solve the current-drifting problem. The reason is that Tikhonov regularization forced the “zero field” mode (singular value zero) to contain some current. There is no real purpose to have this mode exist at all.

My expectation is that this problem can be solved in an alternate way. In my case of a 6-coil system, it was easy. I simply reduced the number of degrees of freedom of the system without loss of generality, so that there were only five independent

currents (5-coil system). I expect this solution can be generalized to any arbitrary number of coils, and I suggest a few possible methods to do this in Section 6.2.4 below.

It is important to consider the condition number of the matrix when designing the coil system. If the condition number is reduced near unity, it could be a step in the right direction. It is also important to consider the right singular vectors (*i.e.* coil modes), which could reveal why a certain singular value is small.

6.2.3 Condition number is not everything

One clear way to reduce the condition number is to simply use Helmholtz coils for everything (three independent sets with three independent currents). In fact such a solution was pursued in the prototype system of Ref. [71] constructed at ETH Zürich. However, this is clearly a bad strategy because such a system will not have as many degrees of freedom as six independent coils. For example, it would never be able to compensate magnetic gradients. What is not trivial is why five independent coils is sufficient. But if thinking in terms of spherical harmonics applied to the magnetic scalar potential, and the kinds of fields that can be generated by Helmholtz coils, this becomes more obvious. This leads to my next recommendation.

6.2.4 What to do instead of regularizing

If I have to begin designing coils tomorrow, I would try the following two general strategies: (i) use orthogonal coils that generate spherical harmonics, and (ii) eliminate the possibility of generating a zero-field mode.

Coils that generate spherical harmonics

A decomposition of the magnetic field into a desired order of spherical harmonics can be conducted. The order could be constrained by the potential sources (discussed in Section 6.2.1) that are desired to be compensated. Decomposing the magnetic scalar potential in this way allows one to design coils, each of which generates a spherical harmonic. Alternately, patch coils could be used to generate each spherical harmonic. Both strategies were discussed in Refs. [71, 103]. Since this method will prevent the zero-field mode from occurring, this should result in a properly conditioned system. This can easily be tested in a coil simulation.

Eliminating the zero-field mode

Another alternate solution could be to wind patch coils on a convenient square frame and initially to allow all possible modes to be excited in the coil system. One of these modes will then correspond to the zero-field mode. Fortunately, this mode can easily be identified because it will have a singular value that is zero, or at least considerably smaller than the other modes. Once this mode has been identified, it can be removed from the singular matrix and the dimension of the matrix reduced by one. The remaining right singular vectors (coil modes) can then be used as the degrees of freedom of the system.

If any other modes should appear with singular values that are small, they too could be removed in a similar fashion until the condition number is small enough. This would prevent the need for matrix regularization, since it provides another method to limit the number of degrees of freedom.

Both methods could easily be implemented in a coil simulation. I would even recommend that the calculation be done in free space initially so that FEA need not be used. Then the system could be designed much more quickly and a reduced set of simulation be done in FEA once the appropriate number of degrees of freedom has been decided.

6.2.5 Develop a full FEA plus feedback system simulation

A key achievement of my thesis was the application of FEA results to the PI simulation. It was the simulation of the current-drifting problem in my 6-coil system that eventually convinced me that this must be a problem inherent to the multi-dimensional control system.

If either free-space and/or FEA calculations are available for both the perturbations and for the coil system, it is easy to implement these into a single time-dependent PI simulation. This kind of simulation generally reproduces all the experimental results as I have shown in my thesis. If I had done this simulation first, I might even have been able to discover the current-drifting problem in advance of every conducting the experiments.

6.3 Implementation in the TUCAN nEDM Experiment

In the previous section, I discussed a few specific ideas on how I would proceed to design an active compensation system. Most of these relate to the development of

simulation tools which can guide the design. Aside from this, there are a large number of other factors that must be considered when designing such a system for TUCAN. The first and foremost question is to be answered is whether the nEDM experiment needs an active compensation system or not.

Historically, such systems were not used in the Sussex-RAL-ILL nEDM experiments. The PSI group was the first to implement such an active compensation system in an nEDM experiment [56]. The system was developed mainly to improve experiment up-time. With the PSI experiment being located closer to facilities generating strong magnetic fields, the experiment would have to spend longer periods of time degaussing without an active compensation system.

Their upgraded experiment n2EDM will be located in the same area. One of the main improvements will be to use a magnetically shielded room (MSR). Even in this situation, it is unclear whether any active magnetic compensation system is necessary. In Ref. [71], drawings of a potential system were shown. In a recent conference proceeding [42], it was indicated an active compensation system was being developed as an additional shielding layer and that it “might be installed after initial characterization measurements.”

To decide on the active compensation strategy for the TUCAN nEDM experiment (Fig. 6.1), I recommend to consider the following factors:

- 1. Which fields the active compensation system should correct, and why**

The MSR is likely to be designed with shielding factor 10^5 on the basis that external 100 nT fluctuations be reduced to the pT level. At this level they are within the typical level of magnetic noise and drift arising from changes

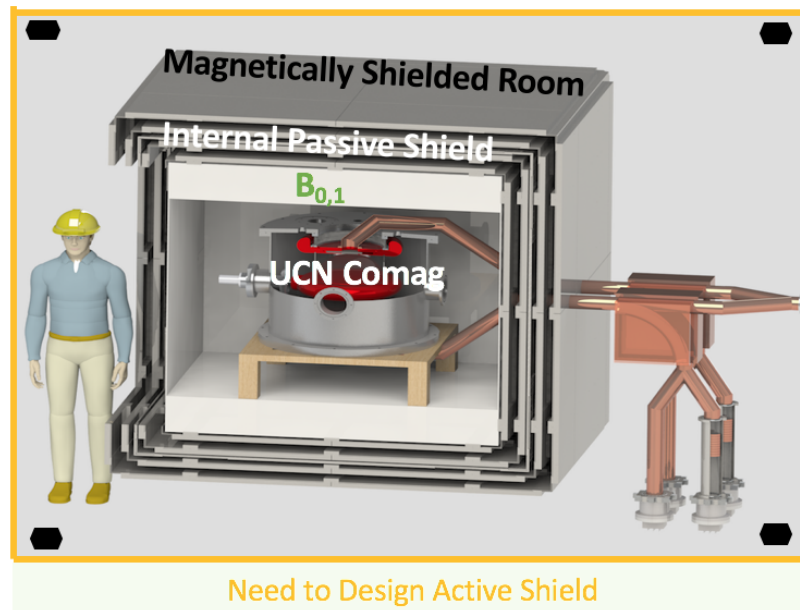


Figure 6.1: Schematic diagram of TUCAN nEDM magnetic field subsystems. From inside out: UCN and the comagnetometer, followed by the internal coil system (B_0 and B_1 coils), four layers of passive shielding comprising the magnetically shielded room (MSR), and the active compensation system which needs to be designed.

in the remnant magnetization of the innermost shield layer after degaussing (idealization).

The active compensation system might be able to correct 1000 nT fluctuations to the 100 nT level as an aggressive but potentially realistic goal. This might make it possible to run the system with worse exterior fluctuations. The question at this point is whether there are any such 1000 nT fluctuations present in Meson Hall, which is relatively unknown.

It is known that crane motion can amount to a 10000 nT or larger perturbation. It is unlikely a compensation system could be design that could compensate this

level of fluctuations. The best we could then hope for is that the system would be used more as its design goal at PSI, *i.e.* to reduce downtime by minimizing the amount of degaussing required after such an excursion.

2. Trade-offs of active vs. passive shielding and the decision on the dividing line between the two

The main question here might be about possible 1000 nT fluctuations in Meson Hall. If they are continuous and negate running the experiment, the budget, personnel, and schedule question would be whether it is superior to develop an active compensation system or to add one layer of passive magnetic shielding.

Clearly, the MSR is designed to handle 100 nT fluctuations, and crane motion is likely rare during nEDM running. So, the real question is if there are any unnaturally large fluctuations 1000 nT. There is presently insufficient information on magnetic fields in Meson Hall to say whether this is worthwhile to consider or not.

3. Saturation of the outermost layer of the MSR

At large DC fields such as the 400,000 nT scale experienced in Meson Hall, saturation of the passive magnetic shielding system comprising the MSR can be a concern, which would seriously impact its effectiveness. As long as the outermost magnetic shield layer does not saturate, and the exterior fluctuations to be compensated by the MSR are at the 100 nT scale, then this is no longer a concern, *i.e.* the MSR will certainly perform adequately without any active magnetic compensation system. The question becomes if it is worthwhile to con-

sider compensating for changes in the cyclotron field which drives the magnetic environment of the area, or if saturation has any realistic chance of occurring. The active compensation system could be used to counter such effects.

4. Magnetically shielded access to the MSR

When accessing the experiment, the door to the MSR must be opened. If presented with a large external field, the inner layers of the passive shielding system could themselves become magnetized, necessitating degaussing and additional experimental down-time. Furthermore, it is also useful to have an area just outside the door with a somewhat smaller magnetic field where components can be prepared for installation. An active compensation could provide such a region as a side goal.

5. Engineering, space, and access requirements

The compensation system would need to fit into the experimental area and not limit access to important parts of the experiment. The interfaces to other subsystems needs to be taken into account.

I expect that based on these factors, an active magnetic compensation system will eventually be implemented into the TUCAN nEDM experiment. My work serves as a useful study of a prototype system. Several new challenges were uncovered and solved along the way, which should help guide the design of the system at TRIUMF.

Appendix A

Analytic solutions to a spherical mu-metal shell in multi-pole field

The TUCAN nEDM experiment will be carried out inside the large magnetically shielded room that is roughly 3 m in diameter. The magnetic environment around the experiment will be challenging because of the closeness of the experiment to the TRIUMF cyclotron, which generates a background field of $\sim 350 - 400 \mu\text{T}$. As a result, it is important to gain an understanding of the magnitude and distribution of the field inside the bulk of a large mu-metal shield located in such an external field. For the purpose of studying this, we derive here analytic solutions of the magnetic field inside the bulk of a spherical mu-metal shield that serves as a model of our MSR in the TRIUMF cyclotron field. For simplicity, we assume a linear magnetic permeability for the shield.

A.1 General solution for an applied zonal field

The boundary conditions between two regions satisfying $\mathbf{B} = \mu\mathbf{H}$ with μ being magnetic permeability are

$$\left. \begin{aligned} B_2^\perp &= B_1^\perp \\ \text{or} \\ H_2^\perp &= \frac{\mu_1}{\mu_2} H_1^\perp \end{aligned} \right\} \quad (\text{A.1})$$

where, B_1^\perp and B_2^\perp are the normal components of magnetic flux density \mathbf{B} immediately inside region 1 and region 2 respectively and

$$\left. \begin{aligned} H_2^\parallel &= H_1^\parallel \\ \text{or} \\ \frac{1}{\mu_2} B_2^\parallel &= \frac{1}{\mu_1} B_1^\parallel \end{aligned} \right\} \quad (\text{A.2})$$

where, H_1^\parallel and H_2^\parallel are the tangential components of magnetic field \mathbf{H} immediately inside region 1 and region 2 respectively in absence of surface current.

In the limit $\mu_1/\mu_2 \rightarrow \infty$, the magnetic field will be vanished in the cavity of region 1 and such a reduction in field is known as magnetic shielding due to high permeable material. The MSR for TUCAN nEDM experiment will be built using this concept of magnetic shielding.

For a magnetic shielding system with n number of shielding layers, there are $2n$ number of distinct surface currents contributing to the net magnetic field in each regions as presented by Ref. [104] whereas the net magnetic field is determined by $4n$ simultaneous equations while using the magnetic scalar potential which is presented by Ref. [105].

In this section, we present those two different methods for solving the magnetic field inside the bulk of a spherical mu-metal shield in the presence of an applied zonal field.

A.1.1 Using Equivalent Bound Surface Currents

The spherical harmonics of order l and degree m can be used to represent any surface current bound to a sphere and the resulting field due to the surface current [104, 106]. The magnetic field calculation using zonal surface current due to presence of a spherical mu-metal shield in a multi-pole field has been discussed in Ref. [104]. We have shown the intermediate steps of the derivation to find out the magnetic field inside the bulk of a spherical mu-metal shield.

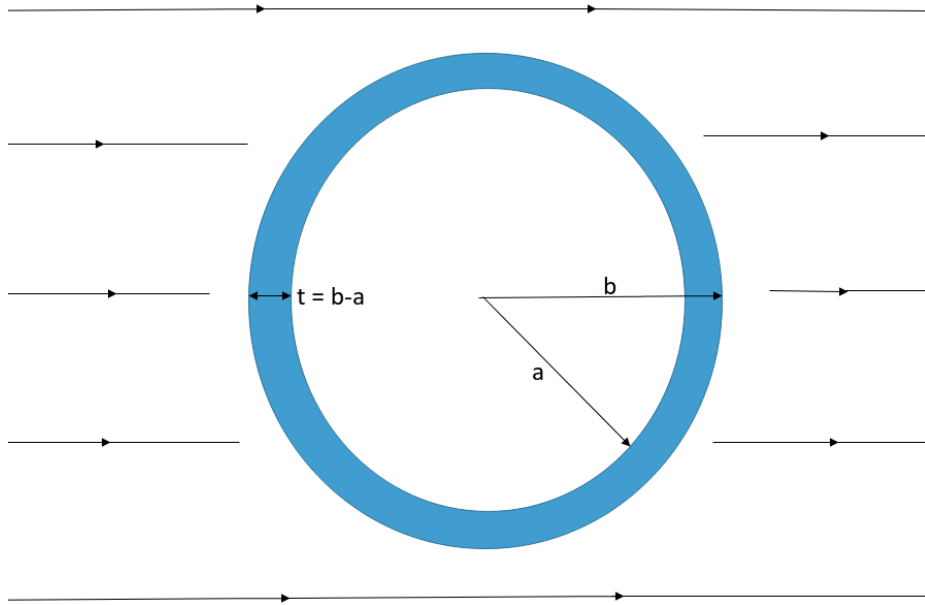


Figure A.1: Spherical shell of inner radius “a” and outer radius “b” with a thickness “t” in the presence of uniform magnetic field (i.e. $l = 1$).

We consider a spherical mu-metal shield of inner radius $r_1 = a$ and outer radius $r_2 = b$, and permeability μ centered on the origin and exposed to the general zonal field (*i.e.* $m = 0$) of order l as shown in Fig. A.1. The general external magnetic field can be written as [104]

$$\mathbf{B}_0 = G_l r^{l-1} (l+1) [l P_l(u) \hat{\mathbf{r}} - P_l^1(u) \hat{\boldsymbol{\theta}}], \quad (\text{A.3})$$

where the magnitude G_l is in units of T/m^{l-1} , $P_l^1(u)$ is the associated Legendre function of order 1 and degree l , and $u = \cos \theta$. The response of the permeable sphere results in bound surface currents \mathcal{K}_1 and \mathcal{K}_2 on radius a and b , respectively, that give rise to the following contributions to the net magnetic field:

$$\mathbf{B}_{\mathcal{K}_1} = \mathcal{K}_1 \begin{cases} r^{l-1} (l+1) [l P_l(u) \hat{\mathbf{r}} - P_l^1(u) \hat{\boldsymbol{\theta}}] & r < a \\ \frac{a^{2l+1}}{r^{l+2}} l [(l+1) P_l(u) \hat{\mathbf{r}} + P_l^1(u) \hat{\boldsymbol{\theta}}] & r > a \end{cases} \quad (\text{A.4})$$

$$\mathbf{B}_{\mathcal{K}_2} = \mathcal{K}_2 \begin{cases} r^{l-1} (l+1) [l P_l(u) \hat{\mathbf{r}} - P_l^1(u) \hat{\boldsymbol{\theta}}] & r < b \\ \frac{b^{2l+1}}{r^{l+2}} l [(l+1) P_l(u) \hat{\mathbf{r}} + P_l^1(u) \hat{\boldsymbol{\theta}}] & r > b \end{cases} \quad (\text{A.5})$$

where, $\mathcal{K}_1 = \mu_0 K_1 / (2l+1) a^{l-1}$, and $\mathcal{K}_2 = \mu_0 K_2 / (2l+1) b^{l-1}$ are the modified surface currents of K_1 and K_2 respectively.

The net field in different regions superposing bound surface currents and external fields are

$$\mathbf{B}_1 = (\mathcal{K}_1 + \mathcal{K}_2 + G_l) (l + 1) r^{l-1} [lP_l(u) \hat{\mathbf{r}} - P_l^1(u) \hat{\boldsymbol{\theta}}] \quad \text{for } r < a, \quad (\text{A.6})$$

$$\begin{aligned} \mathbf{B}_2 = & \mathcal{K}_1 l \frac{a^{2l+1}}{r^{l+2}} [(l + 1)P_l(u) \hat{\mathbf{r}} + P_l^1(u) \hat{\boldsymbol{\theta}}] \\ & + (\mathcal{K}_2 + G_l) (l + 1) r^{l-1} [lP_l(u) \hat{\mathbf{r}} - P_l^1(u) \hat{\boldsymbol{\theta}}] \quad \text{for } a < r < b, \text{ and} \end{aligned} \quad (\text{A.7})$$

$$\begin{aligned} \mathbf{B}_3 = & \frac{\mathcal{K}_1 a^{2l+1} + \mathcal{K}_2 b^{2l+1}}{r^{l+2}} n [(l + 1)P_l(u) \hat{\mathbf{r}} + P_l^1(u) \hat{\boldsymbol{\theta}}] \\ & + G_l (l + 1) r^{l-1} [nP_l(u) \hat{\mathbf{r}} - P_l^1(u) \hat{\boldsymbol{\theta}}] \quad \text{for } r > b. \end{aligned} \quad (\text{A.8})$$

The boundary condition of Eq. (A.2) has been applied to the tangential components B_θ of different regions to find \mathcal{K}_1 and \mathcal{K}_2 *i.e.* The boundary condition for $r = a$ with region 1 and region 2 is

$$\frac{1}{\mu_0} B_{1\theta} = \frac{1}{\mu} B_{2\theta}. \quad (\text{A.9})$$

Using Eqs. (A.6), and (A.7) in (A.9),

$$[\mu + \mu_0 \frac{l}{l+1}] \mathcal{K}_1 + (\mu - \mu_0) \mathcal{K}_2 = -(\mu - \mu_0) G_l \quad (\text{A.10})$$

$$\mathcal{K}_2 = -G_l - \frac{\mu(l+1) + \mu_0 l}{(\mu - \mu_0)(l+1)} \mathcal{K}_1 \quad (\text{A.11})$$

Similarly, the boundary condition for $r = b$ with region 2 and region 3 is

$$\frac{1}{\mu} B_{2\theta} = \frac{1}{\mu_0} B_{3\theta}. \quad (\text{A.12})$$

Using Eqs. (A.7), and (A.8) in Eq. (A.12),

$$(\mu - \mu_0) \frac{l}{l+1} \left(\frac{a}{b}\right)^{2l+1} \mathcal{K}_1 + [\mu \frac{l}{l+1} + \mu_0] \mathcal{K}_2 = (\mu - \mu_0) G_l \quad (\text{A.13})$$

Adding Eqs. (A.10), and (A.13) and using the value of \mathcal{K}_2 from Eq. (A.11),

$$\mathcal{K}_1 = -\frac{\mu(\mu - \mu_0)(l + 1)(2l + 1)G_l}{[\mu(l + 1) + \mu_0 l][\mu l + \mu_0(l + 1)] - (\mu - \mu_0)^2 l(l + 1) \left(\frac{a}{b}\right)^{2l+1}} \quad (\text{A.14})$$

For $\mu \gg \mu_0$, Eqs. (A.11), and (A.14) reduced to

$$\begin{aligned} \mathcal{K}_1 &\approx -\frac{\mu^2(l + 1)(2l + 1)G_l}{\mu^2 l(l + 1) - \mu^2 l(l + 1) \left(\frac{a}{b}\right)^{2l+1}} \\ &\approx -\frac{(2l + 1)G_l}{l - l \left(\frac{a}{b}\right)^{2l+1}}, \text{ and} \end{aligned} \quad (\text{A.15})$$

$$\begin{aligned} \mathcal{K}_2 &\approx -G_l - \frac{\mu(l + 1)}{\mu(n + 1)} \mathcal{K}_1 \\ &\approx -G_l - \mathcal{K}_1. \end{aligned} \quad (\text{A.16})$$

The net field within the bulk of the shield (*i.e.*, $a < r < b$) (see Eq. (A.7)) for $\mu \gg \mu_0$ is

$$\begin{aligned} \mathbf{B}_2 &= (l + 1)(2l + 1)r^{l-1}G_l \\ &\left[\left[\frac{1 - \left(\frac{a}{r}\right)^{2l+1}}{1 - \left(\frac{a}{b}\right)^{2l+1}} \right] P_l(u)\hat{\mathbf{r}} - \frac{1}{l} \left[\frac{1 + \frac{l}{l+1} \left(\frac{a}{r}\right)^{2l+1}}{1 - \left(\frac{a}{b}\right)^{2l+1}} \right] P_l^1(u)\hat{\boldsymbol{\theta}} \right]. \end{aligned} \quad (\text{A.17})$$

A.1.2 Using Scalar Potential

The magnetic field calculation using scalar potential due to presence of a spherical mu-metal shield in a uniform magnetic field has been discussed in Section 5.12 of Ref. [105]. We have extended the derivation of that Section to find out the magnetic field inside the bulk of a spherical mu-metal shield in a multi-pole field $\mathbf{B}_0 = \mu_0 \mathbf{H}_0$ of

order l and compared with the bound surface current method discussed in previous Section considering the same mu-metal as shown in Fig. A.1.

Ampere's law relates the magnetic field \mathbf{H} to the current density \mathbf{J} as $\nabla \times \mathbf{H} = \mathbf{J}$. As there is no free currents presents *i.e.* $\mathbf{J}_f = \mathbf{K}_f = 0$, so $\nabla \times \mathbf{H} = 0$ everywhere. It implies that there exists a magnetic scalar potential Φ that is continuous everywhere and the magnetic field \mathbf{H} is derivable as

$$\mathbf{H} = -\nabla\Phi. \quad (\text{A.18})$$

According to Maxwell's equation, the magnetic field \mathbf{B} has divergence equal to zero *i.e.* $\nabla \cdot \mathbf{B} = 0$. Since $\mathbf{B} = \mu\mathbf{H}$, magnetic field \mathbf{H} also has divergence equal to zero *i.e.*

$$\nabla \cdot \mathbf{H} = 0. \quad (\text{A.19})$$

Using Eq. (A.18) in Eq. (A.19),

$$\nabla \cdot \mathbf{H} = \nabla^2\Phi = 0. \quad (\text{A.20})$$

So, Φ satisfies the Laplace equation. In spherical co-ordinates (r, θ, ϕ) , it is

$$\nabla^2\Phi = \frac{1}{r^2} \left[\frac{\partial}{\partial r} \left(r^2 \frac{\partial\Phi}{\partial r} \right) \right] + \frac{1}{r^2 \sin\theta} \left[\frac{\partial}{\partial\theta} \left(\sin\theta \frac{\partial\Phi}{\partial\theta} \right) \right] + \frac{1}{r^2 \sin^2\theta} \frac{\partial^2\Phi}{\partial\phi^2}. \quad (\text{A.21})$$

The general solution is

$$\Phi(r, \theta, \phi) = \sum_{l=0}^{\infty} \sum_{m=-l}^l [A_{lm}r^l + B_{lm}r^{-(l+1)}] Y_{lm}(\theta, \phi). \quad (\text{A.22})$$

The problem has complete rotational symmetry about the z -axis *i.e.* azimuthal symmetry. So, the general solution Φ is independent of ϕ *i.e.* $m = 0$ is reduced to

$$\Phi(r, \theta) = \sum_{l=0}^{\infty} [A_l r^l + B_l r^{-(l+1)}] P_l(\cos\theta). \quad (\text{A.23})$$

The scalar potential at different regions are then

$$\Phi_1 = \delta r^l P_l(\cos \theta) \quad \text{for } r < a, \quad (\text{A.24})$$

$$\Phi_2 = \left(\beta r^l + \frac{\gamma}{r^{l+1}} \right) P_l(\cos \theta) \quad \text{for } a < r < b, \text{ and} \quad (\text{A.25})$$

$$\Phi_3 = -H_0 r^l P_l(\cos \theta) + \frac{\alpha}{r^{l+1}} P_l(\cos \theta) \quad \text{for } r > b. \quad (\text{A.26})$$

The co-coefficients δ , β , γ and α for different regions are determined by boundary conditions (Eqs. (A.1) and (A.2)) at $r = a$, and $r = b$.

Using Eq. (A.18) and the boundary condition from Eq. (A.1),

$$\frac{\partial \Phi_2}{\partial \theta} \Big|_{r=a} = \frac{\partial \Phi_1}{\partial \theta} \Big|_{r=a}.$$

Using the values from Eqs. (A.24), and (A.25),

$$\beta a^l + \frac{\gamma}{a^{l+1}} = \delta a^l. \quad (\text{A.27})$$

$$\frac{\partial \Phi_3}{\partial \theta} \Big|_{r=b} = \frac{\partial \Phi_2}{\partial \theta} \Big|_{r=b}.$$

Using the values from Eqs. (A.25), and (A.26),

$$-H_0 b^l + \frac{\alpha}{b^{l+1}} = \beta b^l + \frac{\gamma}{b^{l+1}}. \quad (\text{A.28})$$

Using Eq. (A.18) and the boundary condition from Eq. (A.2),

$$\mu \frac{\partial \Phi_2}{\partial r} \Big|_{r=a} = \mu_0 \frac{\partial \Phi_1}{\partial r} \Big|_{r=a}.$$

Using the values from Eqs. (A.24), and (A.25), and $\mu' = \mu/\mu_0$,

$$\delta l a^{l-1} = \mu' \left[\beta l a^{l-1} - \frac{(l+1)\gamma}{a^{l+2}} \right]. \quad (\text{A.29})$$

$$\mu_0 \frac{\partial \Phi_3}{\partial r} \Big|_{r=b} = \mu \frac{\partial \Phi_2}{\partial r} \Big|_{r=b}.$$

Using the values from Eqs. (A.25), and (A.26),

$$-H_0 b^{l-1} - \frac{(l+1)\alpha}{b^{l+2}} = \mu' \left[\beta l b^{l-1} - \frac{(l+1)\gamma}{b^{l+2}} \right]. \quad (\text{A.30})$$

Eqs. (A.27), (A.28), (A.29), and (A.30) can be reduced to

$$\alpha - b^{2l+1}\beta - \gamma = b^{2l+1}H_0, \quad (\text{A.31})$$

$$a^{2l+1}\beta + \gamma - a^{2l+1}\delta = 0, \quad (\text{A.32})$$

$$(l+1)\alpha + \mu' l b^{2l+1}\beta - \mu'(l+1)\gamma = -l b^{2l+1}H_0, \text{ and} \quad (\text{A.33})$$

$$\mu' l a^{2l+1}\beta - \mu'(l+1)\gamma - l a^{2l+1}\delta = 0. \quad (\text{A.34})$$

Subtracting Eq. (A.32) from Eq.(A.34)/l,

$$\gamma = \beta \left[\frac{a^{2l+1}(\mu' - 1)}{\left(\frac{l+1}{l}\right) \mu' + 1} \right]. \quad (\text{A.35})$$

Subtracting Eq. (A.31)*(l+1) from Eq. (A.33) and using the value of Eq.(A.35),

$$\beta = - \left[\frac{(2l+1) \left(\frac{l+1}{l}\right) \mu' + 1}{(\mu' l + l + 1) \left[\left(\frac{l+1}{l}\right) \mu' + 1\right] - (l+1) \left(\frac{a}{b}\right)^{2l+1} (\mu' - 1)^2} \right] H_0. \quad (\text{A.36})$$

Putting the value of Eq. (A.36) in Eq. (A.35),

$$\gamma = - \left[\frac{(2l+1) a^{2l+1} (\mu' - 1)}{(\mu' l + l + 1) \left[\left(\frac{l+1}{l}\right) \mu' + 1\right] - (l+1) \left(\frac{a}{b}\right)^{2l+1} (\mu' - 1)^2} \right] H_0. \quad (\text{A.37})$$

Putting the value of Eqs. (A.36), and (A.37) in Eq. (A.32),

$$\delta = - \left[\frac{\frac{(2l+1)^2}{l} \mu'}{(\mu' l + l + 1) \left[\left(\frac{l+1}{l} \right) \mu' + 1 \right] - (l+1) \left(\frac{a}{b} \right)^{2l+1} (\mu' - 1)^2} \right] H. \quad (\text{A.38})$$

For $\mu' \gg 1$, Eqs. (A.36), and (A.37) reduced to

$$\beta \approx - \left[\frac{2l+1}{\mu' l \left[1 - \left(\frac{a}{b} \right)^{2l+1} \right]} \right] H_0, \text{ and} \quad (\text{A.39})$$

$$\gamma \approx - \left[\frac{(2l+1) a^{2l+1}}{\mu' (l+1) \left(1 - \left(\frac{a}{b} \right)^{2l+1} \right)} \right] H_0. \quad (\text{A.40})$$

Using the values from Eqs. (A.39), and (A.40), and $u = \cos \theta$ in Eq. (A.25),

$$\Phi_2 = - \frac{(2l+1) B_0 r^l P_l(u)}{\mu l} \left[\frac{1 + \frac{l}{l+1} \left(\frac{a}{r} \right)^{2l+1}}{1 - \left(\frac{a}{b} \right)^{2l+1}} \right]. \quad (\text{A.41})$$

Using the value from Eq. (A.41),

$$\begin{aligned} H_r &= - \frac{\partial \Phi_2}{\partial r} \\ &= \frac{(2l+1)}{\mu} r^{l-1} B_0 P_l(u) \left[\frac{1 - \left(\frac{a}{r} \right)^{2l+1}}{1 - \left(\frac{a}{b} \right)^{2l+1}} \right] \text{ and} \end{aligned} \quad (\text{A.42})$$

$$B_r = (2l+1) r^{l-1} B_0 P_l(u) \left[\frac{1 - \left(\frac{a}{r} \right)^{2l+1}}{1 - \left(\frac{a}{b} \right)^{2l+1}} \right], \quad (\text{A.43})$$

$$\begin{aligned} H_\theta &= - \frac{1}{r} \frac{\partial \Phi_2}{\partial \theta} \\ &= - \frac{(2l+1)}{\mu l} B_0 r^{l-1} P_l^1(u) \left[\frac{1 + \frac{l}{l+1} \left(\frac{a}{r} \right)^{2l+1}}{1 - \left(\frac{a}{b} \right)^{2l+1}} \right] \text{ and} \end{aligned} \quad (\text{A.44})$$

$$B_\theta = - \frac{(2l+1)}{l} B_0 r^{l-1} P_l^1(u) \left[\frac{1 + \frac{l}{l+1} \left(\frac{a}{r} \right)^{2l+1}}{1 - \left(\frac{a}{b} \right)^{2l+1}} \right]. \quad (\text{A.45})$$

Finally, the magnetic field inside the bulk of a spherical mu-metal shield is

$$\begin{aligned} \mathbf{B}_2 &= (2l+1) r^{l-1} B_0 \\ &\left[\left[\frac{1 - \left(\frac{a}{r} \right)^{2l+1}}{1 - \left(\frac{a}{b} \right)^{2l+1}} \right] P_l(u) \hat{r} - \frac{1}{l} \left[\frac{1 + \frac{l}{l+1} \left(\frac{a}{r} \right)^{2l+1}}{1 - \left(\frac{a}{b} \right)^{2l+1}} \right] P_l^1(u) \hat{\theta} \right]. \end{aligned} \quad (\text{A.46})$$

A.1.3 Comparison of two methods

For comparing two methods discussed in previous Sections, the surface current flowing at the interface of two magnetic materials has to be taken into consideration. Under such consideration, the boundary condition will be

$$\mu_2 H_2^{\parallel} - \mu_1 H_1^{\parallel} = \mu_0 \mathbf{K}. \quad (\text{A.47})$$

Using Eq. (A.18) and the boundary condition from Eq. (A.47) at $r = a$,

$$\begin{aligned} -\mu \frac{1}{r} \frac{\partial \Phi_2}{\partial \theta} \Big|_{r=a} + \mu_0 \frac{1}{r} \frac{\partial \Phi_1}{\partial \theta} \Big|_{r=a} &= \mu_0 \mathbf{K}_1 \\ \frac{1}{r} \frac{\partial \Phi_1}{\partial \theta} \Big|_{r=a} - \mu' \frac{1}{r} \frac{\partial \Phi_2}{\partial \theta} \Big|_{r=a} &= \mathbf{K}_1 \end{aligned}$$

Using Eqs. (A.24), and (A.25),

$$\begin{aligned} \frac{1}{a} \left[\delta a^l - \mu' \left(\beta a^l + \frac{\gamma}{a^{l+1}} \right) \right] \frac{\partial}{\partial \theta} (P_l(\cos \theta)) &= \mathbf{K}_1 \\ \frac{1}{a} \left[\delta a^l - \mu' \left(\beta a^l + \frac{\gamma}{a^{l+1}} \right) \right] [-P_l^1(u)] &= K_1 P_l^1(u) \\ a K_1 = \mu' \left(\beta a^l + \frac{\gamma}{a^{l+1}} \right) - \delta a^l & \\ \frac{(2l+1)a^{l-1+1} \mathcal{K}_1}{\mu_0} = \mu' \left(\beta a^l + \frac{\gamma}{a^{l+1}} \right) - \delta a^l & \\ \frac{(2l+1)a^l \mathcal{K}_1}{\mu_0} = a^l \left[\mu' \left(\beta + \frac{\gamma}{a^{2l+1}} \right) - \delta \right] & \end{aligned}$$

Using the values from Eqs. (A.36), (A.37), and (A.38),

$$\mathcal{K}_1 = -\frac{\mu_0 H}{l} \left[\frac{(2l+1)(\mu' - 1)\mu'}{(\mu' l + l + 1) \left[\left(\frac{l+1}{l} \right) \mu' + 1 \right] - (l+1) \left(\frac{a}{b} \right)^{2l+1} (\mu' - 1)^2} \right]. \quad (\text{A.48})$$

Eq. (A.14) can be written as

$$\mathcal{K}_1 = -\frac{G_l(l+1)}{l} \left[\frac{(2l+1)(\mu' - 1)\mu'}{(\mu' l + l + 1) \left[\left(\frac{l+1}{l} \right) \mu' + 1 \right] - (l+1) \left(\frac{a}{b} \right)^{2l+1} (\mu' - 1)^2} \right]. \quad (\text{A.49})$$

Comparing Eqs. (A.48), and (A.49)

$$G_l(l+1) = \mu_0 H. \quad (\text{A.50})$$

So, if Eq. (A.50) is correct, then we are getting same result using scalar potential as we got from bound surface current method for \mathcal{K}_1 . Similar approach can be taken for \mathcal{K}_2 .

A.2 Magnetic field with uniform background (l=1)

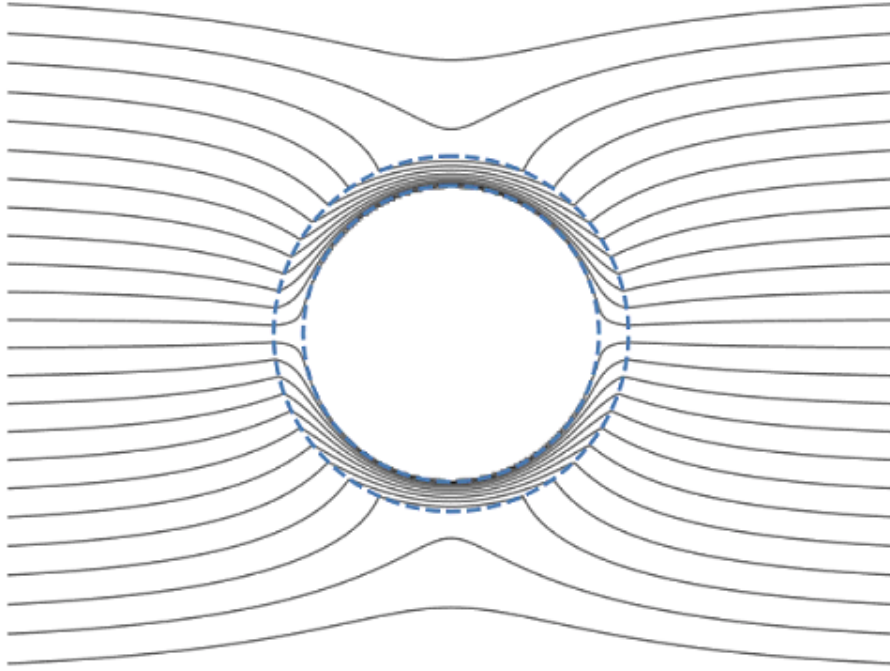


Figure A.2: Shielding effect of spherical shell in a uniform magnetic field.

In this Section, we will calculate the magnetic field inside the bulk of a spherical mu-metal shield in a uniform magnetic field (l=1). Figure A.2 shows the shielding effect of spherical shell in a uniform magnetic field (l=1).

For $\mu \gg \mu_0$ in Eq.(A.15),

$$\begin{aligned}\mathcal{K}_1 &\approx -\frac{\mu^2(l+1)(2l+1)G_l}{\mu^{2l}(l+1) - \mu^{2l}(l+1)\left(\frac{a}{b}\right)^{2l+1}} \\ &\approx -\frac{3G_1}{1 - \left(\frac{a}{b}\right)^3}.\end{aligned}\tag{A.51}$$

For $\mu \gg \mu_0$ in Eq.(A.16),

$$\mathcal{K}_2 \approx -G_1 - \mathcal{K}_1.\tag{A.52}$$

Using Eqs. (A.51), and (A.52) in Eq. (A.17), the magnetic field inside the bulk of a spherical mu-metal shield in a uniform magnetic field ($l=1$) is

$$\mathbf{B}_2 = 6G_1 \frac{1 - \left(\frac{a}{r}\right)^3}{1 - \left(\frac{a}{b}\right)^3} \cos\theta \hat{\mathbf{r}} - 3G_1 \frac{2 + \left(\frac{a}{r}\right)^3}{1 - \left(\frac{a}{b}\right)^3} \sin\theta \hat{\boldsymbol{\theta}}.\tag{A.53}$$

At poles and equator the field is

$$\mathbf{B}_2 \Big|_{\theta=0} = 3 B_0 \frac{1 - \left(\frac{a}{r}\right)^3}{1 - \left(\frac{a}{b}\right)^3} \hat{\mathbf{z}} \quad \text{at poles, and} \tag{A.54}$$

$$\mathbf{B}_2 \Big|_{\theta=\pi/2} = \frac{3}{2} B_0 \frac{2 + \left(\frac{a}{r}\right)^3}{1 - \left(\frac{a}{b}\right)^3} \hat{\mathbf{z}} \approx \frac{3}{2} B_0 \frac{a}{t} \hat{\mathbf{z}} \quad \text{at equator.} \tag{A.55}$$

A.2.1 Comparison with simulation

In this Section, the values obtained for uniform field in Section A.2 will be compared with simulated values. The simulation was performed in OPERA using the parameters of the mu-metal shield as shown in Table A.1 for a 400 μT applied field in y -direction.

Parameters	Sphere
Inner Radius, a (m)	1.296
Outer Radius, b (m)	1.3
Thickness, t (mm)	4
μ	20,000

Table A.1: Properties of the spherical mu-metal shield in OPERA.

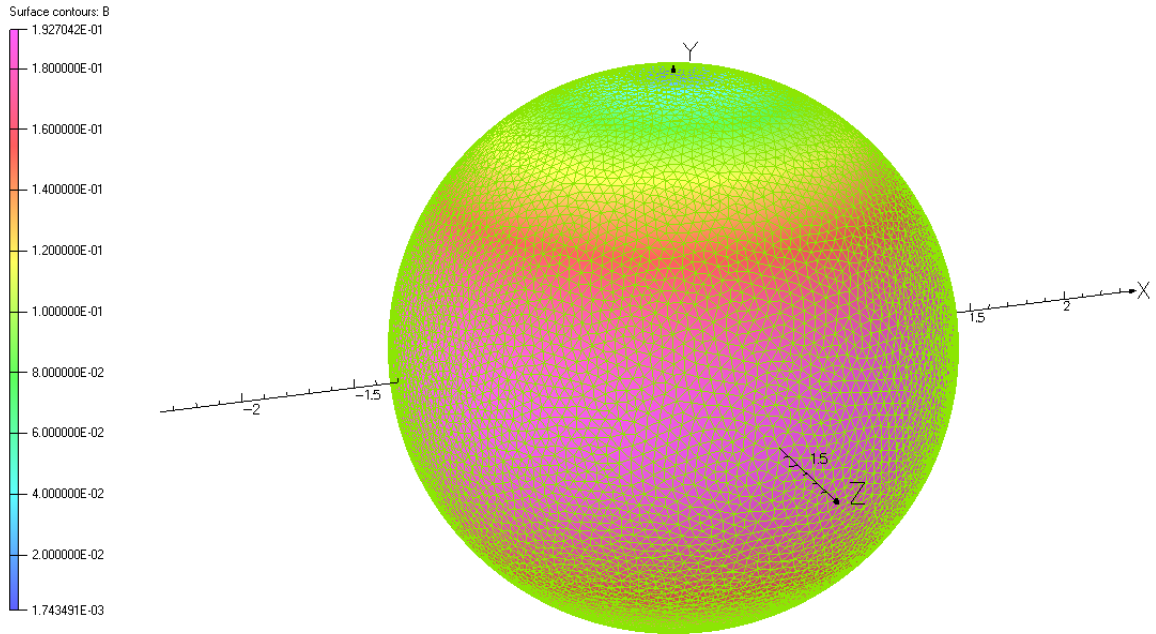


Figure A.3: Color map of the spherical mu-metal shield in OPERA.

Figure A.3 shows the color map of the spherical mu-metal shield in OPERA for the parameters in Table A.1 for the uniform applied field.

Positions (m)	Simulated \mathbf{B} (μT)	Analytical \mathbf{B} (μT)
$x = 1.298, y = 0.0, \text{ and } z = 0.0$	192,000	195,000
$x = 0.0, y = 1.298, \text{ and } z = 0.0$	537	602
$x = 0.0, y = 0.0, \text{ and } z = 1.298$	192,000	195,000
$x = 0.0, y = 1.3, \text{ and } z = 0.0$	1,120	1,200

Table A.2: Comparison of simulated \mathbf{B} field with analytical one for a 400 μT applied field in y -direction.

Table A.2 shows the comparison of simulated \mathbf{B} field with analytical one for a 400 μT applied field in y -direction. It is seen that the analytical values are in agreement with the simulated values.

Bibliography

- [1] T. E. Chupp, P. Fierlinger, M. J. Ramsey-Musolf, and J. T. Singh. [Electric dipole moments of atoms, molecules, nuclei, and particles](#). *Rev. Mod. Phys.*, 91(1):015001, 2019.
- [2] Wikimedia Commons. [Standard model of elementary particles](#), 2006.
- [3] V. Barger *et al.* [Effective number of neutrinos and baryon asymmetry from BBN and WMAP](#). *Physics Letters B*, 566(1):8–18, 2003.
- [4] A. D. Sakharov. [Violation of \$CP\$ Invariance, \$C\$ asymmetry, and baryon asymmetry of the universe](#). *JETP Lett.*, 5:24–27, 1967.
- [5] A. G. Cohen, D. B. Kaplan, and A. E. Nelson. [Progress in Electroweak Baryogenesis](#). *Annual Review of Nuclear and Particle Science*, 43(1):27–70, 1993.
- [6] N. F. Ramsey. [Electric-dipole moments of elementary particles](#). *Reports on Progress in Physics*, 45(1):95, 1982.
- [7] C.A. Baker *et al.* [Apparatus for measurement of the electric dipole moment of the neutron using a cohabiting atomic-mercury magnetometer](#). *Nuclear Instru-*

- ments and Methods in Physics Research Section A: Accelerators, Spectrometers, Detectors and Associated Equipment*, 736:184–203, 2014.
- [8] Ya. B. Zel'dovich. Storage of Cold Neutrons. *Sov. Phys. JETP*, 9:1389, 1959.
- [9] M. Lang. [Development of Active Magnetic Shielding for the Neutron Electric Dipole Moment Experiment at TRIUMF](#). Master's thesis, The University of Manitoba, 2013.
- [10] S. Ahmed *et al.* [First ultracold neutrons produced at TRIUMF](#). *Phys. Rev. C*, 99:025503, 2019.
- [11] T. Andalib. [Magnetic Fields and Ultracold Neutron Production: Studies Towards the Neutron Electric Dipole Moment Experiment at TRIUMF](#). PhD thesis, The University of Manitoba, 2019.
- [12] S. Ahmed *et al.* [A beamline for fundamental neutron physics at TRIUMF](#). *Nuclear Instruments and Methods in Physics Research Section A: Accelerators, Spectrometers, Detectors and Associated Equipment*, 927:101–108, 2019.
- [13] N. F. Ramsey. [A Molecular Beam Resonance Method with Separated Oscillating Fields](#). *Phys. Rev.*, 78:695–699, 1950.
- [14] J. Ellis. [Theory of the neutron electric dipole moment](#). *Nuclear Instruments and Methods in Physics Research Section A: Accelerators, Spectrometers, Detectors and Associated Equipment*, 284(1):33–39, 1989.
- [15] X.-G. He, B. H. J. Mckellar, and S. Pakvasa. [The Neutron Electric Dipole Moment](#). *International Journal of Modern Physics A*, 04(19):5011–5046, 1989.

- [16] S. A. R. Ellis and G. L. Kane. [Theoretical prediction and impact of fundamental electric dipole moments](#). *Journal of High Energy Physics*, 2016(1):77, 2016.
- [17] J. H. Smith, E. M. Purcell, and N. F. Ramsey. [Experimental Limit to the Electric Dipole Moment of the Neutron](#). *Phys. Rev.*, 108:120–122, 1957.
- [18] P. D. Miller, W. B. Dress, J. K. Baird, and N. F. Ramsey. [Limit to the Electric Dipole Moment of the Neutron](#). *Phys. Rev. Lett.*, 19:381–384, 1967.
- [19] C. G. Shull and R. Nathans. [Search for a Neutron Electric Dipole Moment by a Scattering Experiment](#). *Phys. Rev. Lett.*, 19:384–386, 1967.
- [20] W. B. Dress, J. K. Baird, P. D. Miller, and N. F. Ramsey. [Upper Limit for the Electric Dipole Moment of the Neutron](#). *Phys. Rev.*, 170:1200–1206, 1968.
- [21] V. W. Cohen, R. Nathans, H. B. Silsbee, E. Lipworth, and N. F. Ramsey. [Electric Dipole Moment of the Neutron](#). *Phys. Rev.*, 177:1942–1945, 1969.
- [22] J. K. Baird, P. D. Miller, W. B. Dress, and N. F. Ramsey. [Improved Upper Limit to the Electric Dipole Moment of the Neutron](#). *Phys. Rev.*, 179:1285–1291, 1969.
- [23] W. B. Dress, P. D. Miller, and N. F. Ramsey. [Improved Upper Limit for the Electric Dipole Moment of the Neutron](#). *Phys. Rev. D*, 7:3147–3149, 1973.
- [24] W. B. Dress, P. D. Miller, J. M. Pendlebury, P. Perrin, and N. F. Ramsey. [Search for an electric dipole moment of the neutron](#). *Phys. Rev. D*, 15:9–21, 1977.

- [25] I. S. Altarev *et al.* [A search for the electric dipole moment of the neutron using ultracold neutrons.](#) *Nuclear Physics A*, 341(2):269–283, 1980.
- [26] I. S. Altarev *et al.* [A new upper limit on the electric dipole moment of the neutron.](#) *Physics Letters B*, 102(1):13–16, 1981.
- [27] J. M. Pendlebury *et al.* [Search for a neutron electric dipole moment.](#) *Physics Letters B*, 136(5):327–330, 1984.
- [28] I. S. Altarev *et al.* [Search for an electric dipole moment of the neutron.](#) *JETP Letters*, 44(8):460–464, 1986.
- [29] K. F. Smith *et al.* [A search for the electric dipole moment of the neutron.](#) *Physics Letters B*, 234(1):191–196, 1990.
- [30] I. S. Altarev *et al.* [New measurement of the electric dipole moment of the neutron.](#) *Physics Letters B*, 276(1):242–246, 1992.
- [31] I. S. Altarev *et al.* [Search for the neutron electric dipole moment.](#) *Physics of Atomic Nuclei*, 59(7):1152–1170, 1996.
- [32] P.G. Harris *et al.* [New Experimental Limit on the Electric Dipole Moment of the Neutron.](#) 82:904–907, 1999.
- [33] C.A. Baker *et al.* [Improved Experimental Limit on the Electric Dipole Moment of the Neutron.](#) *Phys. Rev. Lett.*, 97:131801, 2006.
- [34] C. A. Baker *et al.* [Improved Experimental Limit on the Electric Dipole Moment of the Neutron.](#) *Phys. Rev. Lett.*, 97:131801, 2006.

- [35] J. M. Pendlebury *et al.* [Revised experimental upper limit on the electric dipole moment of the neutron.](#) *Phys. Rev. D*, 92:092003, 2015.
- [36] B. Yoon, T. Bhattacharya, and R. Gupta. [Neutron Electric Dipole Moment on the Lattice.](#) *EPJ Web Conf.*, 175:01014, 2018.
- [37] P. Schmidt-Wellenburg. [The quest for an electric dipole moment of the neutron.](#) *AIP Conf. Proc.*, 1753:060002, 2016.
- [38] S. Afach *et al.* [Measurement of a false electric dipole moment signal from \$^{199}\text{Hg}\$ atoms exposed to an inhomogeneous magnetic field.](#) *The European Physical Journal D*, 69(10):225, 2015.
- [39] S. Afach *et al.* [Observation of Gravitationally Induced Vertical Striation of Polarized Ultracold Neutrons by Spin-Echo Spectroscopy.](#) *Phys. Rev. Lett.*, 115:162502, 2015.
- [40] H.-C. Koch *et al.* [Design and performance of an absolute \$^3\text{He}/\text{Cs}\$ magnetometer.](#) *The European Physical Journal D*, 69(8):202, 2015.
- [41] B. Lauss. [Status of the apparatus for the next phase of the neutron EDM search at PSI n2EDM.](#) In *Neutron Electric Dipole Moment (nEDM2017) Workshop*, Harrison Hot Springs, BC, Canada, 2017.
- [42] C. Abel *et al.* [The n2EDM experiment at the Paul Scherrer Institute.](#) In *International Workshop on Particle Physics at Neutron Sources 2018 (PPNS 2018)*, Grenoble, France, 2018.

- [43] B. Filippone. [The SNS nEDM experiment](#). In *Neutron Electric Dipole Moment (nEDM2017) Workshop*, Harrison Hot Springs, BC, Canada, 2017.
- [44] J.-C. Peng. [Neutron Electric Dipole Moment Experiments](#). *Modern Physics Letters A*, 23(17n20):1397–1408, 2008.
- [45] S. K. Lamoreaux and R. Golub. [Detailed discussion of a linear electric field frequency shift induced in confined gases by a magnetic field gradient: Implications for neutron electric-dipole-moment experiments](#). *Phys. Rev. A*, 71:032104, 2005.
- [46] S. Clayton. [New effort to develop a new nEDM experiment at LANL](#). In *Neutron Electric Dipole Moment (nEDM2017) Workshop*, Harrison Hot Springs, BC, Canada, 2017.
- [47] R. Pattie. [Commissioning of the ultracold neutron source at Los Alamos Neutron Science Center](#). In *Neutron Electric Dipole Moment (nEDM2017) Workshop*, Harrison Hot Springs, BC, Canada, 2017.
- [48] T. M. Ito *et al.* [Performance of the upgraded ultracold neutron source at Los Alamos National Laboratory and its implication for a possible neutron electric dipole moment experiment](#). *Phys. Rev. C*, 97:012501, 2018.
- [49] A. P. Serebrov and P. Geltenbort. [nEDM research led by PNPI](#). In *Neutron Electric Dipole Moment (nEDM2017) Workshop*, Harrison Hot Springs, BC, Canada, 2017.
- [50] S. Degenkolb. [SuperSUN and PanEDM: a new superthermal UCN source for](#)

- a new nEDM measurement. In *Neutron Electric Dipole Moment (nEDM2017) Workshop*, Harrison Hot Springs, BC, Canada, 2017.
- [51] I. Altarev *et al.* [A magnetically shielded room with ultra low residual field and gradient](#). *Review of Scientific Instruments*, 85(7):075106, 2014.
- [52] I. Altarev *et al.* [A large-scale magnetic shield with 106 damping at millihertz frequencies](#). *Journal of Applied Physics*, 117(18):183903, 2015.
- [53] I. Altarev *et al.* [Minimizing magnetic fields for precision experiments](#). *J. Appl. Phys.*, 117:233903, 2015.
- [54] P. M. Sarte. [Magnetic Field Characterisation of the Meson Hall at TRIUMF for UCN-nEDM Experiment](#), 2013.
- [55] B. Franke. Private communication, Feb. 2019.
- [56] S. Afach *et al.* [Dynamic stabilization of the magnetic field surrounding the neutron electric dipole moment spectrometer at the Paul Scherrer Institute](#). *Journal of Applied Physics*, 116(8):084510, 2014.
- [57] C.A. Baker *et al.* [The search for the neutron electric dipole moment at the Paul Scherrer Institute](#). *Physics Procedia*, 17:159–167, 2011.
- [58] A. P. Serebrov *et al.* [New measurements of the neutron electric dipole moment](#). *JETP Letters*, 99(1):4–8, 2014.
- [59] I. Altarev *et al.* [A next generation measurement of the electric dipole moment of the neutron at the FRM II](#). *Nuovo Cim.*, C035N04:122–127, 2012.

- [60] K. Kirch. [EDM searches](#). *AIP Conference Proceedings*, 1560(1):90–94, 2013.
- [61] J. M. Pendlebury *et al.* [Geometric-phase-induced false electric dipole moment signals for particles in traps](#). *Phys. Rev. A*, 70:032102, 2004.
- [62] G. Pignol and S. Rocca. [Electric-dipole-moment searches: Reexamination of frequency shifts for particles in traps](#). *Phys. Rev. A*, 85:042105, 2012.
- [63] V. Kelha, J. Pukki, R. Peltonen, A. Penttinen, R. Ilmoniemi, and J. Heino. [Design, construction, and performance of a large-volume magnetic shield](#). *IEEE Transactions on Magnetics*, 18(1):260–270, 1982.
- [64] H. J. M. ter Brake, H. J. Wieringa, and H. Rogalla. [Improvement of the performance of a mu -metal magnetically shielded room by means of active compensation \(biomagnetic applications\)](#). *Measurement Science and Technology*, 2(7):596–601, 1991.
- [65] J. Bork, H.-D. Hahlbohm, R. Klein, and A. Schnabel. [The 8-layered magnetically shielded room of the PTB: Design and construction](#). In *Biomag 2000*, Helsinki University of Technology, Espoo, Finland, 2000.
- [66] D. Spemann, T. Reinert, J. Vogt, J. Wassermann, and T. Butz. [Active compensation of stray magnetic fields at LIPSION](#). *Nuclear Instruments and Methods in Physics Research Section B: Beam Interactions with Materials and Atoms*, 210:79–84, 2003.
- [67] T. Bryś *et al.* [Magnetic field stabilization for magnetically shielded volumes by external field coils](#). *Nuclear Instruments and Methods in Physics Research*

- Section A: Accelerators, Spectrometers, Detectors and Associated Equipment*, 554(1):527–539, 2005.
- [68] K. Kobayashi, A. Kon, M. Yoshizawa, and Y. Uchikawa. [Active Magnetic Shielding Using Symmetric Magnetic Field Sensor Method](#). *IEEE Transactions on Magnetics*, 48(11):4554–4557, 2012.
- [69] B. Franke. *Investigations of the internal and external magnetic fields of the neutron electric dipole moment experiment at the Paul Scherrer Institute*. PhD thesis, ETH Zürich, 2013.
- [70] T. Lins. *High Precision Physics in Low Magnetic Fields*. PhD thesis, Technische Universität München, München, 2016.
- [71] M. Rawlik. *Active Magnetic Shielding and Axion-Dark-Matter Search*. PhD thesis, ETH Zürich, 2018.
- [72] L. McLeod. [Active Shielding Prototype for the nEDM Measurement](#). In *TUCAN Collaboration Meeting, TRIUMF*, TRIUMF, BC, Canada, 2015.
- [73] LabJack Corporation. [A-3-1 Noise and Resolution \[T-Series Datasheet\]](#). Lakewood, CO, USA.
- [74] R. Mammei. [Passive Magnetic Shield](#). In *TUCAN Collaboration Meeting*, Japan, 2013.
- [75] Amuneal Manufacturing Corp. [Magnetic Shielding Materials](#). Philadelphia, PA, USA.

- [76] J. W. Martin, R. Mammei, W. Klassen, C. Cerasani, T. Andalib, C. P. Bidinosti, M. Lang, and D. Ostapchuk. [Large Magnetic Shielding Factor Measured by Nonlinear Magneto-optical Rotation](#). *Nucl. Instrum. Meth.*, A778:61–66, 2015.
- [77] P. Ripka. [Review of fluxgate sensors](#). *Sensors and Actuators A: Physical*, 33(3):129–141, 1992.
- [78] B. B. Narod. [The origin of noise and magnetic hysteresis in crystalline permalloy ring-core fluxgate sensors](#). *Geoscientific Instrumentation, Methods and Data Systems*, 3(2):201–210, 2014.
- [79] Bartington Instruments Ltd. [Three-Axis Fluxgate Magnetometers](#). Witney, OX, England.
- [80] Wolfram Research, Inc. [Mathematica, Version 11.3](#). Champaign, IL, 2018.
- [81] G. Heinzel, A. Rüdiger, and R. Schilling. [Spectrum and spectral density estimation by the Discrete Fourier transform \(DFT\), including a comprehensive list of window functions and some new at-top windows](#), 2002.
- [82] Analog Devices, Inc. [Analog Filter Wizard](#).
- [83] Space Weather Canada. [Magnetic Plotting Service](#).
- [84] J. C. A. Barata and M. S. Hussein. [The Moore–Penrose Pseudoinverse: A Tutorial Review of the Theory](#). *Brazilian Journal of Physics*, 42(1):146–165, 2012.
- [85] P. Hansen, J. Nagy, and D. O’Leary. [Deblurring Images](#). Society for Industrial and Applied Mathematics, 2006. See Chapters §1, §5, and §6.

- [86] V. Klema and A. Laub. [The singular value decomposition: Its computation and some applications.](#) *IEEE Transactions on Automatic Control*, 25(2):164–176, 1980.
- [87] S. Park and D. P. O’Leary. [Portfolio Selection Using Tikhonov Filtering to Estimate the Covariance Matrix.](#) *SIAM Journal on Financial Mathematics*, 1:932–961, 2010.
- [88] A. N. Tikhonov, A. V. Goncharsky, V. V. Stepanov, and A. G. Yagola. [Numerical Methods for the Solution of Ill-Posed Problems.](#) Mathematics and Its Applications. Springer Netherlands, 2013.
- [89] G. Golub and W. Kahan. [Calculating the Singular Values and Pseudo-Inverse of a Matrix.](#) *Journal of the Society for Industrial and Applied Mathematics Series B Numerical Analysis*, 2(2):205–224, 1965.
- [90] F. Nie, H. Huang, X. Cai, and C. Ding. [Efficient and Robust Feature Selection via Joint \$l_{2,1}\$ -Norms Minimization.](#) In J. D. Lafferty, C. K. I. Williams, J. Shawe-Taylor, R. S. Zemel, and A. Culotta, editors, *Advances in Neural Information Processing Systems 23*, pages 1813–1821. Curran Associates, Inc., 2010.
- [91] V. Braverman, S. R. Chestnut, R. Krauthgamer, Yi Li, D. P. Woodruff, and L. F. Yang. [Matrix Norms in Data Streams: Faster, Multi-Pass and Row-Order.](#) *arXiv e-prints*, 2016.

- [92] J. A. Shaw. *The PID Control Algorithm, Process Control Solutions*. New York, 2nd edition, 2003.
- [93] J. G. Ziegler and N. B. Nichols. Optimum Settings for Automatic Controllers. *Transactions of ASME*, 64:759–768, 1942.
- [94] B. R. Copeland. *The Design of PID Controllers using Ziegler Nichols Tuning*, 2008.
- [95] D. W. Allan. Statistics of atomic frequency standards. *Proceedings of the IEEE*, 54(2):221–230, 1966.
- [96] W. J. Riley. *Handbook of Frequency Stability Analysis*. U.S. Department of Commerce, NIST Special Publication 1065, 2008.
- [97] T. Andalib and J.W. Martin. *Allan Deviation: Definitions and Theoretical Forms*, 2016.
- [98] COBHAM. *OPERA Simulation Software*.
- [99] M. Rawlik. *External magnetic fields - mapping, monitoring and shielding*. In *Neutron Electric Dipole Moment (nEDM2017) Workshop*, Harrison Hot Springs, BC, Canada, 2017.
- [100] M. Rawlik. Private communication, Oct. 2017.
- [101] J. Smith. *Work Term Report*, 2017.
- [102] E. Cudmore. *Disturbance Coil Redesign and Characterization*, 2018.

- [103] M. Rawlik, C. Crawford, A Eggenberger, K. Kirch, J. Krempel, F. M. Piegsa, and G. Quéméner. [A simple method of coil design](#). *American Journal of Physics*, 86(8):602–608, 2018.
- [104] C. P. Bidinosti and J. W. Martin. [Passive magnetic shielding in static gradient fields](#). *AIP Advances*, 4(4):047135, 2014.
- [105] J. D. Jackson. *Classical Electrodynamics*. John Wiley & Sons Inc., New York, 3rd edition, 1999. See §5.12.
- [106] W.R. Smythe. *Static and Dynamic Electricity*. McGraw-Hill, New York, 2nd edition, 1950. See §5.23, §7.12, §7.14 and §7.17.